# UC San Diego
## UC San Diego Electronic Theses and Dissertations

**Title**
Advanced MEMS-Based Scalable Minimally-Invasive 1024 Channel Microneedle and Subdural Brain and Spinal Cord Implants

**Permalink**
https://escholarship.org/uc/item/06g7d01g

**Author**
Lee, Sang Heon

**Publication Date**
2020

Peer reviewed|Thesis/dissertation

UNIVERSITY OF CALIFORNIA SAN DIEGO

Advanced MEMS-Based Scalable Minimally-Invasive 1024 Channel Microneedle and Subdural

Brain and Spinal Cord Implants

A dissertation submitted in partial satisfaction of

the requirements for the degree Doctor of Philosophy

in

Electrical Engineering (Nanoscale Devices and Systems)

by

Sang Heon Lee

Committee in charge:

       Professor Shadi A. Dayeh, Chair
       Professor Gert Cauwenberghs
       Professor Anna Devor
       Professor Tse Nga Ng
       Professor Piya Pal

2021

The Dissertation of Sang Heon Lee is approved, and it is acceptable in quality and form for

publication on microfilm and electronically:

_____

_____

_____

_____

_____

Chair

University of California San Diego

2021

iii

# DEDICATION

To my beloved parents, little brother, and my wife.

<h1 style="text-align:center">TABLE OF CONTENTS</h1>

# LIST OF FIGURES

ix

# LIST OF TABLES

# ACKNOWLEDGEMENTS

The journey to earning this Ph.D. degree was probably the longest and the most challenging chapter in my life thus far, in which I not only learned to become a better researcher, but also to become a better, wiser, and mature person. There have been countless challenges in this pilgrimage for learning which I will never forget the delight of achievement when finally overcoming those hurdles. Here, this unforgettable chapter of my life concludes today which would not have been possible without all the support from those around me.

I would like to express my most sincere gratitude to my advisor, Professor Shadi A. Dayeh, for his wholehearted support during my Ph.D. study. He was always patient and ready to give the best advice when I needed the most. With his inspiration and guidance, I was able to step up and grow to become more independent in my research.

Also, I cannot forget all the help and support I received from the past and current IEBL group members: Yun Goo Ro, Keundong Lee, Hongseok Oh, Youngbin Tchoe, Farid Azzazy. Atsunori Tanaka, Renjie Chen, Namseok Park, Mehran Ganji, Ahmed Taha El-Thakeb, Ren Liu, Woojin Choi, Jihwan Lee, Lorraine Hossain, Siarhei Vishniakou, Supanee Sukrittanon, Andrew Bourhis, Ritwik Vatsyayan, Joonseop Sim, Nasim Vahidi, Samantha Russman, Po Chun Chen, Keisuke Matsushita, and Tianhai Wu.

The input from my collaborators was also immense. Professor Anna Devor and Professor Martin Thunemann, now at Boston University, were the key personnel in nailing my SiMNA technology, both in experiments and in strengthening the quality of data analysis. I cannot thank more to Dr. Joel Martin, Dr. Daniel Cleary, and Dr. Karen Tonsfeldt for their contributions in solidifying our *in vivo* platforms, and Professor Massoud Khraiche at American University of Beirut, for always supporting with positive insights and feedback of my research. Also, I would

like to express my deepest appreciation to Professor Sydney Cash's team at Massachusetts General Hospital, neurosurgery teams at Oregon Health & Science University and UC San Diego, Dr. Bang's team at Sanford Burnham Prebys, and Professor Kelly Frazer's group for the constructive collaboration over the years.

I also greatly benefited from the invaluable technical support from the staff members of Nano3 cleanroom at Calit2, UC San Diego (Dr. Bernd Fruhberger, Larry Grissom, Dr. Xuekun Lu, Patrick Driscoll, Hal Romans, Sean Parks, and Ahdam Ali), staff members of Center for Integrated Nanotechonologies at Sandia National Laboratories, and staff members of CNSE cleanroom at UC Riverside.

Last but not least, I cannot express more gratitude to my family. With the endless support from my father, Jae Yul Lee, my mother, Jin Young Yoon, and little brother, Hyun Woo Lee, all back in South Korea, and my beloved wife, Haerin Kim, I was able to survive through the toughest times during my Ph.D. study. My confidence and motivation to move forward roots from their love and encouragements.

Chapter 1, in full, is currently being prepared for submission for publication of the material. S. H. Lee, M. Thunemann, F. Azzazy, D. R. Cleary, K. Tonsfeldt, K. Lee, H. Oh, Y. Tchoe, A. Devor, S. A. Dayeh. The dissertation author is the primary investigator and author of this paper.

Chapter 2, in full, is currently being prepared for submission for publication of the material. S. H. Lee, J. R. Martin, D. R. Cleary, K. Tonsfeldt, J. Ciacci, S. A. Dayeh. The dissertation author is the primary investigator and author of this paper.

# VITA

2014        Bachelor of Science, Materials Science and Engineering (Electronic Materials)

            University of Illinois at Urbana-Champaign

2014-2020   Graduate Research Assistant, University of California San Diego

2017        Master of Science, Electrical Engineering (Nanoscale Devices and Systems)

            University of California San Diego

2021        Doctor of Philosophy, Electrical Engineering (Nanoscale Devices and Systems)

            University of California San Diego

# PUBLICATIONS

1. **S. H. Lee**, M. Thunemann, F. Azzazy, D. R. Cleary, K. Tonsfeldt, K. Lee, H. Oh, Y. Tchoe, A. Devor, S. A. Dayeh, "Scalable Thousand Channel Penetrating Microneedle Arrays on Flex for Multimodal and Large Area Coverage Brain-Machine Interfaces", in preparation.

2. **S.H. Lee**, J. R. Martin, D. R. Cleary, J. Ciacci, S. A. Dayeh, "Thresholds of Initiation and Tissue Damage for Dorsal/Ventral Spinal Cord Stimulation for Rodent Hindlimb Motion", in preparation.

3. A. C. Paulk, J. C. Yang, D. R. Cleary, D. J. Soper, M. Halgren, A. R. O'Donnell, **S. H. Lee**, M. Ganji, Y. G. Ro, H. Oh, L. Hossain, J. Lee, Y. Tchoe, N. Rogers, K. Kiliç, S. B. Ryu, S. W. Lee, J. Hermiz, V. Gilja, I. Ulbert, D. Fabó, O. Devinsky, J. R. Madsen, D. L. Schomer, E. N. Eskandar, J. W. Lee, D. Maus, A. Devor, S. I. Fried, P. S. Jones, B. V. Nahed, S. Ben-Haim, S. K. Bick, R. M. Richardson, A. M. T. Raslan, D. A. Siler, D. P. Cahill, Z. M. Williams, G. R. Cosgrove, S. A. Dayeh, S. S. Cash, "Microscale Physiological Events on the Human Cortical Surface Detected with PEDOT:PSS Electrodes", *Cerebral Cortex*, under review.

4. J. C. Yang, A. C. Paulk, **S. H. Lee**, M. Ganji, D. J. Soper, P. Salami, D. R. Cleary, M. Simon, D. Maus, J. W. Lee, B. Nahed, P. Jones, D. P. Cahill, G. R. Cosgrove, C. J. Chu, Z. Williams, E. Halgren, S. A. Dayeh, S. S. Cash, "Microscale Dynamics of Electrophysiological Markers of Epilepsy", in preparation.

5. M. Ganji, A. C. Paulk, J. C. Yang, N. W. Vahidi, **S. H. Lee**, R. Liu, L. Hossain, E. M. Arneodo, M. Thunemann, M. Shigyo, A. Tanaka, S. B. Ryu, S. W. Lee, Y. Tchoe, M. Marsala, A. Devor, D. R. Cleary, J. R. Martin, H. Oh, V. Gilja, T. Q. Gentner, S. I. Fried, E. Halgren, S. S. Cash, S. A. Dayeh, "Selective Formation of Porous Pt Nanorods for Highly Electrochemically Efficient Neural Electrode Interfaces", *Nano Letters* **2019**, 6244-6254.

6. M. Ganji, E. Kaestner, J. Hermiz, N. Rogers, A. Tanaka, D. R. Cleary, **S. H. Lee**, J. Snider, M. Halgren, G. R. Cosgrove, B. S. Carter, D. Barba, I. Uguz, G. G. Malliaras, S. S. Cash, V. Gilja, E. Halgren, S. A. Dayeh, "Development and Translation of PEDOT:PSS Microelectrodes for Intraoperative Monitoring", *Advanced Functional Materials* **2017**, 1700232.

7. R. Liu, R. Chen, A. T. Elthakeb, **S. H. Lee**, S. Hinckley, M. L. Khraiche, J. Scott, D. Pre, Y. Hwang, A. Tanaka, Y. G. Ro, A. K. Matsushita, X. Dai, C. Soci, S. Biesmans, A. James, J. Nogan, K. L. Jungjohann, D. V. Pete, D. B. Webb, Y. Zou, A. G. Bang, S. A. Dayeh, "High Density Individually Addressable Nanowire Arrays Record Intracellular Activity from Primary Rodent and Human Stem Cell Derived Neurons", *Nano Letters* **2017**, 2757-2764.

## PATENTS

1. S. A. Dayeh, R. Chen, **S. H. Lee**, R. Liu, Y. G. Ro, A. Tanaka, Y. Hwang, "Addressable Vertical Nanowire Probe Arrays and Fabrication Methods" US Patent Application No. US2019-0021619A1.

2. S. A. Dayeh, F. Azzazy, **S. H. Lee**, "Flexible Penetrating Cortical Multielectrode Arrays, Sensor Devices and Manufacturing Methods," US Patent Application No. US2017-0231518A1.

## CONFERENCES

### Oral Presentations

1. 2020 Materials Research Society Fall Meeting (2020 MRS), "Scalable Penetrating Microwire Arrays with Flexible Substrate for Chronic Large Area Coverage Brain-Machine Interfaces", **Nov. 2020**, Virtual Meeting.

2. Neuroscience 2016, "Novel 3D Minimal Tissue-Penetrating Probes on Conformal Flexible Substrates for In-Vivo Brain Mapping", **Nov. 2016**, Palm Springs, CA.

3. 2015 Materials Research Society Fall Meeting (2015 MRS), "Novel 3D Minimal Tissue-Penetrating Probes on Conformal Flexible Substrates for In-Vivo Brain Mapping", **Nov. 2015**, Boston, MA.

4. 57th Electronics Materials Conference (EMC 2015), "Novel 3D Minimal Tissue-Penetrating Probes on Conformal Flexible Substrates for In-Vivo Brain Mapping", **Jun. 2015**, Columbus, OH.

5. TechConnect World Innovation Conference & Expo (TechConnect 2015), "Novel 3D Minimal Tissue-Penetrating Probes on Conformal Flexible Substrates for In-Vivo Brain Mapping", **Jun. 2015**, Washington, D.C.

### Poster Presentations

1. Research Expo at UCSD, "Pushing the Boundaries of Brain Mapping with Novel Electronic Materials and Devices", **Apr. 2018**, San Diego, CA

2. Korea University-UCSD Joint MSE Workshop, "Pushing the Boundaries of Brain Mapping with Novel Electronic Materials and Devices", **Aug. 2017**, San Diego, CA.

3. ECE 50-year Anniversary Poster Event, "Pushing the Boundaries of Brain Mapping with Novel Electronic Materials and Devices", **Nov. 2015**, San Diego, CA.

4. The Center for Wearable Sensors Research Summit , "Novel Neural Probe Technologies: Toward High Density, Fidelity, and Flexibility", **Nov. 2014**, San Diego, CA.

**ABSTRACT OF THE DISSERTATION**

Advanced MEMS-Based Scalable Minimally-Invasive 1024 Channel Microneedle and Subdural

Brain and Spinal Cord Implants

by

Sang Heon Lee

Doctor of Philosophy in Electrical Engineering (Nanoscale Devices and Systems)

University of California San Diego, 2021

Professor Shadi A. Dayeh, Chair

Neuromodulation devices are increasingly used in interrogating and treating neurological

dysfunction in the human brain, spinal cord, and peripheral nerves. Recently, there has been an

explosion of interest in applying these devices for brain-machine interfaces and advancing the state-of-the-art interface with the human brain. Toward this end, the Utah array has been the powerhouse of the BrainGate project that partially restored motor and sensory function to patients with neurological injury, though the array itself has advanced little in the last three decades. In this work, we leverage advanced dual-side lithographic microfabrication processes to demonstrate a 1024 channel penetrating Si microneedle array (SiMNA) that is scalable in its recording capabilities and cortical coverage. The SiMNA is built on flexible and transparent substrates permitting simultaneous optical and electrophysiological interrogation of the brain activity and is compliant to brain movements. We use the SiMNA to demonstrate reliable recordings of spontaneous and of evoked field potentials and of single unit activities in chronically implanted mice for up to 196 days in response to optogenetic and to whisker air-puff stimuli. Significantly, the 1024 channel SiMNA established detailed spatiotemporal mapping of broadband brain activity in rats. This novel scalable and biocompatible SiMNA with its multi-modal capability and sensitivity to broadband brain activity will accelerate our progress in fundamental neurophysiological investigations and establishes a new milestone for penetrating and large area coverage microelectrode arrays for brain-machine interfaces.

The reach of soft substrates extends well beyond the curvilinear and pulsating brain toward spinal cord that relays the information bidirectionally to the brain and that has its own processing circuits for fundamental locomotion tasks. Materials that comprise of superior contact properties for recording and stimulation, that are minimally-invasive, and that are biocompatible and flexible have profound impact on the way we record and stimulate activity of the spinal cord. One important application of such devices is to aid in restoring function in spinal cord injury (SCI). However, thresholds for motor recruitment and for tissue damage during direct current stimulation

in the spinal cord using recent microelectrode technologies are not yet established. Additionally, stimulation on the ventral side of the spinal cord in a closer proximity to the motor fibers is advantageous but systematic studies on the efficacy of microelectrode arrays for ventral stimulation versus dorsal stimulation and the stimulation parameters needed for initiation of motor response have not been studied before. This work reports the initiation thresholds for motor recruitment of rodent hindlimb from dorsal and ventral stimulation with various electrode sizes using a newly developed microelectrode material in our laboratory, the platinum nanorod (PtNR) contacts using two device configurations. Device type 1 comprises of microelectrodes of 9 diameters (40/60/80/100/120/140/160/180/200 μm) and a macroelectrode of 250 μm in diameter on sub-10 μm thin flexible parylene-C substrate. Using Device type 1 in the acute setting for dorsal or ventral-lateral spinal cord implantation and electrical stimulation in rats, we quantified lower current thresholds and charge densities, and a lower critical diameter for evoking responses in the sciatic nerves and electromyography responses in hindlimb muscles. Device type 2 consists of three representative diameters (40/100/200 μm) of PtNR electrodes from Device type 1 on sub-10 μm thin flexible polyimide substrate for investigating the stability of the platform on semi-chronic rat implants accompanied by a rigorous stimulation paradigm with a total of over 1 million pulse pairs. This stimulation paradigm is designed based on the a 7-hour stimulation session initially implemented by McCreery et al. In our work, we used a much higher pulse frequency of ~ 200 Hz over the duration of 84 minutes doubling the amount of charge used in McCreery et al.'s work. Device type 3 consists of 128 channels (4 × 32 array) of PtNR electrodes with 30 μm diameter on sub-10 μm thin flexible parylene-C substrate which was used to detect spatiotemporal compound action potentials (CAP) from an acute pig model and demonstrate the high scalability of the device platform.

# Chapter 1

## Scalable Thousand Channel Penetrating Microneedle Arrays on Flex for Multimodal and Large Area Coverage Brain-Machine Interfaces

### 1.1    Introduction: Motivation and Recent Progress and Advances in Neural Interfaces

Neural interface technologies that enable recording of broadband activity are anticipated to revolutionize neuroprosthetics for restoring communication and motor control in patients with neurological injuries, and in neurotherapies for patients with epilepsy, movement disorders, and in neurodegenerative and neuropsychiatric disrupted cognitive processes.[1] To record broadband activity including single units, electrodes that penetrate the cortex (penetrating electrodes) are usually used.[2] Such electrodes were successfully used in intracortical brain computer interfaces (iBCI),[3] the localization and pathophysiology of seizure neurotheraphy,[4] movement disorder therapeutics,[5] and in understanding cognitive processes in the human brain.[6] However, these electrodes are generally highly rigid and can therefore cause damage since they don't move with the brain and their failure is often attributed to connector and material failure issues.[7] Thus further developments were implemented to address the reported issues by demonstrating various geometries of the array shape,[8] and replacing the rigid backplane with dissolvable, biodegradable backplane.[9] Despite geometrically modified arrays' incapability to comply with brain micromotion once implanted and the time consumed to dissolve the backplane is still quite demanding during critical clinical scenarios, these improvements suggest promising features. However more recent studies confirmed that the chronic tissue response is due to tethering forces of the connecting wires.[10] Multiport[11] and multisite Utah arrays[11, 12] were also introduced to

enhance the coverage area and recording resolution of the platform, and electrical recording and stimulation capabilities were further modified by application of iridium oxide[13] and platinum on rough silicon surface.[14] Multimodality of Utah arrays were achieved by simply replacing once of the electrodes with an optrode[15] or fabricating the device entirely on transparent silicate glass for optogentic stimulation and recording,[16] but these approaches are still based on rigid backplane and hinder clear optical visualization of the implantation site, not to mention other hurdles seen by encapsulation material selection for reliable chronic applications.[11]

To overcome these limitations, new electrode technologies have evolved. Ultra-thin flexible threads can reliably record brain activity across the cortical depths and induce minimal scarring to the cortical tissue.[17] Implanting arrays of these neural threads require advanced robotic implanters[18] and the technology is at the dawn of correlating neurophysiological recordings with behavior. Similarly, thin and bendable carbon fiber probes can induce minimal scarring[19] and hand-assembled 16-channel carbon fiber arrays have resulted in single unit recording capability.[20] The absence of a monolithic integration scheme for carbon fibers presents a challenge for their evolution toward an impactful advance in brain-machine interfaces. Thermal drawing process to fabricate fibers were introduced to demonstrate multimodal electrodes for single unit recording by integrating electrical, optical, mechanical, and microfluidic capabilities, but were limited to very small coverage area of a few recording channels per device.[21] Recently, bundled microwire arrays have been used to massively scale the number of recording channels through the integration with high-definition CMOS acquisition circuits,[22] and was scaled to 65,536 channels in the Argo system.[23] Non-lithographically patterned and arranged microwire arrays in the Argo system can cause significant volumetric damage to the brain structure and as a result, it has been implemented for surface recordings in sheep animal model.[23] The Argo system also has a rigid packaging at

the back of the array to facilitate integration with the CMOS electronics and can be used as a remote connector to flexible neural interface platform,[23] such as the one described in this work.

The objective of this work is to demonstrate a clinically translatable version of the Utah array, that is scalable to large area cortical coverage with a backing that is thin, flexible and compliant to brain movements. To this end, we devised a novel fabrication procedure[24] that permits the realization of dense out-of-plane SiMNAs. Using standard microfabrication techniques, we were able to control the microscale electrochemical interface to achieve low electrochemical impedances using platinum nanomesh (PtNM) contacts.[25] With its transparent polyimide substrate, the SiMNA allow the simultaneous optical and electrophysiological intervention in the chronic setting.[26] We discuss the fabrication and the development of implantation procedures of the SiMNAs in benchtop experiments. We also demonstrate their broadband electrophysiological recording capabilities, as well as two-photon imaging, optogenetic-electrophysiological interrogations in the chronic setting using a proof-of-concept 32ch SiMNA. We then demonstrate the recording capabilities of the 1024 SiMNA in the acute rat animal experiments demonstrating high spatiotemporal mapping in the rat brain.

## 1.2 Experimental Details

### 1.2.1 Device Fabrication

#### 1.2.1.1 Overview of the 32 Channel Si Microneedle Array Fabrication Process on Flexible Substrates

The fabrication begins with a 100 μm-thick, double side polished, n-type silicon wafer with low resistivity of 0.002-0.005 Ω-cm for the preparation of reliable ohmic contact between the metal adhesion layers Cr and Ti, and the silicon microneedle at the top and bottom, respectively, later in

the process. The wafer is cleaned using standard solvent cleaning procedure followed by acidic solution (acidic piranha, $H_2SO_4/H_2O_2$) to remove organic contaminants, and the final buffered oxide etchant (BOE 6:1, Sigma-Aldrich) to remove the resulting oxide layer. The wafer is then spin-coated with 5 μm-thick polyimide (PI2611, HD Microsystems), and cured in nitrogen-purged oven (HTCR, Carborlite) at maximum temperature of 300 °C. 40 nm Ti was electron-beam evaporated (e-Beam Evaporator 2, Temescal) on the polyimide side of the wafer to serve as the hard etch mask for the later step of dry etching of vias in the 1st layer of polyimide. Photolithography was performed to define the via sites and mask the rest of the underlying Ti layer, followed by reactive ion etching (RIE, Plasmalab 80+, Oxford Instruments) with $SF_6/Ar$ to etch the Ti in the via sites. The remaining photoresist (NR9-3000PY, Futurrex, Inc.) was removed with solvents and the exposed polyimide on the via sites are RIE etched with $O_2$. The wafer was then dipped in BOE to remove the polyimide ashes from the RIE process on the vias, and the remaining Ti etch mask. Photolithography was performed again on the polyimide side of the wafer to define the ohmic contact and the metal leads. The wafer was descummed with $O_2$ (Plasma Etch 100, Oxford Instruments) and then treated with BOE to remove the native oxide on the Si surface at the via sites and swiftly loaded for electron-beam evaporation of the following: first layer of 20 nm Ti for ohmic contact with the Si, then 80 nm Ni which later serves as the etch stop layer for deep reactive ion etching (DRIE), and finally 10 nm Cr to prevent oxidation of the metal layers. The wafer was then transferred to Denton Discovery 18 Sputter System to sputter 250 nm Ti for conformal electrical connection between the proceeding metal stack at the vias and the metal leads on the surface of the polyimide. The polyimide side of the wafer is spin-coated and cured again with 5 μm-thick polyimide to encapsulate the metal layers. (Figure 1.1a)

After RIE etching residual polymer residue and oxide on the exposed Si side of the wafer with $O_2$ and $CHF_3/Ar$, respectively, the wafer was flipped upside down for the novel backside-alignment process (MA6 Mask Aligner, Karl Suss) to photolithographically define another array of ohmic contacts, which in part, serves as the DRIE etch mask to form "sacrificial Si pillars" on the exposed Si side of the wafer. The wafer was descummed with $O_2$, the native oxide was removed on the Si surface with BOE, and then sputtered with 15 nm Cr for the ohmic contact, 100 nm Pt, and finally ~0.5 μm Pt-Ag alloy was deposited by co-sputtering technique in which the power was set at 400 W for Ag, and 100 W for Pt. (Figure 1.1b)

The wafer was immediately transferred to electron beam evaporate 10 nm Ti as the adhesion layer between Pt-Ag alloy and Ni, and finally 50 nm Ni to serve as the DRIE etch-stop layer later in the process. (Figure 1.1c) After lifting off residual metal stacks, the polyimide side of the wafer was carefully bonded to a carrier wafer (500 μm-thick, single side polished Si wafer) with photoresist (NR9-6000PY, Futurrex, Inc.) then baked at 150 °C for 1 min. DRIE (Plasmalab 100, Oxford Instruments) was used to perform a 2-step etch process (Bosch process, or combination of isotropic plasma etch with $SF_6$, and passivation with $C_4F_8$) to remove Si and leaving an array of 100 μm-tall, vertical Si micropillars underneath the predefined Cr/Pt/Pt-Ag/Ti/Ni metal stack. (Figure 1.1d) During this process, the additional metal stack of Cr/Pt/Pt-Ag/Ti/Ni also leaves sacrificial/protecting Si pillars (Figure 1.3), defined around the actual Si micropillar array to be served as the electrodes. These additional sacrificial/protecting pillars assist with the fine control of the etch profile, or the tapering angle of the DRIE etched pillars, by modifying the density of the array.[27, 28] These sacrificial/protecting pillars have relatively weaker bonding to the underlying polyimide substrate when compared to the actual electrode Si

microneedle supported on the exposed metal contact at the base. This allows a simple process of breaking off the sacrificial/protecting pillars with a micromanipulator setup.

The device is released from the carrier wafer, and coated with 1 μm-thick parylene-C layer (SCS Labcoter 2 Parylene Deposition System, Specialty Coating Systems) to passivate the entire device. (Figure 1.1e)

The device was remounted to a carrier wafer with the Si microneedles facing up. The polyimide/parylene-C substrate of the device was slowly spin-coated with photoresist (NR9-6000PY, Futurrex, Inc.) and then baked without UV exposure. The photoresist layer was dipped in developer (RD6, Futurrex, Inc.) for up to 10 s, much shorter than the usual photolithography process. This removes the thinner layer of photoresist at the tip of the Si microneedles without exposing the other protected areas of the polymer substrate, allowing selective RIE with $O_2$ to remove the parylene-C layer only at the tip of the microneedles. The remaining oxidized photoresist is removed with the same developer to prevent residues which may occur from conventional solvent cleaning technique. The Ni mask at the exposed tip of the Si microneedles was removed with Ni etchant (Ni etchant TFB, Transene Company, Inc.) and the underlying Ti layer was removed with BOE. Then the Pt-Ag was de-alloyed by removing the Ag component from the alloy with $HNO_3$ heated at 60 °C for 2 min which leaves the final PtNM electrode surface at the tip of the Si microneedles. (Figure 1.1f)

The device was again RIE etched while covering the array region with glass sides without damaging the array region, and only exposing the electrical contact pads embedded in polymer substrate on the opposite end with regard to the Si microneedle array. Lastly, the device was released from the carrier wafer and bonded with conductive epoxy (Silver Conductive Epoxy Adhesive, MG Chemicals) to a custom connector PCB.
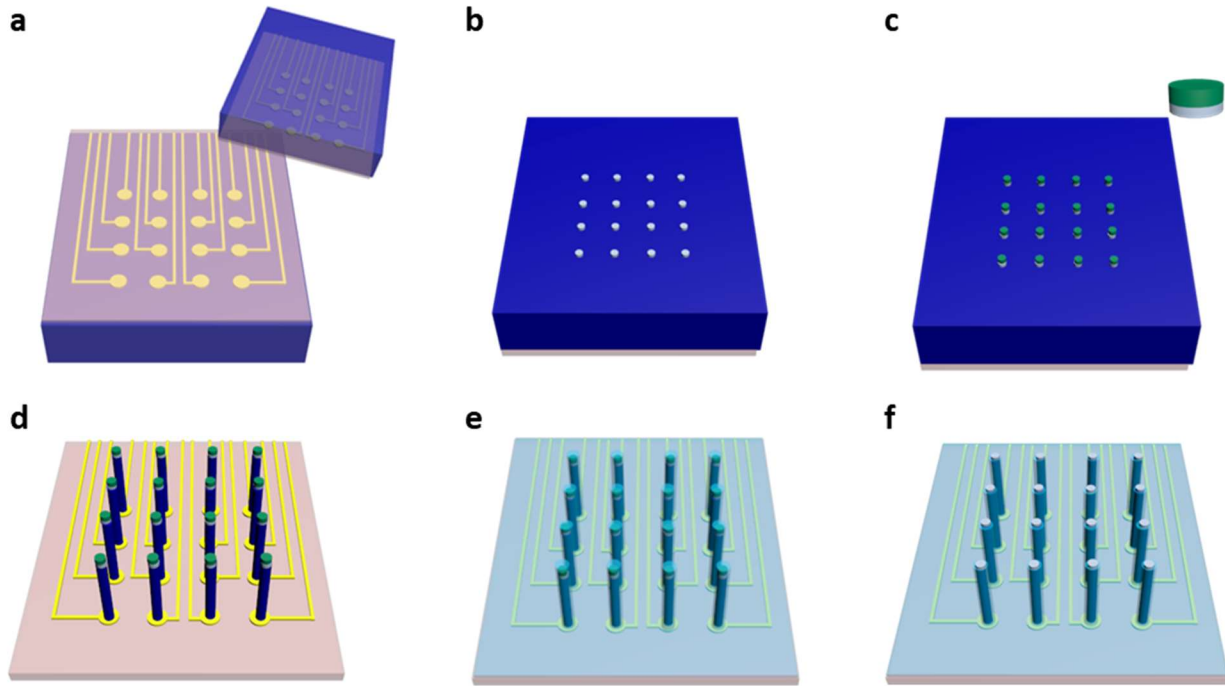
**Figure 1.1** Fabrication process flow of 1024ch SiMNA on flexible substrate. (a) Polyimide layers (~10 μm total thickness) and metal lead stack (E-beam evaporate 20 nm Ti, 80 nm Ni, 10 nm Cr, and then sputter 250 nm Ti) deposited on 100 μm-thick heavily doped n-type Si wafer. Inset shows the wafer flipped view for back-side alignment. (b) Back-side alignment photolithography and sputter 15 nm Cr, 100 nm Pt, and co-sputter ~0.5 μm of Pt and Ag (PtAg alloy). (c) E-beam evaporate 10 nm Ti and 50 nm Ni. (d) DRIE (Bosch process) to form SiMNA structure. (e) Deposit 1 μm parylene-C layer. (f) Selectively dry etch the SiMN tips, wet etch Ni with Ni etchant, Ti with BOE and then Ag in the PtAg alloy with $HNO_3$ to form PtNM structure.

The schematic diagram and magnified images of the final devices are shown in Figure 1.2. Each microneedle has a high aspect ratio of 10, with 100 μm height and 10 μm diameter, which are encapsulated in polyimide and parylene-C to ensure biocompatibility for chronic implantation in animal models. The tip of the electrode acts as the active sensing area, which is coated with nanoscale mesh structure of platinum, or Pt nanomesh (PtNM), to lower the electrode impedance. Figures 1.2a and 1.2b show the two different pitches of the device, with microneedle-to-microneedle spacing of 50 μm and 400 μm, representing the highly customizable density of the array.
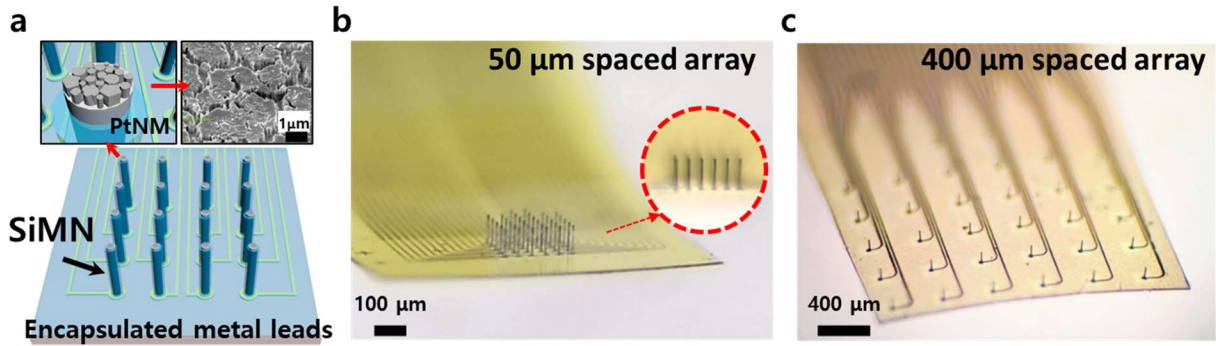
**Figure 1.2** 32ch SiMNA on flexible substrate. (a) Schematic diagram of the device highlighting the key components; PtNM electrode at the tip of the SiMN, metal leads, and encapsulation layers. (b) A magnified image of the 50 μm spaced array. (c) A magnified image of the 400 μm spaced array.

### 1.2.1.2 Optimization of the 32 Channel SiMNA Etching Process

One of the key challenges in the fabrication of Si microneedle arrays on flexible substrate was the formation of the high aspect ratio microneedles with dry etch process. In order to allow sufficient mechanical stability, achieve high aspect ratio morphology of the microneedle, and reliable yield of microneedles per device, we applied dry etch processes of continuous inductively coupled plasma-reactive ion etching, or RIE/ICP, and 2-step deep reactive ion etching process (2-step DRIE, or Bosch). However, as shown in Figure 1.3, both approaches led to the undesired negative tapering profile, or tapering angle of below 90°, which would later hinder the penetration of the microneedles. A systematic study on the DRIE parameters for vertically aligned micropillar arrays[29] suggested possible options to overcome this processing issue, but was only applicable to very high density arrays of pitch size of a few microns, thus inappropriate for our goal of fully customizable micropillar array that allows one to also change the array density in the range of tens or hundreds of microns. The concept of sacrificial or protecting pillars were introduced to form high aspect ratio microelectrode arrays for intracellular recording and in vitro mapping of neural activity,[27, 28] despite the limitations such as only having one electrically function channel,[27] and

8

being supported on rigid substrate,[28] these methods were invaluable inspirations toward the development of a new process that allows fabrication of high aspect ratio microneedles with customizable array density on flexible substrate.
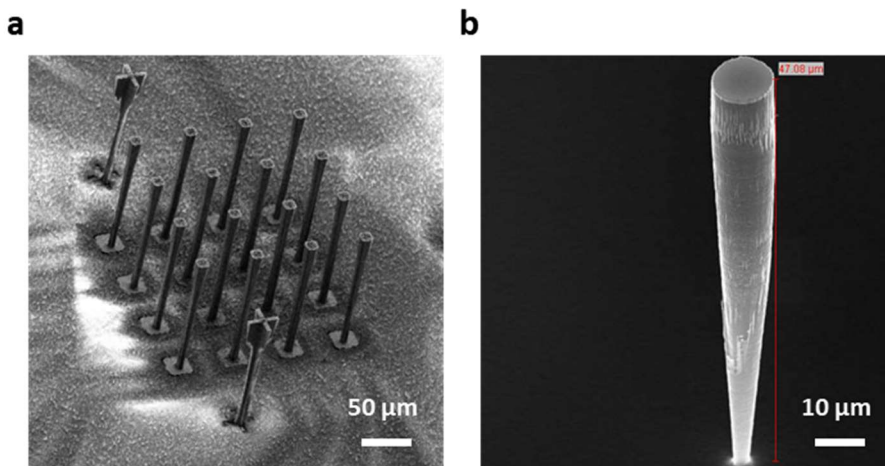


**Figure 1.3** Prototype devices using conventional RIE/ICP and 2-step DRIE. (a) A device using continuous RIE/ICP etch results in tapering of microwire with the base thinner than the tip. (b) 2-step DRIE (Bosch etch) on a single Si microwire with undesired tapering similar to (a).

For the denser, 50 µm microneedle-to-microneedle spacing array, we utilized the sacrificial pillar method similar in design with the previously reported work, as shown in Figure 1.4a.[27] For the 400 µm microneedle-to-microneedle spacing array, we altered the design from Figure 1.3a to Figure 1.4b. In a more sparsely spaced microwire array, the shadowing effect provided by the sacrificial pillars during the 2-step DRIE process is not sufficient to protect the region near the base of the electrically functional microwire, highlighted in red circle in Figure 1.4. Thus, we replaced the sacrificial pillars that are smaller in diameter than the electrically functional microwire with protecting pillars that are the same size as the functional microwire (Figure 1.4b). Both designs of sacrificial and protecting microwires are all located outside the boundary of the ohmic contact, highlighted as green circle in Figures 1.4, 1.5 and 1.6, with the underlying metal leads, whereas the electrically functional microwire sits in the center of the ohmic contact.
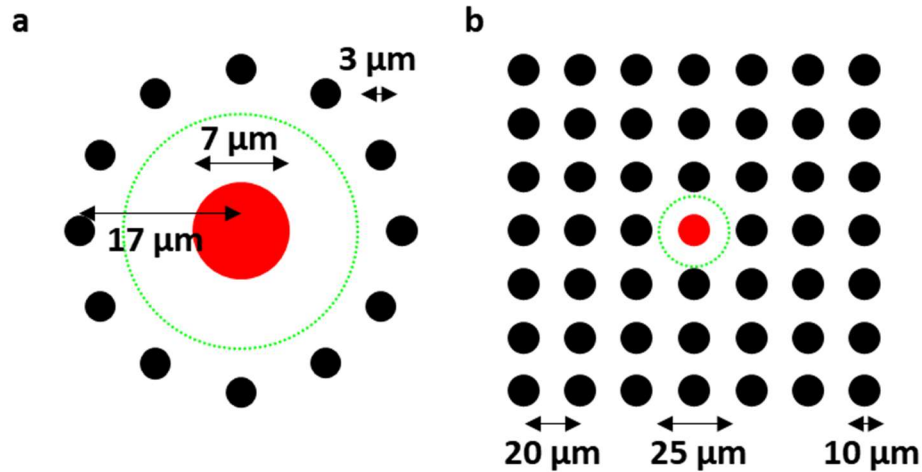
**Figure 1.4** Etch mask designs for 50 μm and 400 μm microneedle-to-microneedle spacing array. (a) A single microwire (red) surrounded by 12 sacrificial microwires (black), for a 50 μm microneedle-to-microneedle spacing array. (b) A single microwire (red) surrounded by 48 sacrificial microwires (black), for a 400 μm microneedle-to-microneedle spacing array.

The 2-step DRIE (Bosch etch) yielded the best dry etch results for the test samples of both 50 μm and 400 μm microneedle-to-microneedle arrays as shown in Figure 1.5. We further finetuned the etch recipe to achieve the desired tapering angle of 90° or higher. A 2-3 min $O_2$ plasma was performed to clean the surface of the Si wafer from organic contaminants before the main 2-step DRIE. Then the 2-step DRIE was set to cycle through a sequence of the main etch step ($SF_6$ 100 sccm, $C_4F_8$ 1 sccm, RIE 40 W, ICP 1000 W, at 35 mTorr for 8 s), passivation step ($SF_6$ 1 sccm, $C_4F_8$ 100 sccm, RIE 12 W, ICP 1000 W, at 35 mTorr for 7 s), and the transition step ($SF_6$ 75 sccm, $C_4F_8$ 25 sccm, RIE 20 W, ICP 1000 W, at 35 mTorr for 2 s). Dry etching a 100 μm-thick Si wafer required a total of about 400-500 cycles of this 2-step DRIE which was broken down to small sets of cycles in sequence with short break times in between such as 200 cycles, 100 cycles, 50 cycles, 20 cycles, and 10 cycles and then finally 5 cycles to slowly control the exposure of the underlying polyimide, without inducing over etch of the desire Si microneedle array.

10
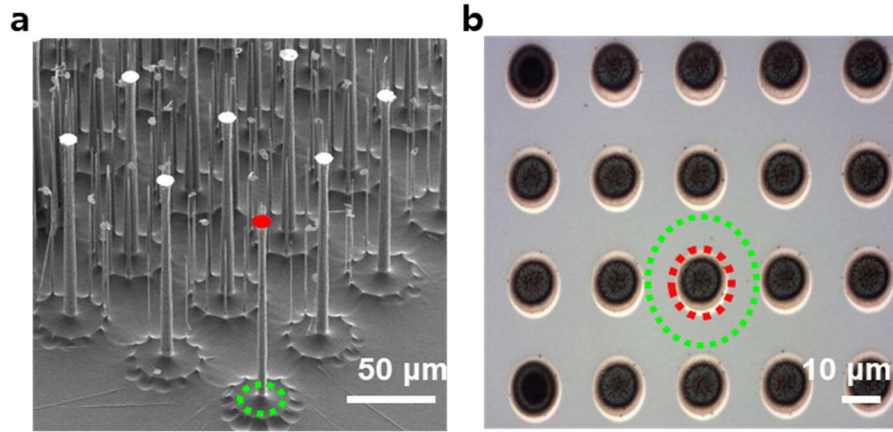
**Figure 1.5** Etch results from test samples of 50 µm and 400 µm microneedle-to-microneedle spacing array. (a) SEM image during 2-step DRIE of a test sample of 50 µm microneedle-to-microneedle spacing array. (b) A magnified image showing top side view of a test sample of 400 µm microneedle-to-microneedle spacing array.

The final morphology of the Si microneedle is shown in Figure 1.6. The tapering angle was between 90° and 91°, resulting in the tip of the microneedle with diameter of either the same or slightly smaller than the diameter of the microneedle at the base where it forms an ohmic contact with the underlying metallization through the vias of the polyimide layer. The height of the microneedle was around 100 µm and the diameter at the tip was around 10 µm. The focused ion beam cut was used to obtain cross-sectional images at the interface of the ohmic contact. In Figures 1.6b and 1.6c, the via region of the polyimide layers is where the Si microneedle forms the ohmic contact with the metal stack of 20 nm Ti / 80 nm Ni / 10nm Cr which is then conformally connected through 250 nm of Ti with the rest of the metallization in the middle of the first and second layers of polyimide. A passivation layer of parylene-C with about 1 µm thickness encapsulates the entire device around the polyimide layers and the sidewall of the microneedle, while only the tip of the microneedle is exposed with the PtNM electrode.
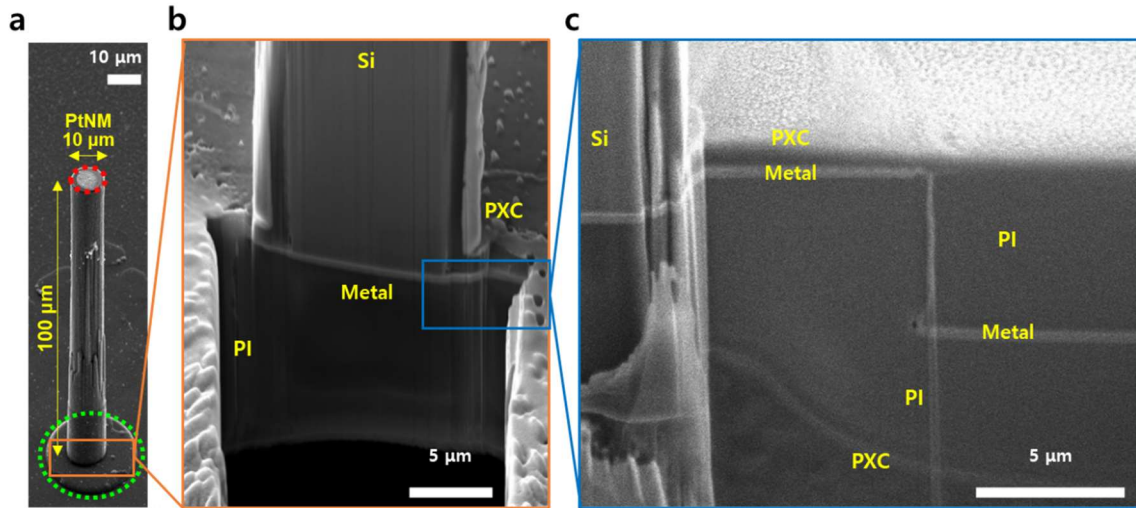
**Figure 1.6** The final morphology of a single Si microneedle. (a) SEM image of a single microneedle. (b) FIB-cut, cross-sectional image of the ohmic contact at the base of a microneedle. (c) FIB-cut, cross-sectional image of the conformal metallization in between the encapsulation layers of polyimide and parylene-C.

### 1.2.1.3 Overview of the 1024 Channel Si Microneedle Array Fabrication Process on Flexible Substrates

The fabrication begins with a 500 μm-thick, double side polished, n-type silicon wafer with low resistivity of 0.001-0.005 Ω-cm for the preparation of reliable ohmic contact between the metal adhesion layer of Cr and the silicon microneedle at the top and bottom of the final Si microneedle later in the process. The wafer is cleaned using standard solvent cleaning procedure followed by buffered oxide etchant (BOE 6:1, Sigma-Aldrich) to remove the resulting oxide layer. The wafer is then spin-coated with 5 μm-thick polyimide (PI2611, HD Microsystems), and cured in nitrogen-purged oven (HTCR, Carbolite) at maximum temperature of 300 °C. 50 nm Ti was electron-beam evaporated (e-Beam Evaporator 2, Temescal) on the polyimide side of the wafer to serve as the hard etch mask for the later step of dry etching of vias in the 1st layer of polyimide. Photolithography was performed to define the via sites and mask the rest of the underlying Ti layer, followed by reactive ion etching (RIE, Plasmalab 80+, Oxford Instruments) with $SF_6$/Ar to etch

12

the Ti in the via sites. The remaining photoresist (NR9-3000PY, Futurrex, Inc.) was removed with solvents and the exposed polyimide on the via sites are RIE etched with $O_2$. The wafer was then dipped in BOE to remove the polyimide ashes from the RIE process on the vias, and the remaining Ti etch mask. Photolithography was performed again on the polyimide side of the wafer to define the ohmic contact and the metal leads. The wafer was descummed with $O_2$ (Plasma Etch 100, Oxford Instruments) and treated with BOE to remove the native oxide on the Si surface at the via sites and swiftly loaded to Denton Discovery 18 Sputter System to deposit 15 nm Cr for ohmic contact with the Si, then 100 nm Pt for conformal electrical connection. The polyimide side of the wafer is spin-coated and cured again with 5 μm-thick polyimide to encapsulate the metal layers. (Figure 1.7a)

After RIE etching residual polymer residue and oxide on the exposed Si side of the wafer with $O_2$ and $CHF_3/Ar$, respectively, the wafer was flipped upside down for the novel backside-alignment process (MA6 Mask Aligner, Karl Suss) to photolithographically define a grid to serves as the alignment guidelines for the dicing step later in the process. The wafer was descummed with $O_2$, the native oxide was removed on the Si surface with BOE, and then electron beam evaporated with 50 nm Ti. (Figure 1.7b)

The polyimide side of the wafer was bonded to a carrier wafer (500 μm-thick, single side polished Si wafer) with photoresist (NR9-6000PY, Futurrex, Inc.) then baked at 150 °C for 1 min. The combined wafer was mounted to an automatic dicing saw system (DAD3220, Disco) for the dicing process. The dicing saw was aligned with the Ti grid on the top Si surface and was programmed to make partial cuts at blade feed speed of 0.5 mm/s, creating 470 μm-deep, 300 μm-wide trenches in between the micropillars, each with the tip area of around 100 μm × 100 μm. This forms a 58 × 58 array of Si micropillars of which the 32 × 32 array in the center are the Si

microneedle electrodes in the final device. The surrounding micropillars which allows ease of handling and serve as the "buffer zone" during the later wet etch process for more uniform length of the final Si microneedle electrodes. (Figure 1.7c)

The diced wafer was unmounted from the dicing saw system and the Si micropillars were thinned down by isotropically dry etching with $XeF_2$ ($XeF_2$ Etcher, Xactix) until the micropillar tip area was about 90 μm × 90 μm. The wafer was transferred for DRIE (Plasmalab 100, Oxford Instruments). The 2-step etch process (Bosch process, or combination of isotropic plasma etch with $SF_6$, and passivation with $C_4F_8$) etches away the thin, residual Si near the base of the Si micropillars to electrically isolate them from each other. The device is released from the carrier wafer and the large Si pieces surrounding the array region were manually peeled off from the polyimide substrate. The Si micropillars were further sharpened with Si etchant solution ($HF/HNO_3$) for around 2-5 min, similar to the "static etch" utilized to fabricate UEAs.[30] (Figure 1.7d)

All surviving additional, electrically-nonfunctional Si micropillars in the "buffer zone" are removed using the micromanipulator setup similar to the process described in the fabrication of the 32ch device. The device was remounted to a carrier wafer with the Si microneedles facing up by laminating the device on the carrier wafer spin-coated with photoresist (NR9-6000PY, Futurrex, Inc.) then baked without UV exposure. 4 small (about 5mm × 1.8 mm each) 500 μm-thick Si pieces were bonded with photoresist to form a square frame surrounding the array, on top of the polyimide substrate. Similar to the preparation of "selective RIE step" in the fabrication of 32ch device, this later allows thicker coating of photoresist for the Si microneedles. The mounted device again spin-coated 2 times with the same photoresist at slower spin speed of 1000 RPM, and 1 spin-coat at 500 RPM, with 5 min vacuum and 5 min pre-bake in between each spin-coat. The wafer is then cured

oven for 2 h at 80 °C, and dipped in developer (RD6, Futurrex, Inc.) for up to 20 s with agitation. This removes the thinner layer of photoresist at the tip of the Si microneedles without exposing the other areas coated with the photoresist. Any residual photoresist at the tips was descummed with $O_2$, the native oxide was removed on the Si surface with BOE, and then sputtered with 15 nm Cr for the ohmic contact, 100 nm Pt, and finally ~0.5 μm Pt-Ag alloy was deposited by co-sputtering technique in which the power was set at 400 W for Ag, and 100 W for Pt. (Figure 1.7e)

The device is released from the carrier wafer, and coated with 2 μm-thick parylene-C layer (SCS Labcoter 2 Parylene Deposition System, Specialty Coating Systems) to passivate the entire device. The coated device was laminated to a carrier wafer with the same procedure detailed in the earlier steps of the fabrication. A custom etch mask was prepared using the laser cutter (ULS 3.5, Universal Laser Systems) to puncture holes in stencil film (2 Mil polyester tape with silicone adhesive, APT) which was temporarily mounted to the device. The punctured holes or vias on the stencil mask are aligned with the electrical contact pads region at the other end from the Si microneedle array. The polyimide/parylene-C layers embedding the contact pads were RIE etched with $O_2$ through the vias in the stencil mask while other exposed regions were covered with glass sides without damaging the array region. The stencil mask was removed after the contact pads are fully exposed and the same multistep photoresist spin-coating technique used for Pt-Ag alloy deposition was performed to selectively RIE etch the parylene-C layer with $O_2$, that is passivating the tip of the Si microneedles. Then the device was released from the carrier wafer, and the exposed Pt-Ag was de-alloyed by removing the Ag component from the alloy with $HNO_3$ heated at 60 °C for 2 min which leaves the final PtNM electrode surface at the tip of the Si microneedles. Lastly, and bonded with conductive epoxy (Silver Conductive Epoxy Adhesive, MG Chemicals) to a custom connector PCB. (Figure 1.7f)

15
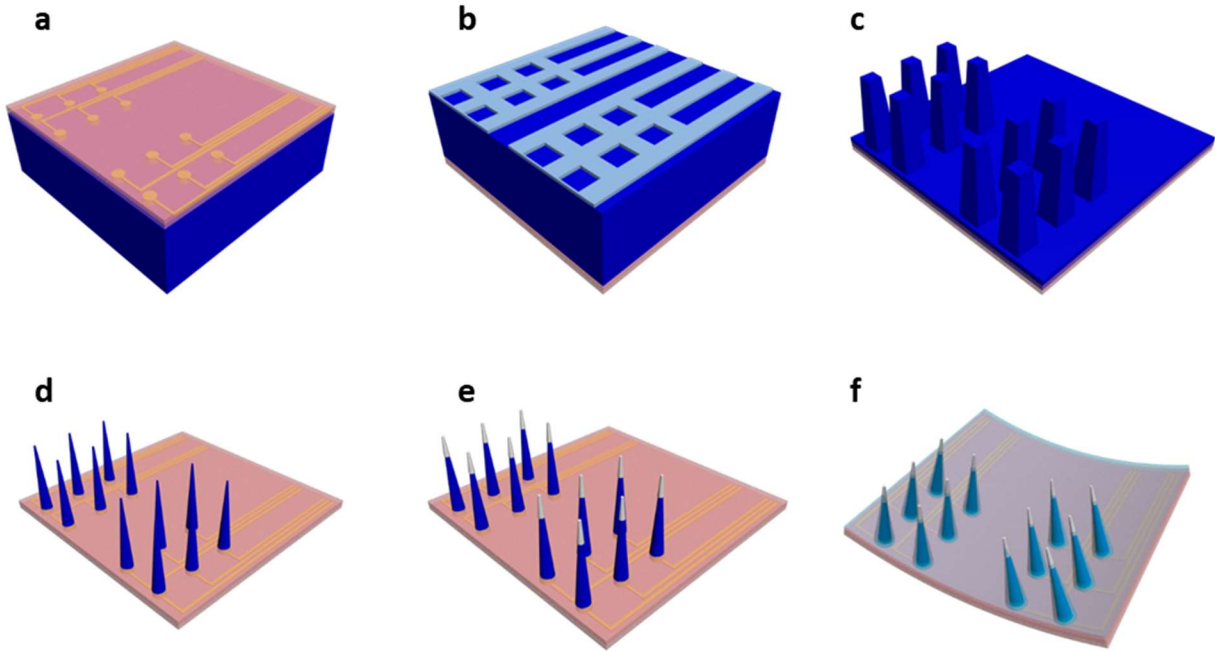
**Figure 1.7** Fabrication process flow of 1024ch SiMNA on flexible substrate. (a) Polyimide layers (10 μm total thickness) and metal lead stack (sputter 15 nm Cr and 100 nm Pt) deposited on 500 μm-thick heavily doped n-type Si wafer. (b) Flip the wafer, back-side alignment photolithography and E-beam evaporate 50 nm Ti. (c) Dicing saw creates ~300 μm wide, ~470 μm deep trenches between SiMNs. (d) Isotropic $XeF_2$ dry etch, 2-step DRIE, and wet etch with $HF:HNO_3 = 1:19$ to sharpen the SiMNs. (e) Selectively sputter 15 nm Cr, 100 nm Pt, and selectively co-sputter 0.5 μm of Pt and Ag (PtAg alloy). (f) Deposit 2 μm parylene-C layer and selectively dry etch the SiMN tip and then wet etch Ag in the PtAg alloy to form PtNM structure.

The magnified images of the final device are shown in Figure 1.8. The microneedle-to-microneedle spacing was 400 μm and each microneedle was around 200-300 μm in height, base size of around 70 μm × 70 μm, and very sharp, submicron tips, which are encapsulated in polyimide and parylene-C to ensure biocompatibility for acute implantation in rodent models. The top 80-100 μm region at the tip of the electrode acts as the active sensing area, which is coated with nanoscale mesh structure of platinum, or Pt nanomesh (PtNM), to lower the electrode impedance.
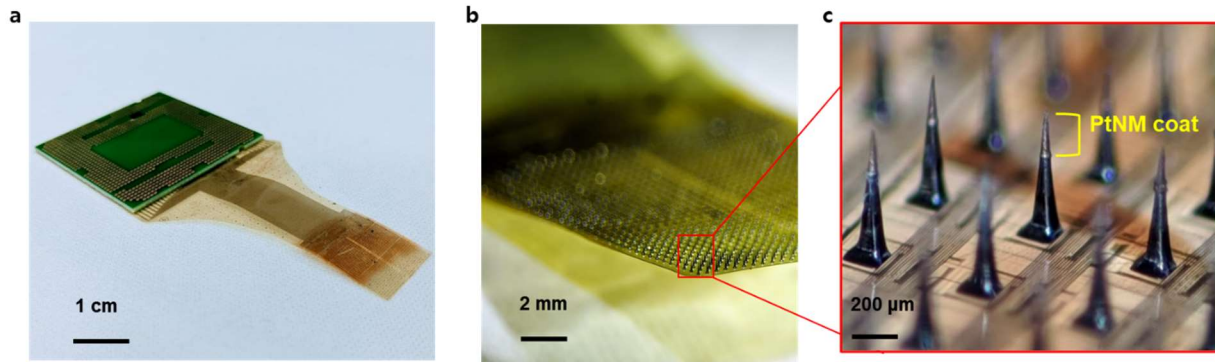
**Figure 1.8** 1024ch SiMNA on flexible substrate. (a) An overview image of the fabricated device bonded to a custom LGA socket connector PCB; PtNM electrode at the tip of the SiMN, metal leads, and encapsulation layers. (b) A magnified image of the 1024ch SiMNA on flex. (c) A magnified image of the representative SiMN with PtNM coating at the tip.

### 1.2.1.4 Optimization of the 1024 Channel SiMNA Etching Process

We combined our fabrication techniques from the 32ch devices for smaller animal models, with the manufacturing process used in the Utah electrode arrays[31] to enable monolithic, and scalable fabrication of thousands of microneedles on an array on flexible substrate. The backside alignment technique used in the fabrication of 32ch devices was also applied here to align the ohmic contacts with the desired Si micropillars to be formed on the other side of the wafer. Similar to the dicing procedure used in Utah arrays, the dicing saw system forms ~470 µm-deep and ~300 µm-wide trenches, thus leaving residual Si micropillars aligning with the metal contacts in the via regions of the polyimide (Figure 1.9a). The Si micropillars were thinned down by isotropic dry etching with $XeF_2$, followed by 2-step DRIE (Bosch etch) to selectively etch the remaining Si near the base of the Si micropillars for electrical isolation between the final Si microneedles (Figure 1.9b). The 2-step etch process used the same recipe as the one used in the fabrication of 32ch device but with a total of around 50-70 cycles which was sufficient to expose the underlying polyimide layer. The device is then released from the carrier wafer and the large Si pieces surrounding the array region were manually peeled off from the polyimide substrate, in preparation

of the wet etch process to sharpen the micropillars into sharp microneedles. The Si etchant solution of HF:HNO₃=1:19 at room temperature for a total of around 5 min, similar to the "static etch" utilized to fabricate UEAs.[30] (Figure 1.9d) The final morphology of the microneedle is shown in Figure 1.9e. The selective coating technique using photoresist is shown in Figure 1.9f, in which the microneedles are partially submerged in the photoresist coating while the tips are exposed. This allows both the selective coating of PtNM and selective dry etching of parylene-C passivation layer, later in the fabrication process.
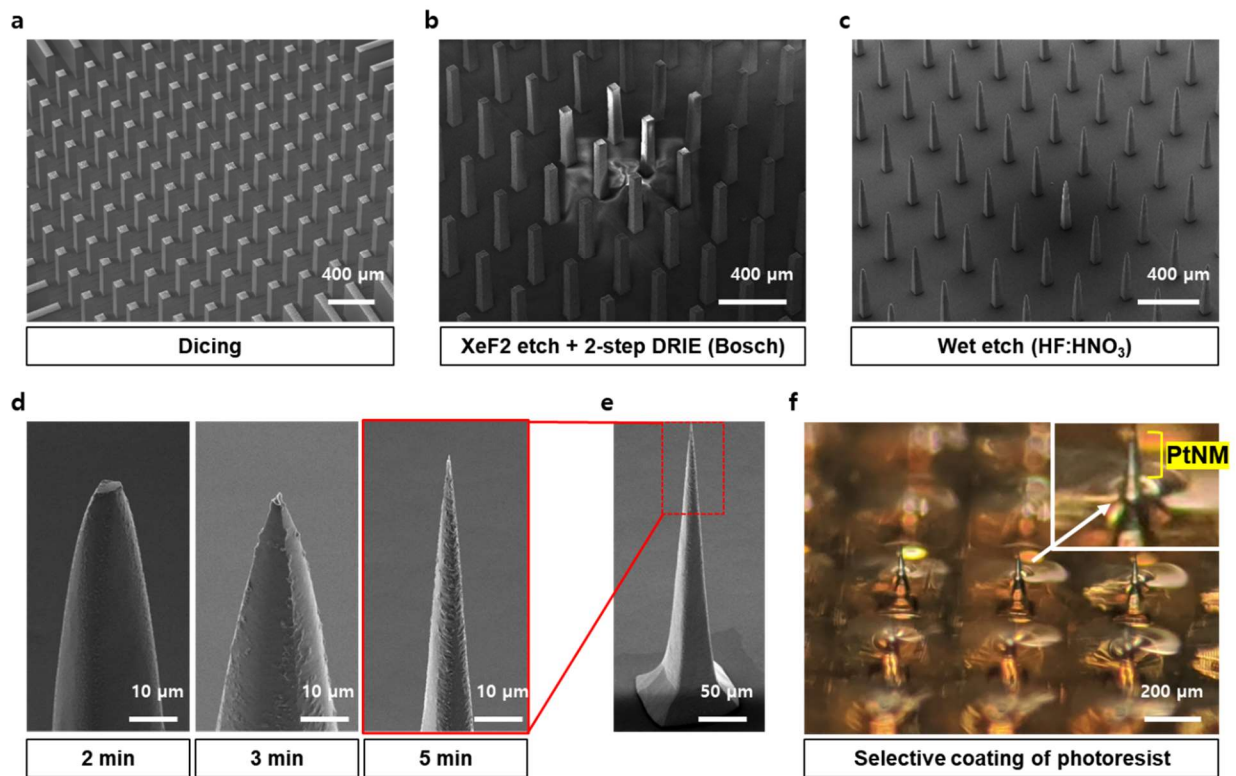


**Figure 1.9** The etching process of sharp microneedles in 1024ch SiMNA on flex. (a) A test device after dicing trenches on the Si wafer. (b) A test wafer after isotropic and anisotropic dry etch processes. (c) A test wafer after 2 minutes of wet etch. (d) Progression of microneedle tip morphology depending on the wet etch process time. (e) Morphology of the final, sharp Si microneedle suitable for implantation. (f) Selective coating of photoresist on SiMNA.

### 1.2.1.5  Electrode Impedance Control by Surface Material Coating

The electrical performance of the device was improved through various revisions of the electrode surface material coating. The initial approach was to conformally coat the Si microneedle with titanium layer on both the tip and the sidewall of the microneedle as shown in Figure 1.10a. Despite successful lowering of the electrical impedance when compared to the bare Si, this method would hinder the brain layer-to-layer analysis. In order to control the depth at which the microneedle records brain activity, we altered the process to passivate the sidewall and the exposed metal contact at the base of the Si microneedle as shown in Figure 1.10b, 1.10c and 1.10d. Our second approach was to either galvanostatically or potentiostatically electrodeposit a conductive polymer, poly(3,4-ethylenedioxythiophene) (PEDOT:PSS), on top of the 10 nm Ti / 50 nm Ni tip of the microneedle which was used as etch mask for the previous 2-step DRIE process. As shown in Figures 1.10c and 1.10d, The other approaches were to replace this PEDOT:PSS with monolithically defined platinum nanorods (PtNR) and platinum nanomesh (PtNM). The original ohmic contact of Ti/Ni with the Si microneedle at the tip was replaced with 15 nm Cr and 100 nm Pt, before defining either PtNR or PtNM.
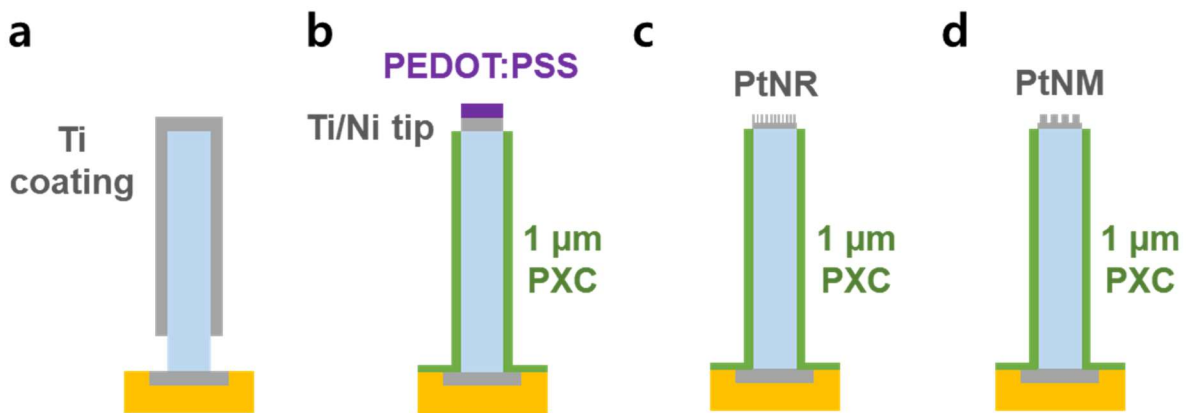


**Figure 1.10** The revision of the electrode surface material coating. (a) Conformal Ti coating of the Si microneedle. (b) Passivation of the sidewall and the electrodeposition of PEDOT:PSS at the tip of the microneedle. (c) Passivation of the sidewall and the deposition of PtNR at the tip. (d) Passivation of the sidewall and the deposition of PtNM at the tip.

**1.2.1.6  Development of Custom Connectors and Rodent Headposts for Chronic Recordings**

The chronic implantation of our device into the mouse cortical tissue requires the mouse to move freely while not recording. This calls for the development of a custom headmounts and headposts to secure the device and the animal model, along with the connector printed circuit board (PCB) that enables electrical connection to the device with the recording system. Figure 1.11a shows a sample device that is bonded to the custom connector PCB designed in our laboratory. The exposed Ti metal contact pads on the device after fabrication is bonded to one side of the PCB with gold contact pads using a conductive epoxy (Silver Conductive Epoxy Adhesive, MG Chemicals) at an elevated temperature of 60 °C for over an hour. This allows individual addressing of each microneedle, or channel, with the gold contacts on the zero-insertion-force (ZIF) connector on the other side of the custom connector PCB, which then allows one to electrically connect the device to the recording system with a flexible flat cable (FFC, highlighted orange in Figure 1.12a).
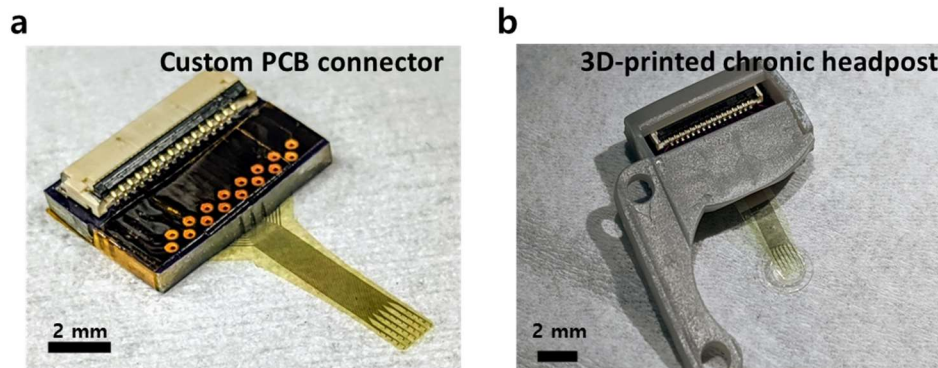


**Figure 1.11** Custom designed connector PCB and 3D-printed chronic headpost. (a) An image of the 32ch SiMNA on flex bonded the custom connector PCB. (b) An image of the device bonded the custom connector PCB that is encased in the 3D-printed chronic headpost before implantation.

Once the device is bonded to the connector PCB, a custom 3D-printed headpost (Figure 1.11b, and highlighted yellow in Figure 1.12a) encases the PCB and secures the device on the mouse head with the custom titanium head frame, highlighted in red, as illustrated in Figure 1.12a.

In order to maintain the chronic optical access, we bonded the array with transparent, ultraviolet-curable glue (Norland Optical Adhesive 61) on a chronic glass cranial window[32] with ~3 mm inner diameter, ~5 mm outer diameter, and total thickness of ~1 mm (Figure 1.12b).
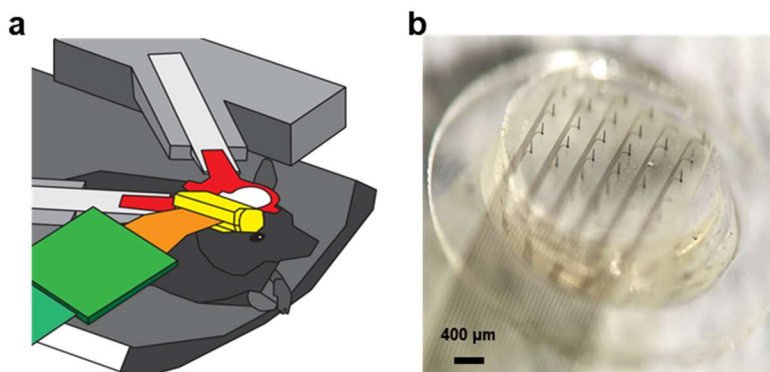


**Figure 1.12** Setup for mouse head fixture and cranial window for SiMNA. (a) A schematic diagram of the frame, headmount, headpost, and electrical connection to the recording system. (b) A magnified image of the device bonded custom cranial window.

### 1.2.1.7  Connectorization to Custom LGA Socket Connecter PCB

Similar to the connectorization of 32ch device detailed in the previous section, the 1024ch SiMNA of flex also needed a custom connector PCB for the electrical connection to the recording system. We modified Intel's LGA1155 socket design to make custom LGA socket connector PCB which was bonded to the exposed metal contact pads of the fabricated 1024ch device from the "device bonding side" of the PCB (Figure 1.13a) using a conductive epoxy (Silver Conductive Epoxy Adhesive, MG Chemicals) at an elevated temperature of 60 °C for over an hour. The device with the connector PCB was then mated on the "socket contact side (Figure 1.13b)" with the LGA socket on our custom amplifier board. The custom amplifier board consists of 16 amplifier chips (RHD2164, Intan Technologies), each addressing 64 channels, and the mating connector PCB for the device is secured in place with the socket clamp (Figure 1.13c).
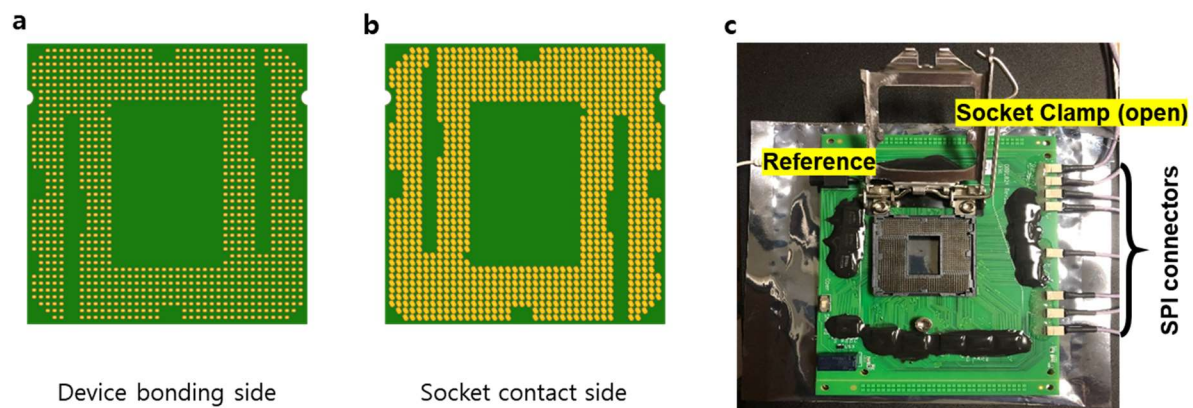
**Figure 1.13** Custom designed LGA socket connector PCB and custom amplifier board. (a) The device bonding side of the custom LGA socket connector PCB. (b) The socket contact side of the custom LGA socket connector PCB. (c) Custom amplifier board embedding 16 RHD2164 chips.

### 1.2.2    Electrochemical and Structural/Morphological Characterization and Analysis

As discussed earlier, the electrode impedance was controlled by modifying the electrode surface materials. Here, we compared the feasibility of the processes involving a conductive polymer, poly(3,4-ethylenedioxythiophene) (PEDOT:PSS), and platinum nanomesh, or PtNM.

Figure 1.14a shows an array after attempting to electrodeposit PEDOT:PSS on all microneedles of a 32ch array with total of 31 microneedles. The contrast in the color of the tip of the microneedles varied despite consistent parameters used for electrodeposition. Figure 1.14b, and 1.13c shows the tip of a microneedle after galvanostatic (constant current), and potentiostatic (constant voltage) deposition of PEDOT:PSS, respectively. The potentiostatic electrodeposition of PEDOT:PSS seemed more susceptible to over-deposition of PEDOT:PSS as shown in Figure 1.14c, and the galvanostatic electrodeposition seemed to be slightly more reproducible but nonetheless it had poor reproducibility in the morphology of the electrodeposited PEDOT:PSS. Although the parameters from previously reported work[33] were used for both galvanostatic and potentiostatic electrodeposition settings for each microneedle array, we observed that not only the deposition

thickness and texture was inconsistent but also the resulting electrochemical impedance at 1 kHz of the entire Si microneedle array showed poor yield as demonstrated in the histogram in Figure 1.14d. It is likely that this was caused by small variations in serial resistance, ohmic contact quality, and the contact surface area of individual microneedles. In addition, the electrodeposition of PEDOT:PSS must be performed on one microneedle at a time, making it a non-scalable process.

Hence, we moved on to a more reliable, reproducible, and monolithic approach of defining PtNR or PtNM at the tip of the microneedle. The survivability of the Pt nanorods of a few hundreds of nanometers during the penetration into cortical tissue was questionable, thus we modified the co-sputtering recipe of the Pt-Ag alloy to form PtNM structure. The power for Pt deposition was increased to 100 W instead of the original 50 W used in co-sputtering process for PtNR, while the Ag deposition power was set the same at 400 W. PtNM is in principle, similar to PtNR, but forms larger islands of Pt, maintaining the porous nature of the morphology which increases the active surface area, thus reducing the electrochemical impedance. Figure 1.15a shows planar, bare Si surface at the tip of a test microneedle after 2-step DRIE as reference. Figure 1.15b shows another test sample that was coated PtNM, confirming the porous morphology that increase the active surface area of the electrode when compared to Figure 1.15a. Figure 1.15c shows an image of a test wafer with a 7 by 7 array of PtNM dots on Si surface. Unlike the electrodeposition of PEDOT:PSS, the PtNM morphology was consistent throughout the wafer. The reproducibility of this material was confirmed with the histogram in Figure 1.15d. The impedance distribution of 9 devices showed that the center of distribution is at much lower impedance, below 1 MΩ.
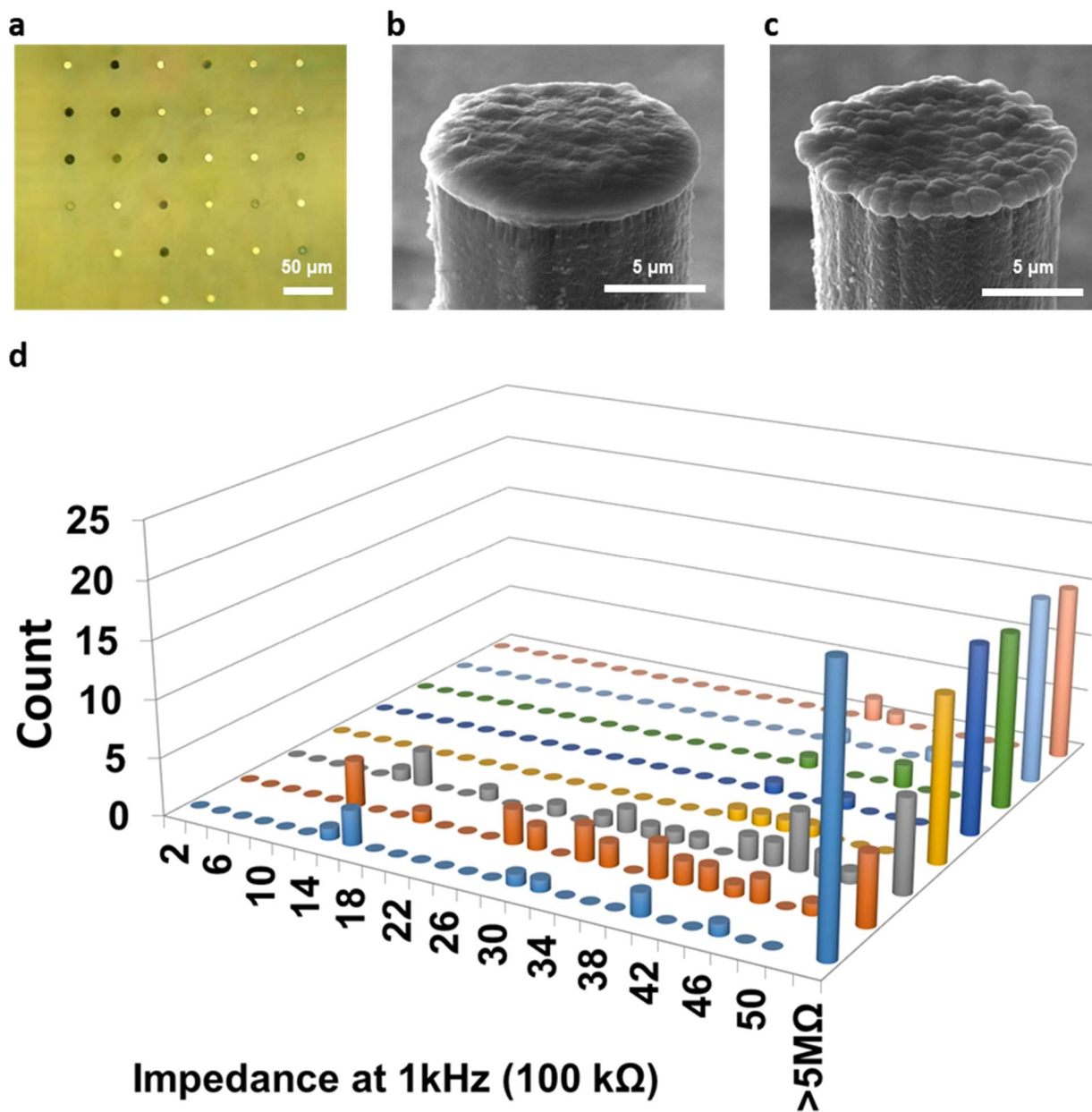
**Figure 1.14** Electrochemical and Structural/morphological characterization of PEDOT:PSS on 32ch SiMNA on flex. (a) A magnified image of an array of electrodeposited PEDOT:PSS at the tip of the microneedles. (b) A microneedle tip after galvanostatic deposition of PEDOT:PSS. (c) A microneedle tip after potentiostatic deposition of PEDOT:PSS. (d) A histogram of impedance at 1kHz for 8 different devices with electrodeposited PEDOT:PSS.
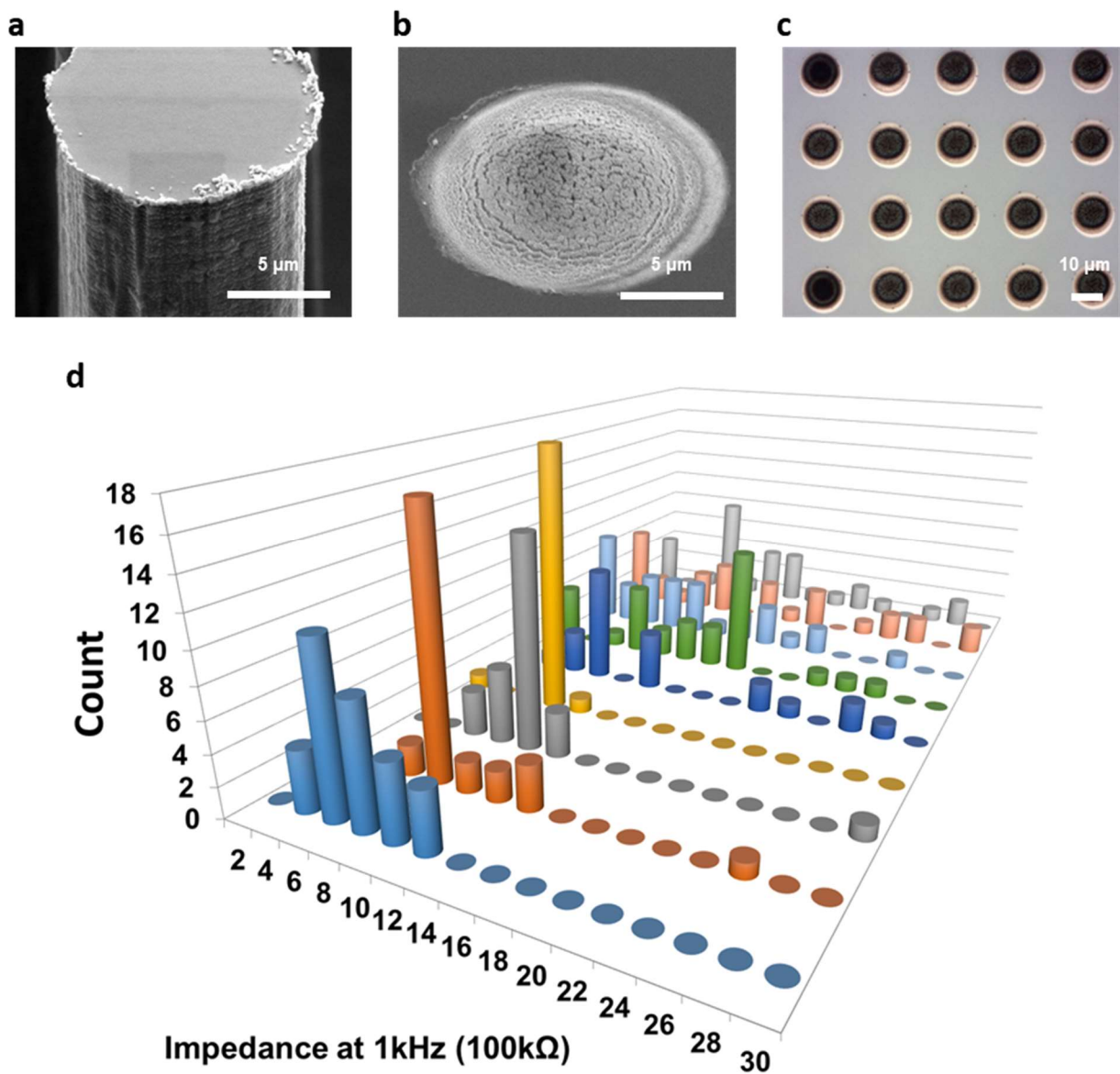
**Figure 1.15** Electrochemical and Structural/morphological characterization of PtNM on 32ch SiMNA on flex. (a) A microneedle tip after with bare Si surface after 2-step DRIE. (b) SEM image of PtNM on test wafer. (c) A magnified image of an array of PtNM dots after wet etching Ag from the original PtAg alloy. (d) A histogram of impedance at 1kHz for 9 different devices with PtNM.

After settling with PtNM as the electrode surface material for the SiMNA on flex, further electrochemical characterization was performed. The impedance magnitude and phase spectra were measured in Dulbecco's phosphate-buffered saline (DPBS, Thermo Fisher Scientific) which are shown in Figure 1.16a and 1.16b, respectively, and contrast those before (red curve, Si tip) and

after (blue curve, PtNM tip) coating the SiMN tips with PtNM. At 1 kHz, the average impedance of a SiMN with the PtNM tip was 643 kΩ ±208 kΩ, which is nearly an order of magnitude lower than the average impedance of 5.03 MΩ ±3.41 MΩ for the bare SiMN (Figure 1.16a). The average phase angle at 1 kHz was -66.0 ° ±13.2 ° for PtNM and -60.4 ° ±13.4 ° for Si surface (Figure 1.16b). Further analysis with the voltage transient (Figure 1.16c, injected current 2 μA, pulse width 400 μs), we measured that a single microneedle with PtNM coating would be capable of delivering up to maximal cathodal current, or $I_{mc}$ of 1.78 μA at maximal cathodal potential, or $E_{mc}$ (Figure 1.16d). The Utah electrode arrays demonstrated that the average threshold of electrical stimulation required to induce stimulation evoked response in cat model was around 8.9 nC/ph.[34] Our measured $I_{mc}$ of 1.78 μA in the same voltage transient as the Utah array (biphasic, injected current 100 μA, pulse width 100 μs per phase), predicts that our device can deliver charge of up to 0.178 nC/ph, about 50 times less that the Utah array. We believe that this is partially due to the fact that the tip surface area of our device is much smaller for our SiMNA on flex, although the novel PtNM structure allows one to increase the charge injection capability of an electrode that once had planar surface. This leaves us with a room for future improvements such as replacing the two ohmic contacts; one at the tip and the other at the bottom of the microneedle, with flush metalltization from the PtNM electrode surface to the recording system, while still passivating the sidewall of the microneedle. Such approach is expected to futher reduce the impedance by bypassing the silicon material of the microneedle in between the PtNM electrode and the metal lead at the base.

The 1 kHz *in-vivo* impedance was monitored for three independent implantations (mouse #2, 4, and 6) for up to 137 days and was generally higher than the results from the benchtop tests, as expected (Figure 1.16e). The overall 1 kHz average impedance fluctuated below the 1.5 MΩ-bar[35] which was suitable for high signal-to-noise ratio (SNR) recordings.
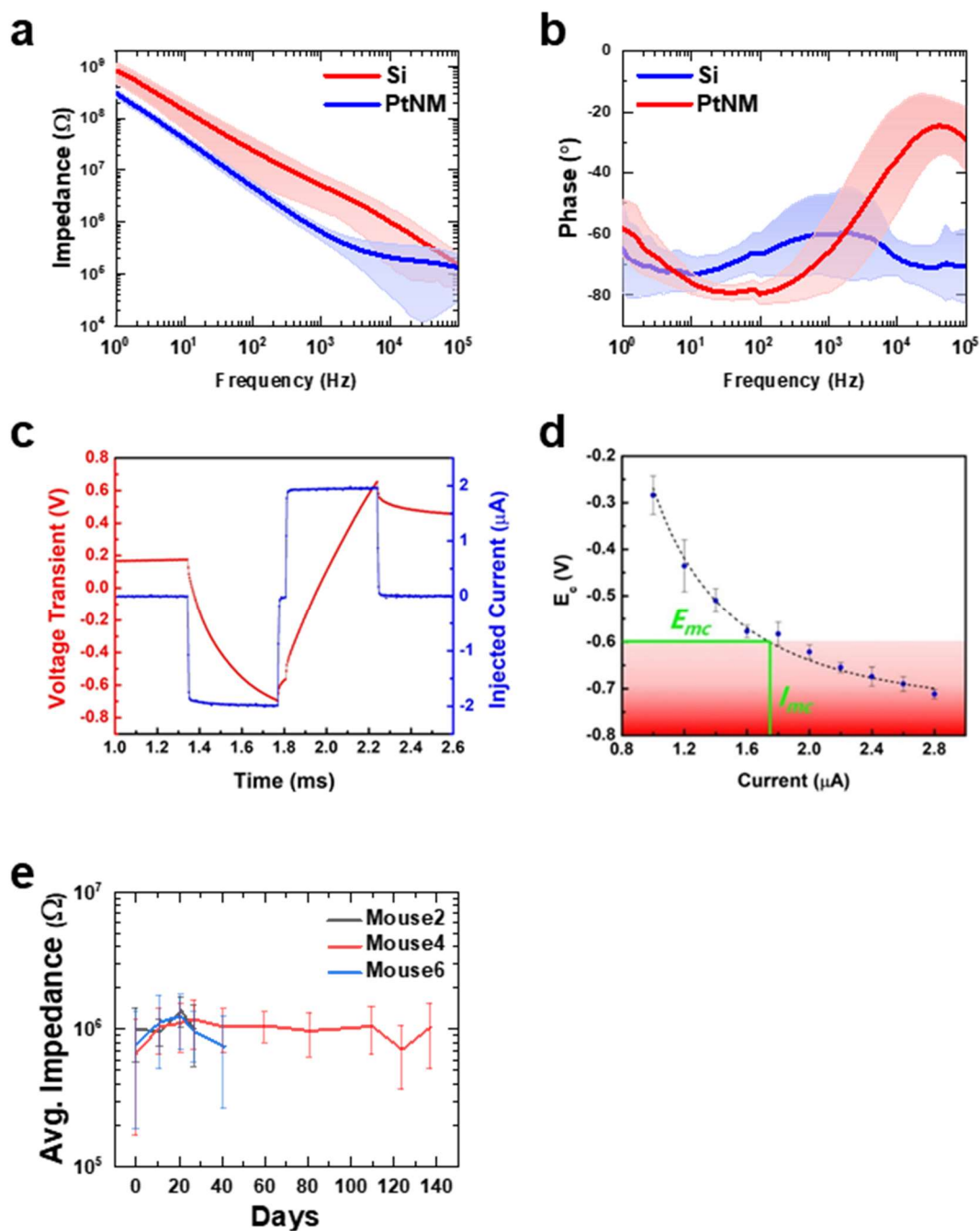
**Figure 1.16** Benchtop electrochemical characterization of 32ch SiMNA on flex with PtNM electrode surface. (a) Impedance plotted against frequency for a SiMN before (red) and after (blue) coating with PtNM. (b) Phase angle plotted against frequency for a SiMN before (red) and after (blue) coating with PtNM. (c) Measured voltage transient of a single 10 μm diameter SiMN with PtNM coating. (d) Determination of the cathodal current injection limit ($I_{mc}$), charge injection limit (CIC).

### 1.2.3 Chronic Implantation of the 32ch Si MNA on Flex Devices in Mice

For the insertion of Utah electrode arrays in to the cortical tissue, a pneumatic implanter system is typically used.[36] The aggressive, pneumatic punching motion allows full penetration of the Utah electrodes, but this alone induces undesired situations like bleeding and other clinical complications,[37] not to mention the invasiveness of the Utah array itself.

In order to devise am implanter setup suitable for our platform, we combined the micromanipulator secured on the stereotaxic frame with the typical pneumatic implanter rod (Pneumatically-Actuated Impulse Array Inserter, Blackrock Microsystems) where we added micropipette tip connected to a vacuum hose (Figure 1.17a). After the custom connector PCB and the 3D-printed headpost are secured to the titanium headpost, the vacuum-enabled tip grabs the backside of the array with the Si microneedles facing downwards and the micromanipulator is used to aim the array on the desired implantation site on either the test agarose bed or the rodent somatosensory cortex (Figure. 1.17b and 1.17f). A few drops of artificial cerebrospinal fluid (aCSF) were applied on the target region and then the device was gently lowered down to additional 300-500 μm from the surface of either the test agarose bed, or the rodent somatosensory cortex (Figure 1.17c and 1.17g). During the test on agarose bed, we also applied the 1 mm-deep, 22psi pneumatic punch motion. This allowed full penetration of our most dense array of 50 μm microneedle-to-microneedle spacing as demonstrated in the cross-sectional two-phone image in Figure 1.17e, but when applied to the rodent model, we observed multiple issues such as bleeding and the rodent model dying from seizure.

Hence, we diverted our approach by only applying the "gentle-push" method on the chronic rodent models, while increasing the microneedle pitch size to 400 μm to allow easier full penetration of all microneedles into the cortical tissue without the need for the pneumatic implanter setup. Figure 1.18a shows an example of chronic implantation of the device after 22 days *in vivo*.
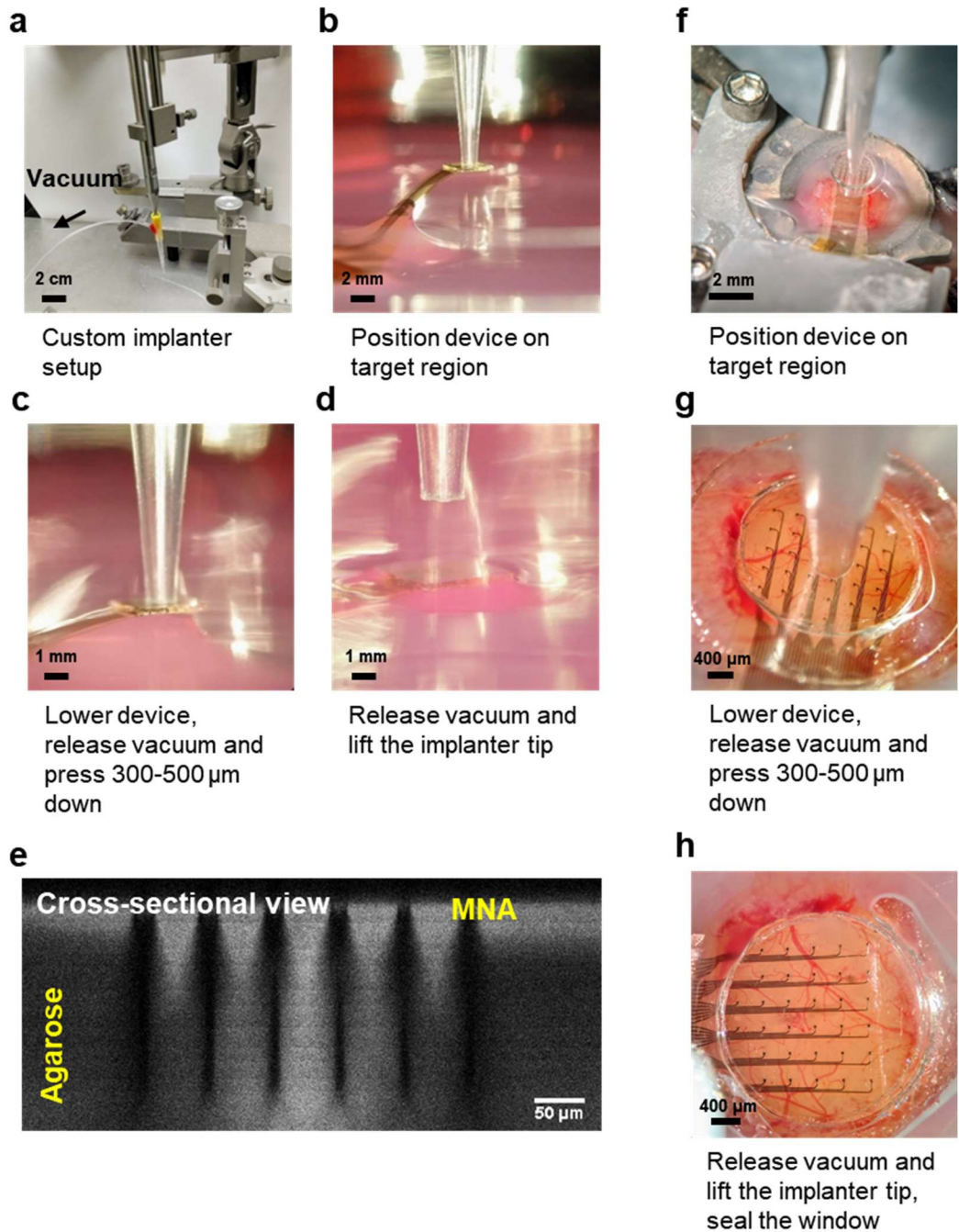
**Figure 1.17** Custom implanter and optimization of implantation procedure. (a) Custom implanter setup. (b) Vacuum-enabled tip holding the array for aiming of the implant site on agarose bed. (c) Wet the target region with aCSF, lower the array and press down additional 300-500 μm from the surface. (d) Release the vacuum and lift the implanter tip. (e) A cross-sectional two-photon image of the test array fully penetrating into the agarose bed. (f) Vacuum-enabled tip holding the array for aiming of the implant site on rodent somatosensory cortex. (g) Wet the target region with aCSF, lower the array and press down additional 300-500 μm from the surface. (h) Release the vacuum, lift the implanter tip, and seal the cranial window with UV-curable dental cement.

There was no indication of bleeding on the barrel cortex of the mouse from the visual inspection. The cross-sectional two-photon images taken from the cutlines highlighted with red and blue arrows showed ChR2-EYP-expressing brain tissue in between black shadows of the Si microneedles (Figure 1.18b).
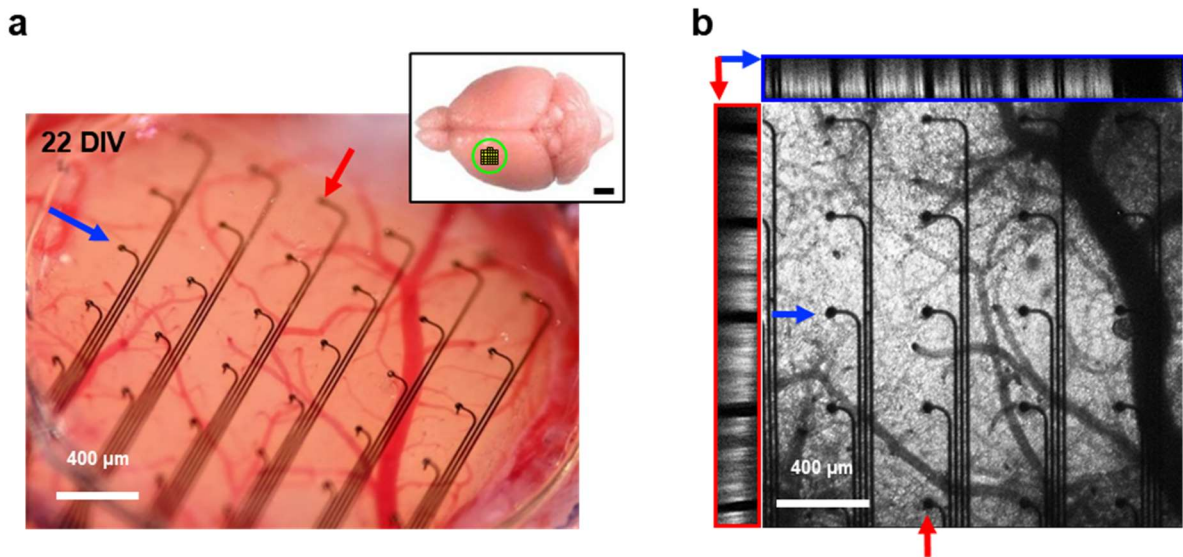


**Figure 1.18** Chronic implantation of 32ch SiMNA on flex and two-photon imaging. (a) A magnified image through the cranial window of a 32ch SiMNA implanted on mouse barrel cortex (22 days *in vivo*). Inset shows the approximate size of the craniotomy at the implantation site (scale bar, 2mm). (b) Two-photon image stack of the array from (a). The left (red box) and the top (blue box) insets show the cross-sectional images taken from the vertical (red arrow, medial-lateral) and horizontal (blue arrow, posterior-anterior) cutlines where the SiMNs exhibit black contrast demonstrating full implantation in tissue.

### 1.2.4    Animal Procedures

All experimental procedures were performed in accordance with the guidelines established by the UCSD Institutional Animal Care and Use Committee (IACUC). We used 6 adult (age > 8 weeks) Emx1-Cre;Ai32 double transgenic (het/het) mice of either sex with[38] (JAX 005628 and 024109) on C57BL/6 background. Surgical procedures were performed as previously described[39] with some modifications. Briefly, a 3-mm cranial window was implanted over the left barrel cortex (coordinates A-P 2 mm and L-R 3 mm relative to bregma). As reference electrode, a micro-screw

was inserted above the cerebellum of the right hemisphere. For head fixation of the animals during recording procedures, we attached a custom-designed headpost machined from titanium. The headpost allows fixation of a custom connector PCB within a lightweight 3D-printed protective enclosure.

After surgery, animals were allowed to recover for 7-14 days before animals are habituated for head fixation.[40] Animals were anesthetized with Isoflurane, the headpost was fixed to the stage, and the recording equipment was connected. Then, anesthesia was discontinued, and animals woke up while under head-restrain. Recording sessions were started that lasted for 30-60 min.

At the end of the study, animals were deeply anesthetized with 210 mg/kg pentobarbital (Fata Plus) and transcardial perfusion of 10 mL heparinized DPBS followed by 15 mL DPBS with 4% paraformaldehyde (PFA, prepared from 16% PFA stocks, Electron Microscopy Sciences) was performed. After perfusion, brains were extracted and placed in DPBS with 4% PFA overnight at 4 °C. Then, brains were transferred into water containing 20% sucrose until further processing. The location of the craniotomy was highlighted by inserting a glass microneedle covered in carbon beads at four corners around the implantation site.

For immunofluorescence, the brain was fixed a second time in 10% neutral buffered formalin and dehydrated in 70% EtOH over several days. It was paraffin processed (Reveal BioSciences, San Diego), embedded, and sectioned at 10 μm on a microtome. Sections were dehydrated and antigen retrieval performed using a Retriever 2100 (Electron Microscopy Sciences) in citrate buffer. Sections were washed and blocked in 0.5% goat serum for one hour. The sections were then incubated in primary antibodies in PBS-T (chicken anti-Neun, 1:500, Sigma-Aldrich ABN91; Cy3-conjugated anti-GFAP, 1:1000, Sigma-Aldrich C9205; Rabbit anti Iba1, 1:1000,

Sigma-Aldrich ZRB1177) overnight. Sections were washed and then incubated with secondary antibodies for 30 minutes (goat anti-chicken 488, 1:100, Sigma-Aldrich SAB4600039; goat anti-rabbit 647, 1:100, Sigma-Aldrich SAB2600184). After final washes, sections were coverslipped with ProLong Gold with DAPI (Thermo-Fisher). Images were acquired at the UCSD Nikon Imaging Core using a Nikon Eclipse Ti2-E equipped with a DS-Qi2 CMOS camera.

### 1.2.5   Two-Photon Imaging

Procedures were similar to those described previously.[40] Fluorescein isothiocyanate (FITC)-labeled dextran (MW = 2 MDa, FD-2000S, Sigma), or Alexa Fluor 680 conjugated to amino-dextran (MW = 2 MDa, Finabio AD2000x100) in-house, was injected IV (50-100 ul of 5 % (w/v) solution in phosphate-buffered saline) to visualize the vasculature. Images were obtained using an Ultima two-photon laser scanning microscopy system from Bruker Fluorescence Microscopy equipped with an Ultra II femtosecond Ti:Sapphire laser (Coherent) tuned between 800-1000 nm. FITC and Alexa Fluor 680 were imaged using cooled GaAsP detectors (Hamamatsu, H7422P-40). We used a 4x objective (Olympus XLFluor4x/340, NA=0.28) to obtain low-resolution images of the exposure. An 0.5-NA 20x objective water-immersion objective (Olympus UMPlanFI) was used for high-resolution imaging.

### 1.2.6   Optogenetic Photostimulation

Optogenetic stimulation was performed with a 450-nm diode-pumped solid-state laser (Optoengine) either coupled to a 200-um, 0.22 NA optical fiber (Thorlabs FG200UEA) or into the Ultima two-photon laser scanning microscopy. Pulses were controlled through Prairie View Software; a trigger signal in synchronization with the laser pulse was sent to the Intan recording system for synchronization.

### 1.2.7   Sensory Stimulation

For sensory stimulation, each trial consisted of a single air puffs delivered to the lower bottom part of the contralateral whisker pad to avoid eye blink reflexes. In case of 1024ch device on anesthetized rat model, contralateral hindlimb was also stimulated with the same air puff for comparison with the stimulation on whiskers. Air puffs were delivered through a pneumatic microinjector (Pneumatic PicoPump, World Precision Instruments) controlled through a data acquisition system with custom-written MATLAB routines; a trigger signal in synchronization with the air puff was sent to the Intan recording system for synchronization.

### 1.2.8    Recording and Analysis of Electrophysiological Data

The electrophysiological data were recorded as previously described[35] using a RHD2000 amplifier board and RHD2000 evaluation system (Intan Technologies). The sampling rate was 20 kHz. Data were analyzed in MATLAB using custom-written software. After import and conversion into MATLAB files, bandpass filter was applied at 1 Hz to 250 Hz for local field potential activity, bandpass filter was applied at 250 Hz to 3000 Hz for activity in the higher frequency band such as MUA and single units, trigger signals were detected and further evaluation steps were performed.

The motion of the awake mouse was recorded using an infrared CCD camera at frame rate of 20 Hz or 40 Hz, which was time aligned to electrophysiological data using the trigger signals synchronized with the RHD2000 evaluation system. The video data was collected as individual frames using a custom MATLAB code which then calculated the standard deviation of the brightness and contrast in the images of the contralateral whisker pad region.

For single unit detection, the electrophysiological data that had lower than 5% of the motion data was selected to prevent motion artifact affecting the spike sorting process. The selected data was exported to Offline Sorter (Plexon). Spikes were detected by setting the

waveform length of 1500 μs, prethreshold period of 350 μs, dead time of 1050 μs, and then the threshold was set to -3 times standard deviations from mean of peak heights histogram,[41] automatic sorting using valley seeking scan mode.

## 1.3 Results and Discussion

### 1.3.1 Two-Photon Imaging and *In Vivo* Electrophysiological Recordings of Optogenetic Photostimulation-evoked Responses in Anesthetized Mice.

With optical access afforded by the flexible substrate backing of the penetrating SiMNAs, we are able to perform two-photon imaging through the array as illustrated in Figure 1.19. Figure 1.19a shows the overview after 28 days *in vivo* of the array implanted on the barrel cortex with clear visibility of the vascular structure underneath the SiMNA on flex. Figure 1.19b is a magnified view of one of the microneedles that is penetrating into the cortical tissue without causing bleeding, in other words, puncturing the blood vessel, as indicated by the pressure point on the vessel where the sidewall of the microneedle is pushing the vessel wall inwards.
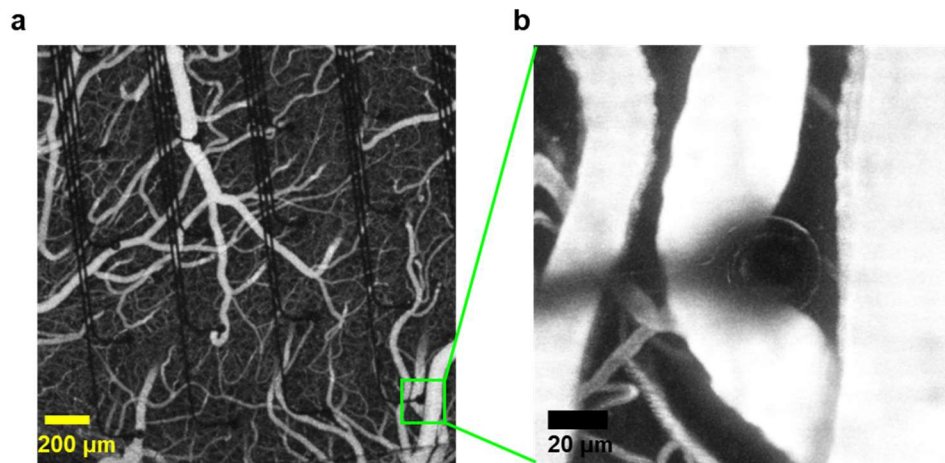


**Figure 1.19** Two-photon imaging of the barrel cortex implanted with SiMNA on flex. (a) Vascular structure beneath the SiMNA on flex, after 28 days *in vivo*. (b) A magnified view of a microneedle penetrating into the cortex without puncturing the blood vessel.
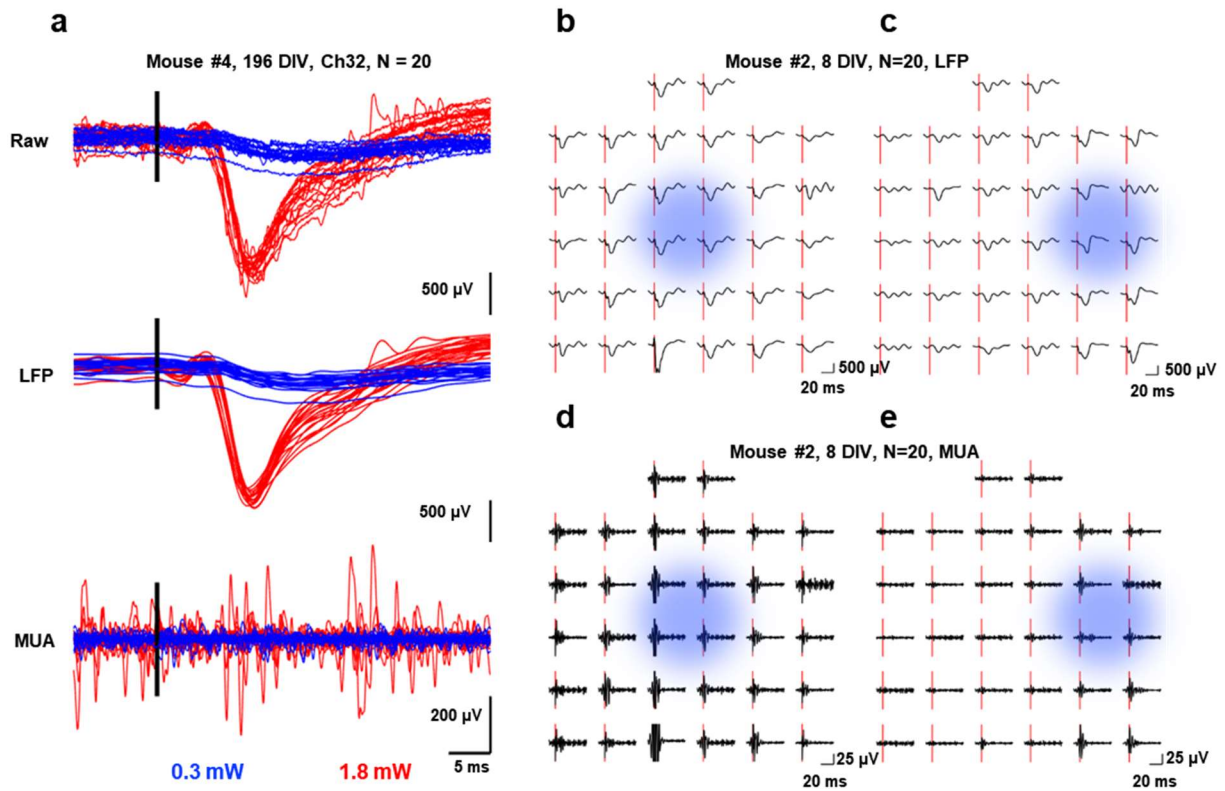
**Figure 1.20** Optogenetic stimulation-evoked responses in anesthetized mice. (a) Stacks of optogenetic photostimulation-evoked electrical potentials from all individual trials (N=20) from a single channel (Ch32) 400 μm-spacing 32ch MNA on flex after 196 days *in vivo* (DIV). Raw and filtered (LFP; 1-250 Hz, MUA; 250-3000 Hz) data for lower (blue, 0.3 mW) and higher (red, 1.8 mW) amplitudes of optogenetic photostimulation (black bar). (b)-(e), Average mapping of optogenetic photostimulation (red bar) evoked responses from 400 μm-spacing 32ch MNA on flex after 8 DIV (average of 20 trials, blue circle indicates approximate area of the photostimulation beam; (b) and (d) focused in the center of the array, (c) and (e) focused on the posterior side of the array with respect to the mouse, (b) and (c) LFP; 1-250 Hz, and (d) and (e), MUA; 250-3000 Hz).

To evaluate the capabilities of the SiMNAs in recording local field potentials, we illuminated the cortical region in between the 32ch SiMNA with two different laser excitation powers of 0.3 mW and 1.8 mW for 5 ms. The 1.8 mW laser excitation power elicited well resolved local field potentials (LFP, < 250 Hz) and multi-unit activity (MUA, 250 Hz to 3000 Hz) as shown in Figure 1.20a, where spontaneous MUA firing was also prevalent. The 0.3 mW laser excitation power did not evoke activity in the same recording session on the same animal. By focusing the

laser beam on two different locations relative to the 32ch SiMNA (indicated by light blue circles in Figure 1.20b-e), the location of the maximal responsive channels shifted accordingly for both LFP (Figure 1.20b and 1.20c) and MUA (Figure 1.20d and 1.20e).

### 1.3.2. Electrophysiological recording of sensory evoked responses and the detection of single units in awake mice.

We performed electrophysiological recordings of sensory stimulation-evoked responses in head-fixed awake mice. The whiskers on the right side of the mouse, contralateral to the implanted left hemisphere, was stimulated by deflection with an air puff (26 psi, 5 ms pulse per trial) (Figure 1.21). The yellow dotted lines indicate the initial position of the whiskers, 25 ms before the stimulation trial. The white line shows the whisker at the onset of air puff, just starting to traveling backwards. Then around 25 ms post-stimulus, the whisker reaches its maximal posterior position, highlighted in red dotted line, due to air puff, aligning well with the first phase of the response marked with red arrow in Figure 1.22b. At around 75 ms post-stimulus, not only the puffed whisker travels back towards anterior side, as highlighted in green dotted lines, but also the ipsilateral whiskers that were not deflected also starts moving forward, indicating the initiation of whisking activity which aligns well with the peak marked with green arrow in Figure 1.22b.

Figure 1.22a shows a stack of the average filtered LFP and MUA responses from all SiMNs where the 22 to 28 ms post-stimulus response is highlighted with light-blue box. Figure 1.22b provides magnified view of this average filtered data for a single, representative channel, in which the rectified MUA reveals the two key stages in the sensory stimulation-evoked response as discussed earlier in Figure 1.21. The first response, highlighted with a red arrow, represents the native cortical response to the air puff at 23 ms post-stimulus, similar to previously reported response times on various rodent models.[42] The second response, highlighted with a green arrow,

represents the mouse whisking in reaction to the air puff in conjunction with previously reported reflexive whisking evoked from sensory stimulation[43], starting around 70 ms post-stimulus as filmed in the video recording of the mouse motion and corresponds to the negative peak in the LFP response (Figure 1.22a). The colormap sequence in Figure 1.22c is taken from the blue highlighted region from Figure 1.22a, or the first response phase. The time-aligned MUA and LFP in Figure 1.22c showed clear selective activation and correlation. The MUA response recorded with higher sensitivity on the left part of the array is initiated at the top left and moves to toward the lower channels as time progresses. This LFP response that is initiated at the top-left corner of the SiMNA propagates towards the bottom-right side of the array. These broadband high spatiotemporal resolution recordings demonstrate the capabilities of our SiMNA for fundamental and applied neurophysiological investigations.
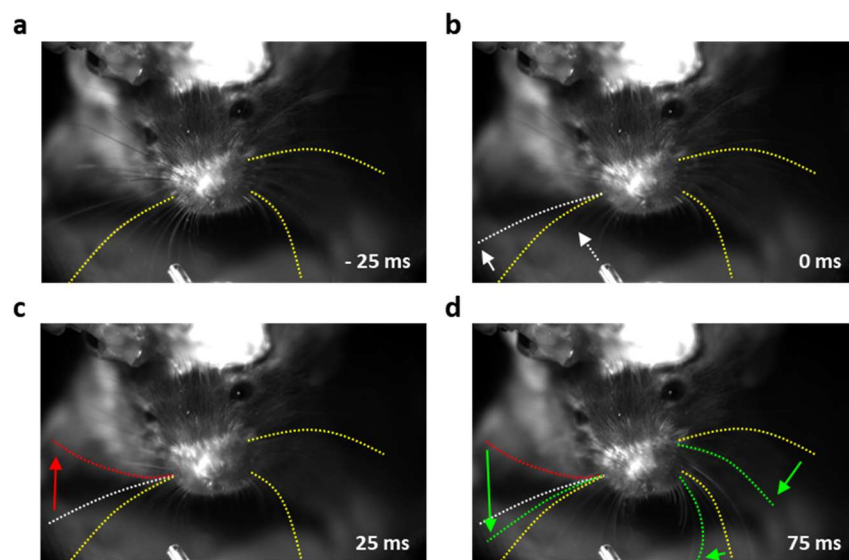


**Figure 1.21** Video recording image of the mouse for motion detection. (a) The awake mouse at 25 ms before air puff stimulation, in which the reference position of the whiskers are highlighted with yellow dotted lines. (b) The initiation of air puff stimulation at 0 ms, directed towards right side whiskers. Air puff stimulation (white dotted arrow), early-stage location of the whisker pushed back by air puff (white dotted line). (c) At 25 ms post-stimulus, the position of the whisker pushed further back by air puff (red dotted line). (d) Green dotted lines indicate the initiation of whisking activity on both sides in response to the air puff stimulation.
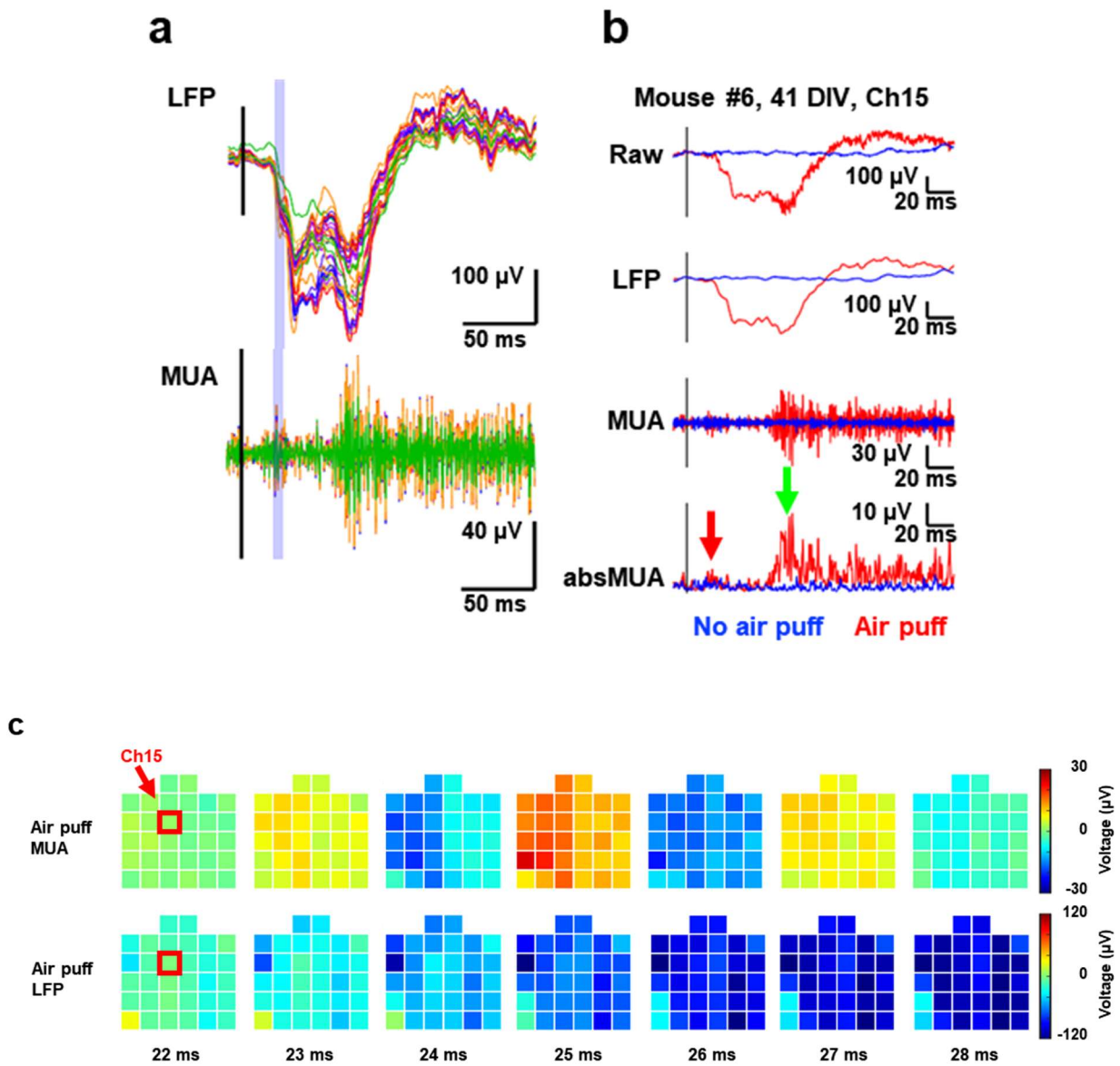
**Figure 1.22** Sensory stimulation-evoked responses in awake mice. (a) Average filtered whisker air puff stimulation-evoked responses from all channels of the 400 μm-spacing 32ch MNA on flex implanted on mouse somatosensory cortex. (b) Average filtered whisker air puff stimulation-evoked responses from a single channel (Ch15) of the 400 μm-spacing 32ch MNA on flex implanted on mouse somatosensory cortex. (average of 20 trials) (c) Heatmaps of filtered whisker air puff stimulation-evoked MUA and LFP responses 22 ms to 28 ms post-stimulus, corresponding to blue highlighted region in (a). Ch15 from (b) is highlighted red box at 22 ms post-stimulus. (a)-(c) LFP: 1-250 Hz, MUA: 250-3000 Hz, absMUA: rectified MUA.

The SiMNAs are also capable of recording single unit activity. To avoid the influence of motion artifacts, we selected the electrical recording in which had less than 5% level of motion from the video recording data, thus yielding pre-processed recording of 23 s. Figure 1.23 illustrates example units detected from a single Si microneedle electrode. Other SiMN electrodes in the same array detected between 2 to 9 units per channel from the same recording. The inter-spike interval (ISI) histograms and corresponding clusters confirmed that the detected units were distinguishable units from each other and the ISI usually stayed below 60 ms during the 23 s recording data.
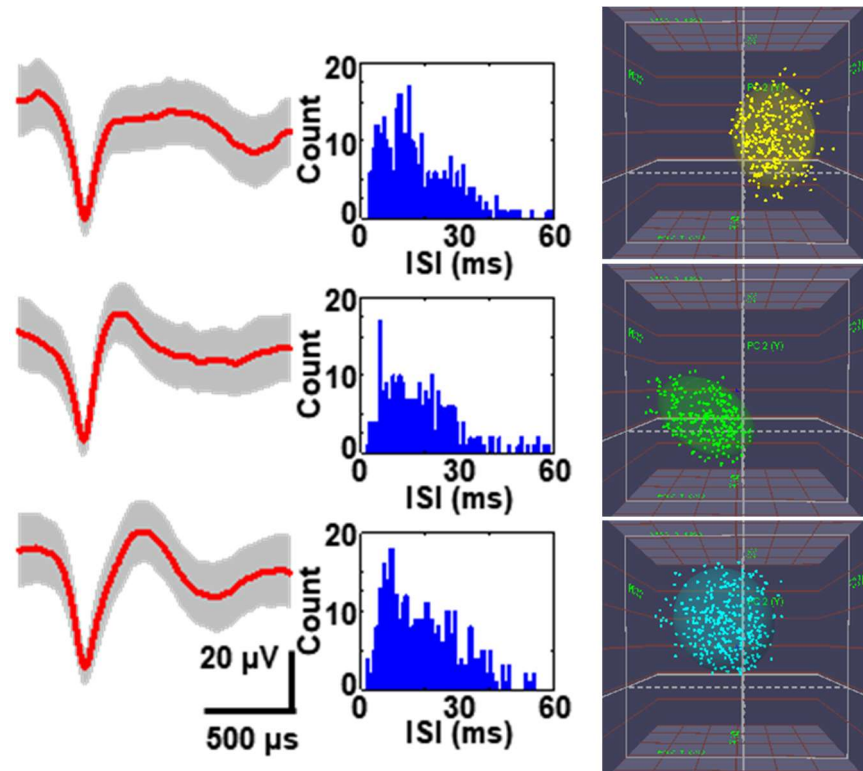


**Figure 1.23** Detection of single unit activity. (a) three distinguishable units detected from Ch05 SiMN, after 41 days *in vivo*. (b) ISI histograms corresponding to the units in (a). (c) Cluster analysis of the units detected in (a).

The recorded units from the SiMNA were independent from each other, as further confirmed by comparing the spike firing in raster plots of the single units detected in four neighboring channels (Figure 1.24 and 1.25). Channels 13, 05, 12, and 06 detected 6, 3, 4, and 4

single units, respectively. All detected units from these channels showed different waveforms; e.g. the waveform of a single unit in channel 13 marked with yellow arrow in Figure 1.25c was distinguishable from all other 16 units.
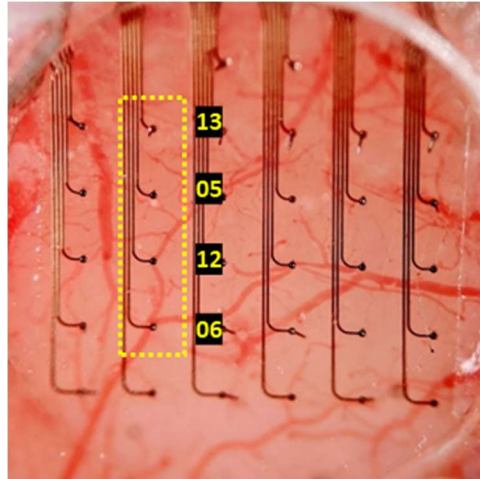


**Figure 1.24** A magnified photograph of a 32ch SiMNA on flex with 400 μm microneedle-to-microneedle spacing implanted in mouse #6 somatosensory cortex. Spike sorting was performed on Ch13, 5, 12, and 6 which are highlighted in yellow box.
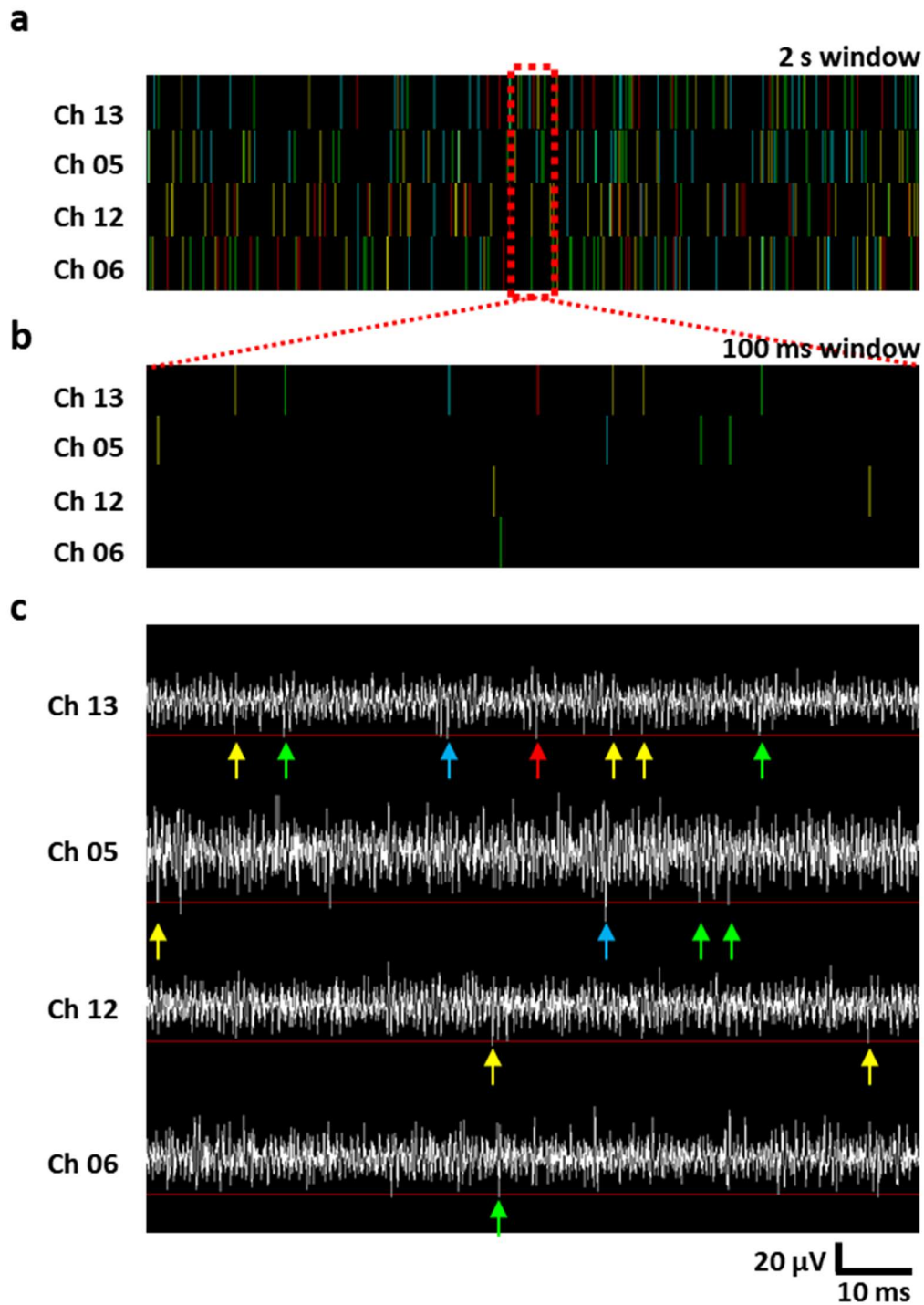
**Figure 1.25** Raster plots of detected single units from four neighboring SiMNs. (a) A spike raster of 2 second window from Ch13, 5, 12, and 6. (b) A magnified spike raster of 100 millisecond window from Ch13, 5, 12, and 6 in the red highlighted box from (a). (c), Filtered and spike detected waveforms from respective thresholds (red line), time-aligned with the spike raster in (b). Yellow, green, blue, and red arrows indicate time stamps of detected units. Mouse #6, 41 days *in vivo*.

### 1.3.3 Histology

Immunohistochemistry was performed for the analysis of the cortical tissue in response to the chronic implantation of the 32ch SiMNA. Figure 1.26a shows the hematoxylin and eosin (H&E) stained coronal section of the mouse cortical tissue where a single Si microneedle was implanted for a total of 73 days and then extracted for sectioning. The visual inspection of the neuronal distribution within the section seemed consistent both around and away from the Si microneedle. The immunofluorescent image from the ipsilateral hemisphere where the Si microneedle was inserted (Figure 1.26b) was compared with that from the contralateral hemisphere as reference (Figure 1.26c). The dark spot in the center of Figure 1.26b is where the SiMN penetrated through the cortical tissue (100 μm in depth), and the diameter of the puncture, about 10 μm, matches that of the SiMN. No differences in neurons (NeuN), astrocytes (GFAP), and microglia (IBA1) were observed relative to the reference image from Figure 1.26c. This confirms the minimally-invasive characteristics of the SiMNA on flex.
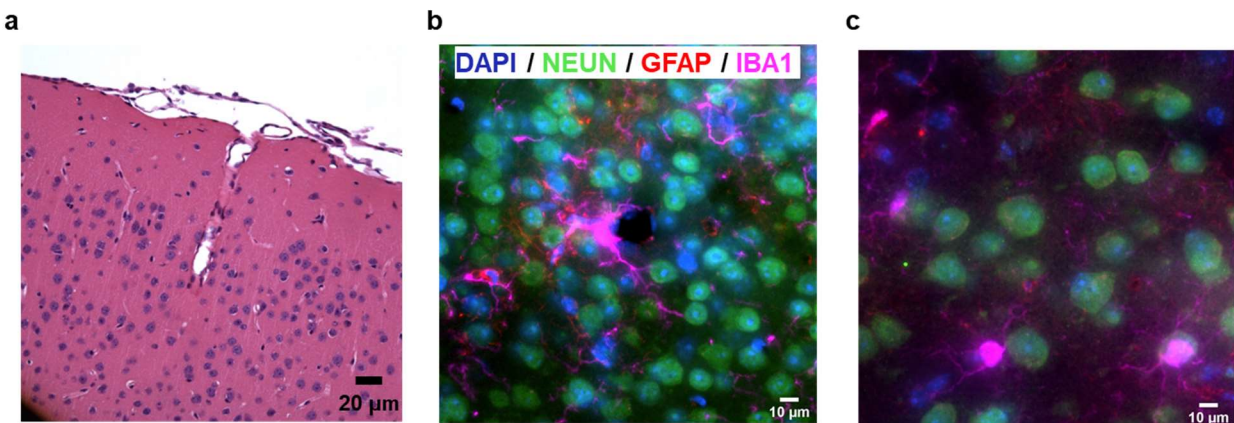


**Figure 1.26** Histology of chronic implantation site of the SiMNA. (a) H&E-stained coronal section of cortical tissue where a SiMN was implanted. (b) Immunofluorescent image of DAPI/NEUN/GFAP/IBA1-stained lateral section, 100 μm in depth, of the cortical tissue in the ipsilateral hemisphere where a SiMN was implanted. (c) Immunofluorescent image of DAPI/NEUN/GFAP/IBA1-stained lateral section, 100 μm in depth, of the cortical tissue in the contralateral hemisphere.

### 1.3.4 Large Scale Mapping of Whisker Air Puff Stimulation Evoked Brain Activity

In order to demonstrate higher cortical coverage recording of the 1024ch SiMNA on flex, we performed recording of sensory evoked brain activity of acute rat model similar to that of the 32ch SiMNA on flex. The recording setup is shown in Figure 1.27a with the device mounted on the custom amplifier board which is secured to the stereotaxic frame and sits above the anesthetized rat. The overall cortical coverage of the array was $12.8 \times 12.8$ mm$^2$, which was greater than the area of the rat craniotomy that did not cause surgical complications and larger than a single hemisphere of the anesthetized rat as shown in Figure 1.27b. The green highlighted region shows the region where the Si microneedles were fully inserted into the cortical tissue on the right hemisphere and the red highlighted region is where the Si microneedles were resting atop the exposed skull. Figure 1.27c shows the immediately after the implantation of the SiMNA. There is small bleeding spot in the top-right corner of the image, or the anterior lateral side of the exposed right hemisphere, which did not hinder our visual inspection afterwards.
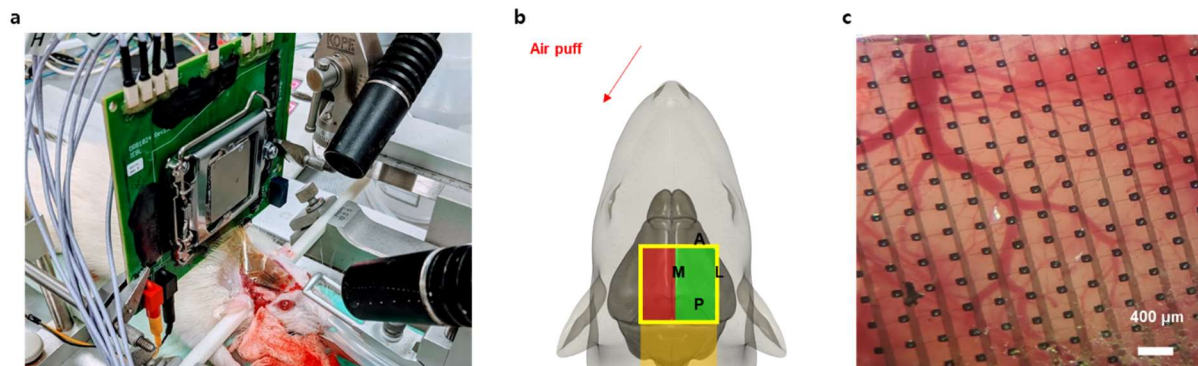


**Figure 1.27** Implantation of 1024ch SiMNA on flex. (a) Recording setup with device on custom amplifier board atop anesthetized rat. (b) Schematic diagram of the air puff stimulation direction and implantation site. (c) Implanted device on the right hemisphere of the rat.

The sensory stimulation was delivered on all contralateral (left side of the rat) whiskers by air puff stimulator (40 psi, 5ms duration). The colormaps of the air puff stimulation-evoked responses showed clear indication of broad LFP activation (Figure 1.28a), and more localized high gamma activation (Figure 1.28b). Figure 1.28c shows that the colormap of the high pass filtered

data (HPF) was substantially more localized despite large saturation from artifacts in the left side of the array (or the red highlighted region from Figure 1.27b). Figure 1.28d, 1.28e, and 1.28f show all filtered waveforms from medial(M)-lateral(L), and anterior(A)-posterior(P) cutlines from the colormaps in Figure 1.28a, 1.28b, and 1.28c, respectively. As the frequency range increases, it is clear that the average responses were much more localized, especially in the M-L cutline.
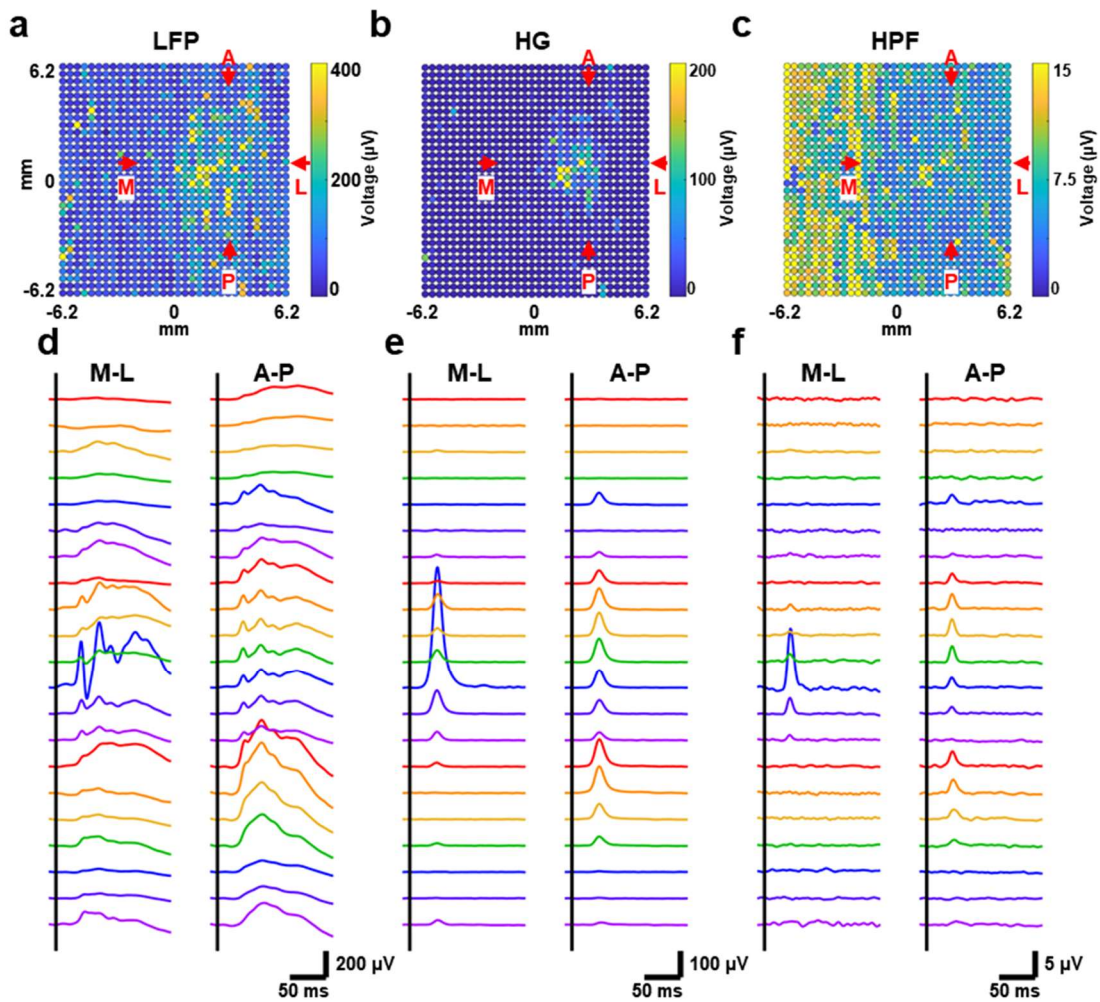


**Figure 1.28** Sensory stimulation-evoked responses in anesthetized rat recorded from 1024ch SiMNA on flex. (a)-(c) Colormaps of filtered average stimulation-evoked LFP, HG activity and HPF data, respectively. (d)-(f) Filtered waveforms from medial(M)-lateral(L), and anterior(A)-posterior(P) cutlines from corresponding colormaps in (a)-(c). (a)-(f) Average of 60 trials, LFP: 1-250 Hz, HG: 70-190 HZ, HPF: 250-3000 Hz.

In order to validate our recording, we compared the air puff stimulation-evoked responses from contralateral whiskers with that from the contralateral hindlimb. The average of 60 trials showed that the unfiltered waveform of the evoked responses was clearly visible in whisker stimulation in the range of 2 mm to 4 mm in x-coordinates, and -4 mm to 2 mm in y-coordinates (Figure 1.29a). As for the hindlimb stimulation, there was no noticeable waveform other than artifacts (Figure 1.29b).
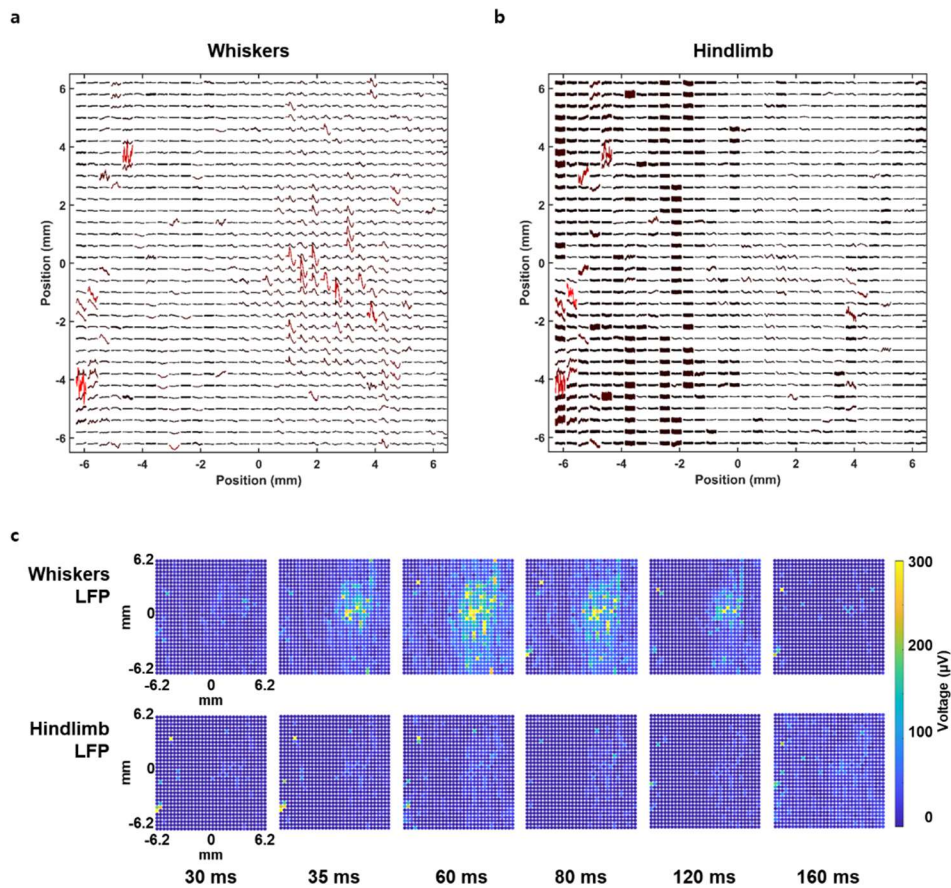


**Figure 1.29** Comparison of stimulation-evoked responses from whiskers and hindlimb stimulation. (a) Average mapping of unfiltered waveforms from whisker stimulation. (b) Average mapping of unfiltered waveforms from hindlimb stimulation. (c) LFP colormaps for air puff on contralateral whiskers and hindlimb from 30-160 ms post stimulus (a)-(c) Average of 60 trials, LFP: 1-250 Hz.

The LFP colormaps in Figure 1.29c further confirms the spatiotemporal characteristics of the stimulation-evoked LFP which initiates around 35 ms post-stimulus, similar to previously reported time stamp of 30 ms,[44] near the barrel cortex that is in the center of the successfully implanted Si microneedles and propagates outwards and diminishes between 120 ms and 160 ms post-stimulus. The recording with air puff stimulation on the anesthetized rat's hindlimb instead of the whiskers showed no detection of LFP, further confirming the validity of the whisker stimulation-evoked responses (Figure 1.29c).

## 1.4    Conclusion

In this work, we demonstrated a high spatial resolution, individually addressable Si microneedle array platform for chronic multimodal recording that consists of the recording of optogenetic photostimulation-evoked responses, sensory stimulation-evoked responses and *in vivo* two-photon imaging through the transparent, flexible substrate of the implanted device. We were able to detect broadband activities of local field potentials, high gamma activity, and multi-unit activity, along with the clear detection of single unit activity. The small diameter, high aspect ratio microneedle arrays constructed on biocompatible materials elicited minimal biofouling response. The newly developed fabrication methods allowed minimal rubbing against the brain micromotion for both acute and chronic implantations, low tethering from the connectorization, and high scalability of the process, expanding to 1024 channels which allowed high spatiotemporal recording of brain activity. To the best of our knowledge, our device is the highest channel count of Utah-like microelectrode array ever monolithically fabricated, especially on flexible substrate, and utilized in *in vivo* experiments. For future studies stemming from this platform, further improvements on the electrical stimulation capability delivered through the electrode surface

material of the Si microneedle, and more extensive large animal studies are required as the pre-step for clinical translation.

Chapter 1, in full, is currently being prepared for submission for publication of the material. S. H. Lee, M. Thunemann, F. Azzazy, D. R. Cleary, K. Tonsfeldt, K. Lee, H. Oh, Y. Tchoe, A. Devor, S. A. Dayeh. The dissertation author is the primary investigator and author of this paper.

# Chapter 2

## Platinum Nanorod Surface Electrode Arrays for Systematic Investigation of Effective Intradural Spinal Cord Stimulation

### 2.1    Introduction

In contrast to traditional extradural spinal cord stimulation (SCS), intradural SCS has the potential ability to provide higher stimulation efficacy, lower stimulation thresholds and lower charge injection densities for initiation, decreased power requirements, as well as concomitant recording and "smarter" stimulus-evoked stimulation for a variety of pathologies. But SCS poses new challenges in biomedical engineering, that can only be overcome with new materials and minimally invasive device designs.

The eventual target population for this work is spinal cord injury (SCI). Intradural SCS is a promising technology for SCI [45], and as SCS electrodes have decreased in size and materials have changed, it is critical for the advancement and adoption of this novel therapy to evaluate stimulation-induced neural tissue damage in the spinal cord. It is widely known that spinal cord tissue can be terribly unforgiving after injury, with a variety of detrimental biological processes taking place [46]. However, little is known about the limits of therapeutic stimulation of spinal cord tissue. Most tissue damage studies over the past few decades have focused on stimulation of the feline cerebral cortex [47] and have discovered a subtle difference in the behavior of electrical stimulation waveforms and protocols in macroelectrodes (area larger than ~$2000\mu m^2$) versus smaller, next-generation microelectrodes. Specifically, microelectrodes have generated tissue damage with increasing charge injection but are able to tolerate higher charge density (i.e charge normalized to the area of the electrode), much higher than that observed with macroelectrodes.

This distinction is thought to be due to non-uniform current distribution during a pulse in larger electrodes, which results in higher current and charge densities at the perimeter of the electrode. Our group have shown in electrochemical bench-top testing that the area of the electrode near the perimeter is only active in charge injection and degrades the charge injection capacity of the electrodes as the diameter increases. [48]

To understand the relationship between charge density and charge per phase on spinal cord nervous tissue, we built a series of novel thin and flexible next-generation spinal cord neural-electronic interfaces, with various electrode sizes and configurations, that were implanted in various animal models. Our first goal was to determine the safe charge injection thresholds for both macro and micro-electrodes, which has a high-impact from a clinical perspective, whereby the smallest possible currents to obtain initiation for each electrode diameter were determined. Our second goal was to demonstrate that our electrodes, made of contacts composed of Platinum nanorods with low electrochemical impedances, enabled high spatiotemporal resolution in recording, as well as localized and safe spinal cord microstimulation at low power. The results from this study did not only measure safe SCS thresholds, but also anticipated to create a full-feedback clinically therapeutic recording/stimulating system for adjunctive or primary therapy for SCI.

## 2.2    Experimental Details

## 2.2.1    Device Fabrication Process of Variable Diameter PtNR Devices for Acute and Chronic Rodent and Pig Models

In order to demonstrate the versatility of the device platform, we developed three different types of microelectrode arrays. Type 1 device was used for determining the efficacy of ventral and

dorsal intradural spinal cord stimulation (iSCS) for variable electrode diameters in acute rodent models (Figure 2.1a). Type 2 device was designed for dorsal iSCS in chronic rodent models (Figure 2.1b) and type 3 device was used in spatiotemporal recording of traveling waveforms in acute pig models (Figure 2.1c). All types of devices had the porous, platinum nanorod structure, or PtNR as the electrode surface material (Figure 2.1d). Type 1 and 3 for acute models used parylene-C as the encapsulation layer, whereas type 2 was passivated with polyimide (PI2611, HD Microsystems) for improved mechanical stability in the chronic models.
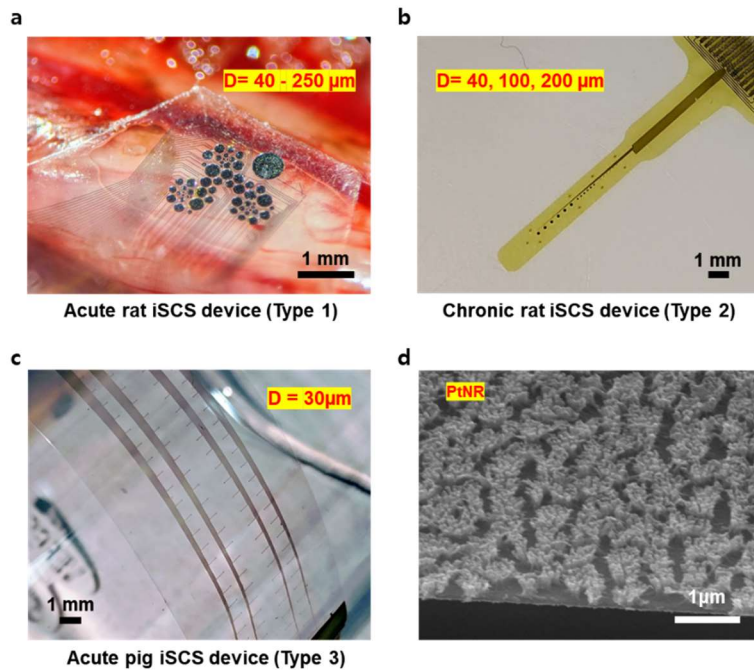


**Figure 2.1** Three different types of flexible PtNR microelectrode arrays and morphology of PtNR. (a) Type 1 device with diameters ranging between 40 μm and 250 μm. (b) Type 2 device with 18ch PtNR electrodes of diameters, 40 μm, 100 μm, and 200 μm. (c) Type 3 device with 128ch PtNR electrdoes with 30 μm diameter. (d) SEM image showing the morphology of the PtNR.

Figure 2.2 illustrates the fabrication procedure of type 1 and 3 devices. The fabrication begins with a 4-inch, single side polished, test grade Si wafer which is spin coated with antiadhesion layer of 0.4% diluted Micro-90, which is then coated with 5 μm-thick parylene-C layer (SCS Labcoter 2 Parylene Deposition System, Specialty Coating Systems). Photolithography

(NR9-3000PY, Futurrex, Inc.) and descum with $O_2$ (Plasma Etch 100, Oxford Instruments) were performed, followed by the metallization (10 nm Cr adhesion layer and 100 nm Au contact) using electron-beam evaporation (e-Beam Evaporator 2, Temescal). (Figure 2.2a)

Another photolithography was performed and descummed with $O_2$, and then the device was sputtered with 15 nm Cr as adhesion layer to Au, 100 nm Pt, and finally ~0.5 μm Pt-Ag alloy was deposited by co-sputtering technique in which the power was set at 400 W for Ag, and 50 W for Pt (Discovery 18 Sputter System, Denton). The Pt-Ag was de-alloyed by removing the Ag component from the alloy with $HNO_3$ heated at 60 °C for 2 min which leaves the PtNR electrode surface. (Figure 2.2b)

Then the device was deposited with second layer of 5 μm-thick parylene-C, spin coated with antiadhesion layer of 0.4% diluted Micro-90, and again deposited with third layer of 2 μm-thick parylene-C. (Figure 2.2c)

A dry etch mask (SU8-2015, MicroChem) was photlithographically defined (Figure 2.2d) and the second and third parylene-C layers were etched by reactive ion etching $O_2$ plasma (RIE, Plasmalab 80+, Oxford Instruments), exposing the metal connector pads and PtNR. (Figure 2.2e)

Finally, the third layer of parylene-C carrying the dry etch mask was mechanically peeled off and the device was also mechanically released from the carrier Si wafer. (Figure 2.2f)
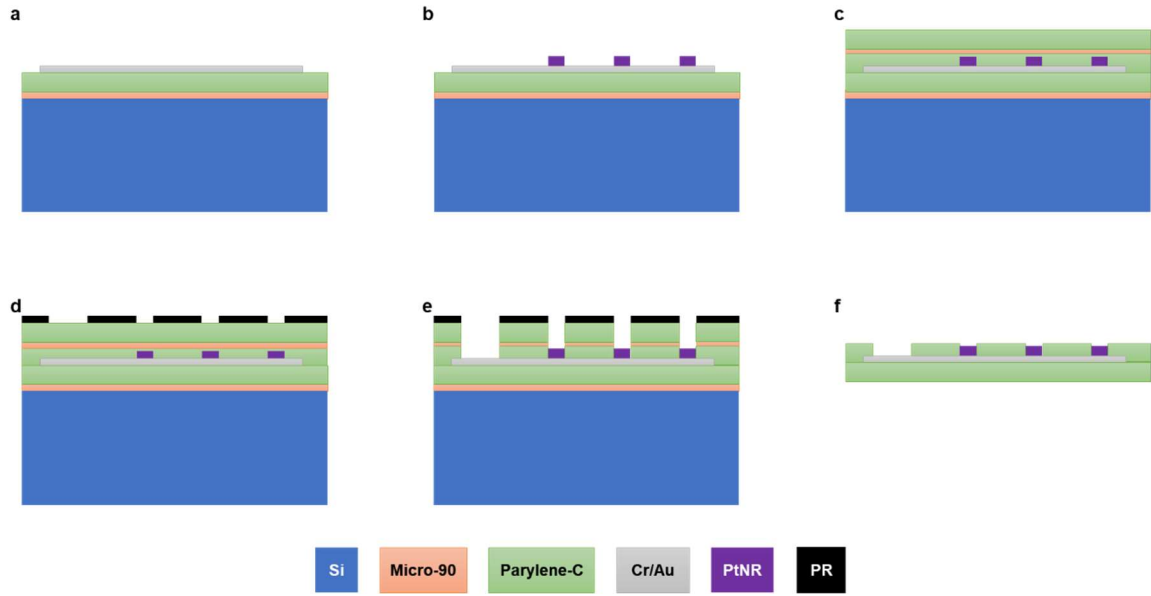
**Figure 2.2** Fabrication process flow of type 1 and type 3 PtNR devices. (a) Spin coating of Miro-90, deposition of 1st parylene-C layer, metallization. (b) Sputtering of Pt-Ag alloy and dealloying to form PtNR. (c) Deposition of 2nd parylene-C layer, spin coating of Micro-90, and deposition of 3rd parylene-C layer. (d) Photolithography of SU8 dry etch mask. (e) RIE etch of 2nd and 3rd parylene-C layers. (f) Mechanical removal of 3rd parylene-C layer and release of device.
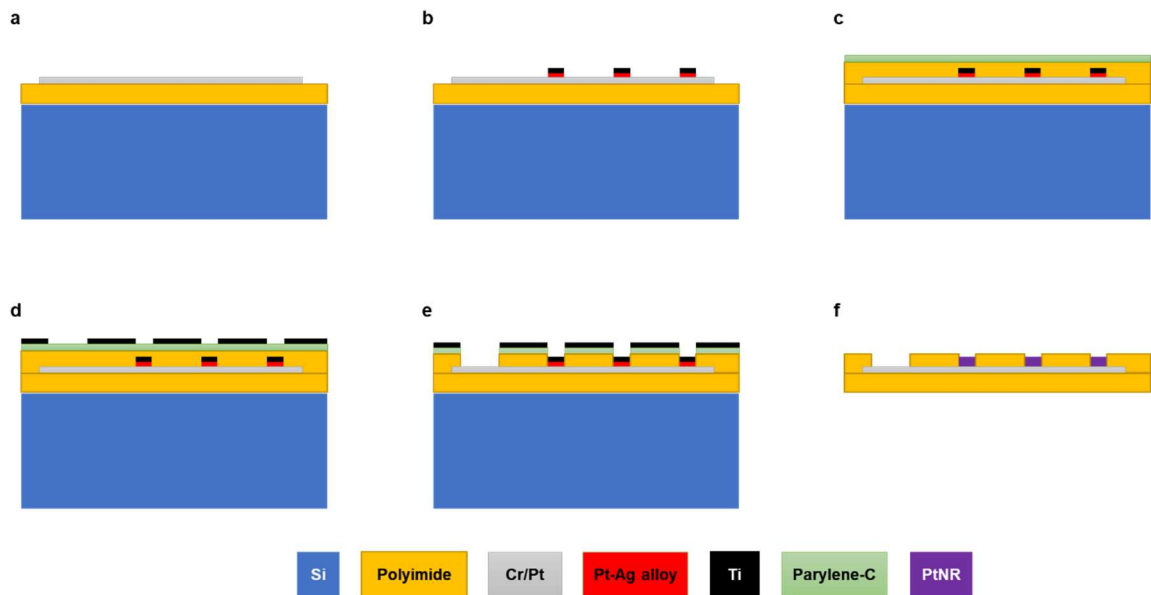


**Figure 2.3** Fabrication process flow of type 2 PtNR devices. (a) Deposition of polyimide and metallization. (b) Sputtering of Pt-Ag alloy and e-beam evaporation of Ti. (c) Deposition of 2nd polyimide layer and parylene-C layer. (d) Photolithography and e-beam evaporation of Ti dry etch mask. (e) RIE etch of 2nd polyimide layer, wet etch all Ti layers and dealloying of Pt-Ag alloy to form PtNR. (f) BOE-dip to delaminate parylene-C layer and release the device from the carrier wafer.

On the other hand, the fabrication procedure of type 2 device is illustrated in Figure 2.3. The fabrication also begins with a 4-inch, single side polished, test grade Si wafer which is spin-coated with 5 μm-thick polyimide (PI2611, HD Microsystems), and cured in nitrogen-purged oven (HTCR, Carborlite) at maximum temperature of 300 ℃. Photolithography (NR9-3000PY, Futurrex, Inc.) and descum with $O_2$ (Plasma Etch 100, Oxford Instruments) was performed, followed by sputtering of 10 nm Cr adhesion layer and 100 nm Pt for metallization. (Figure 2.3a)

Another photolithography was performed and descummed with $O_2$, and then the device was sputtered with 15 nm Cr as adhesion layer to underlying Pt, another 100 nm Pt layer, and finally ~0.5 μm Pt-Ag alloy was deposited by co-sputtering technique in which the power was set at 400 W for Ag, and 50 W for Pt. The device was then immediately transferred for electron-beam evaporation of 50 nm Ti on top of the Pt-Ag alloy. (Figure 2.3b)

The second layer of 5 μm-thick polyimide was spin-coated and cured in nitrogen-purged oven (HTCR, Carborlite) at maximum temperature of 300 ℃. The entire device is then coated with 2 μm-thick parylene-C layer for the protection of polyimide during the dealloying step later in the process. (Figure 2.3c)

The last photolithography step was performed and descummed with $O_2$, and then the device was electron-beam evaporate with 50 nm Ti. (Figure 2.3d)

The top Ti layer acts as the dry etch mask to etch the 2nd polyimide layer by reactive ion etching $O_2$ plasma, exposing the metal connector pads and the underlying Ti on Pt-Ag alloy. All Ti layers were removed with buffered oxide etchant (BOE 6:1, Sigma-Aldrich), and the Pt-Ag alloy was de-alloyed by removing the Ag component from the alloy with $HNO_3$ heated at 60 ℃ for 2 min which leaves the final PtNR electrode surface. (Figure 2.3e)

Finally, the device was left in buffered oxide etchant for around 2-7 hours which delaminates the top parylene-C layer and gradually releases the device from the carrier Si wafer. (Figure 2.3f)

### 2.2.2 Electrochemical Characterization

The benchtop electrochemical impedance measurements of all device types showed dependance with the electrode diameter, similar to the previously reported results from our laboratory.[25] Figure 2.4 shows the average impedance measured from the type 2 device implanted on chronic rat model *in vivo*. With an exception of 200 μm-diameter PtNR electrode on day 11 *in vivo* which had the later resolved connectorization issue, all diameters of electrodes showed reliable impedance values for up to 32 days *in vivo* (Figure 2.4a). Figure 2.4b shows the impedance measurements from another type 2 device, comparing the benchtop impedance measured in phosphate-buffered saline (PBS, Thermo Fisher Scientific) with day 0 *in vivo*, day 8 *in vivo* before electrical stimulation, and day 8 *in vivo* after over 1 million electrical stimulation pulses which simulates a clinical treatment of SCI. There is minimal fluctuation in the measured impedance for all parameters, thus proving the stability of the electrical performance PtNR electrodes in chronic models, not to mention for acute models.
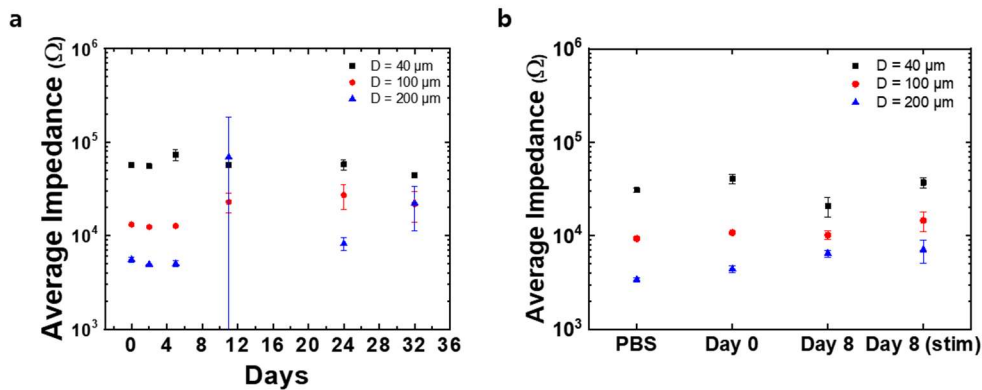


**Figure 2.4** 1kHz impedance measurements from type 2 PtNR devices on rat *in vivo*. (a) Average impedance over 32 days of implantation. (b) Comparison of benchtop, and in vivo average impedance, before and after electrical stimulation.

### 2.2.3    Acute Ventral/Dorsal and Chronic Implantation of the Device on Rat Spinal Cord

One of the key advantages of this device platform is the diversity of the implantation scheme. It is well-known that the axon of motor neurons are more concentrated on the ventral side of the spinal cord,[49] thus electrical stimulation on the ventral side is more preferable when compared to that on dorsal side of the spinal cord for successful recruitment of motor response.

The ultra-thin, 10 µm parylene-C substrate allows gentle lamination of the device around the ventral-lateral side of the spinal cord without damaging the nerve roots around it. Figure 2.5 compares the ventral-lateral and dorsal implantation of type 1 device on the rat spinal cord.
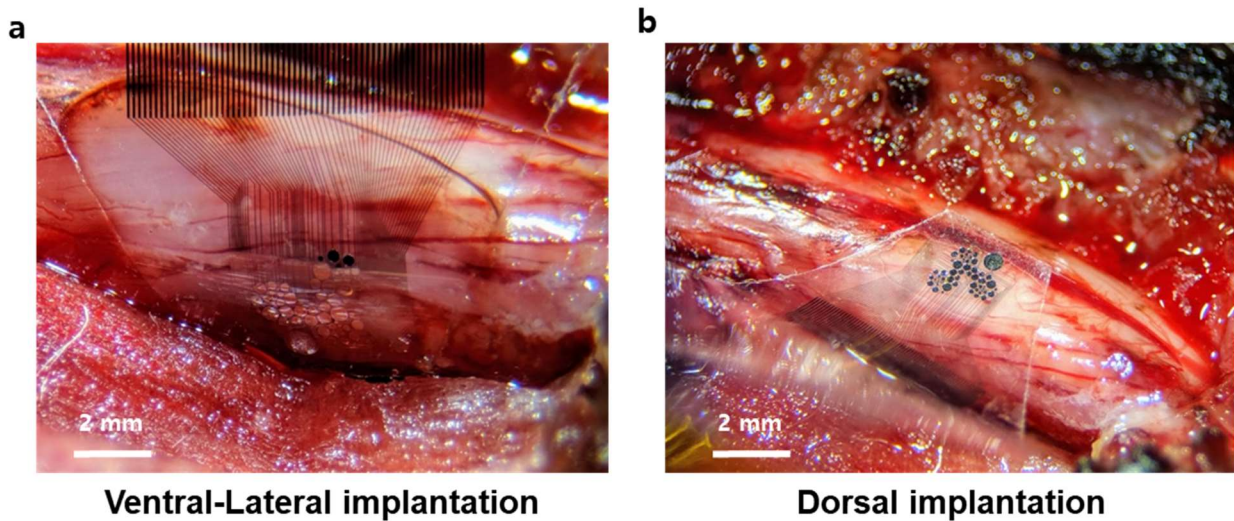


**Figure 2.5** Acute ventral/dorsal implantation of the type 1 PtNR devices on rat model. (a) Device laminating on the ventral-lateral side of the spinal cord. (b) Device rested on the dorsal side of the spinal cord.

The chronic implantation of the PtNR devices required mechanically stable frame structure to house and protect the device from rats' free motion, and secure the original coordinates of the electrode-to-spinal cord interface for consistent electrical stimulation on the same location of the spinal cord. Hence, we referred to the previously reported chronic implantation procedure used for e-dura device,[50] and modified it to suit our platform. Figure 2.6a illustrates the schematic

of our chronic implantation of type 2 device. The spinal cord region in between the thoracic and lumbar regions was exposed and the dura was removed for intradural implantation of the device. The surrounding area was supported by a dental cement structure settled along the suture framed around four clinical bone screws. The device embedded in the middle of the dental cement structure which also passivates the device except the flexible flat cable (FFC) and the PtNR electrodes that interface with the dorsal side of the spinal cord. The vacancy between the dental cement and the spinal cord was filled with absorbable gelatin powder, or gelfoam (Surgifoam, Ethicon) which kept electrodes in contact with the spinal cord. The center of the dental cement frame was sealed with biocompatible acrylic cranial window which allowed visual inspection of the implantation site afterwards (Figure 2.6b).
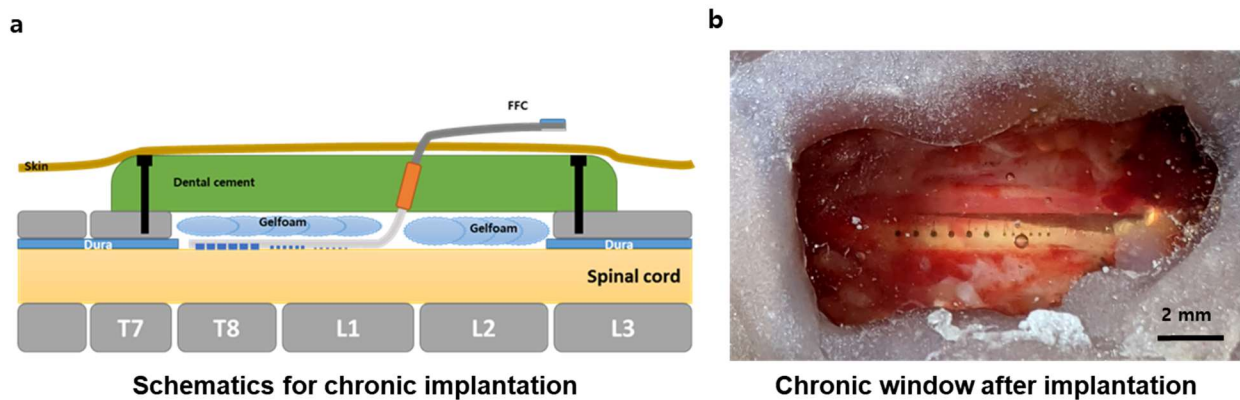


**Figure 2.6** Chronic implantation of the type 2 PtNR devices on rat model. (a) Schematic diagram of the chronic implantation. (b) Device viewed through the cranial window after implantation.

## 2.2.4    Electrical Stimulation Parameters

The correlation between charge density and injection charge illustrated by the Shannon plot [51] is known as the gold standard for safe electrical stimulation in the past few decades in which McCreery and other researchers further updated the safe guidelines for electrical stimulation using various models.[52, 53] However, the accumulated data forming the Shannon plot is mainly

based on large, penetrating conical-shaped electrodes and although tissue damage thresholds for micro and macroelectrodes, 4 nC/ph and 30 $\mu C\ cm^{-2}$, respectively, are recently reported, the validity of these guidelines still remain vague and inappropriate for emerging microelectrode technologies.[53] In particular, a systematic study on the efficacy of electrical stimulation and tissue damage thresholds when using novel materials such as platinum nanorods has not been reported to this date.

In this study, we investigated the efficacy of electrical stimulation for variable PtNR electrode diameters with different parameters of charge density and injection charge to verify the onset of stimulation-evoked motor recruitment. We also compared the stimulation-evoked motor responses from electrical stimulation of ventral-lateral and dorsal side of the spinal cord, and spatiotemporal recording of traveling waveform as a precursor to translation of this device platform in large animal studies and clinical applications.

Figure 2.7 shows the schematic of the experiment setup in which the device was implanted on the spinal cord for either acute or chronic rodent models and injected with stimulation currents. In case of acute models, a 2-prong hook electrode connected to a differential amplifier with active headstage (DP-311, Warner Instruments) for the recording of stimulation-evoked sciatic responses. Stimulation-evoked electromyography (EMG) was also recorded through a second differential amplifier with active headstage. All stimulation and recordings were synchronized using a trigger signal sent to the Intan RHD Stim/Recording Controller. The setup was identical for the chronic rat models, excluding the sciatic recording.
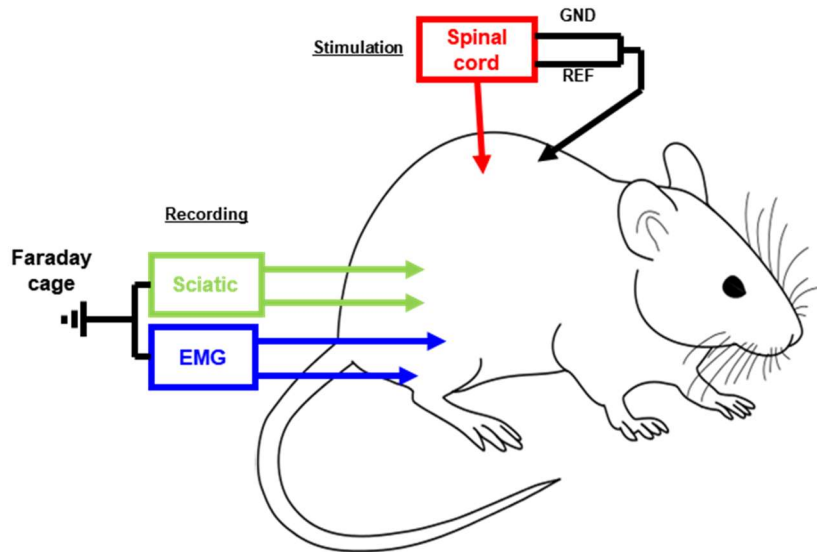
**Figure 2.7** Schematic diagram of the stimulation/recording setup.

For the electrical stimulation of the spinal cord cord in acute rodent models, we refered to the previously reported maximal charge injection capacity (CIC) values of various PtNR electrode diameter sizes which were measured in benchtop tests on saline.[25] For each diameter of PtNR electrode, the reported CIC value was set as the maximal data point at which electrical stimulation was tested in a step-wise progression of injection charge per phase or charge density per phase of a pulse train of 20 biphasic, asymmetric, cathodic first pulses as shown in Figure 2.8a.

For chronic iSCS, new CIC values and the corresponding current, $I_{max}$, at the maximal cathodal potential, $E_{cathodal}$, were measured *in vivo* with voltage transients for three reporesentative diameters, 40 μm, 100 μm, and 200 μm, of electrodes as shown in Table 2.1. This showed that *in vivo* CIC was about an order of magnitude smaller than benchtop CIC which was then used as the maximal data point at which electrical stimulation was tested in a step-wise progression of 0%, 20%, 40%, 60%, 80%, and 100% of *in vivo* CIC for a given electrode size. The pulse train of 100 symmetric pulse pairs (cathodic first) was set as shown in Figure 2.8b. Figure 2.9 shows the

stimulation charge density and injection charge per phase paramters used for acute and chronic

iSCS.
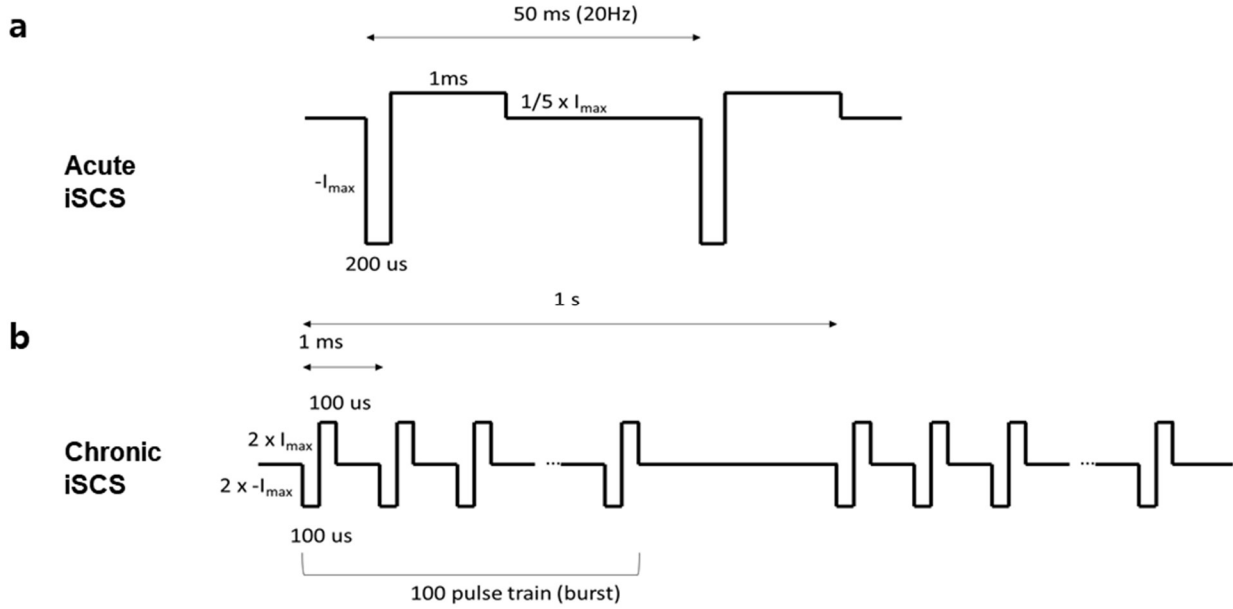


**Figure 2.8** Electrical stimulation parameters. (a) Pulse train of 20 pulse pairs for acute iSCS. (b) Pulse train of 100 pulse pairs repeated for a total of over 1 million pulses for chronic iSCS.

**Table 2.1** Comparison of the current at maximal cathodal potential in saline and rat.

| Medium | Diameter (μm) | $E_{cathodal}$ (V) | $E_{anodal}$ (V) | Current, $I_{max}$ | Impedance at 1 kHz (kΩ) |
|--------|---------------|--------------------|--------------------|--------------------|--------------------------|
| | 40 | -1.143 | 0.88 | 0.788 mA | 25 |
| Saline | 100 | -1.173 | 0.8 | 1.06 mA | 8.15 |
| | 200 | -1.25 | 0.8 | 7.10 mA | 2.986 |
| | 40 | -0.87 | 1.2 | 75.3 μA | 62.46 |
| Rat | 100 | -0.93 | 1.1 | 69.9 μA | 36.14 |
| | 200 | -1.03 | 1.25 | 795.5 μA | 5.86 |

**Figure 2.9** iSCS parameters of different PtNR electrode diameter. (a) Acute iSCS parameters plotted with Shannon line. (b) Chronic iSCS parameters plotted with Shannon line.

### 2.2.5    Animal Procedures

Acute implantation studies were performed on sprague-dawley rodents. For the surgery, adult rats were placed in the prone position and anesthetized in accordance with UCSD Institutional Animal Care and Use Committee protocol. A midline incision and laminectomy were performed to sufficiently expose the target lumbar enlargement area of the spinal cord. Following laminectomy, an incision was made into the dura, allowing exposure of the spinal cord. The sciatic nerve was also exposed and a differential hook electrode was placed across the sciatic nerve. Electromyography (EMG) needles were also placed in the ipsilateral hind limb muscles. Baseline EMG of the sciatic nerve and hindlimb muscles was conducted. The PtNR electrode array was then placed on the surface of the spinal cord, centered over the lumbar enlargement on both the ventral-lateral and dorsal surface. The ventral-lateral configuration was done by gently wrapping the distal tip of the conformable PtNR electrode array under the spinal cord. The PtNR electrode array contains a sporadic configuration of micro and macroelectrodes ranging in diameter from 40μm to 250μm. Macroelectrodes were classified as larger than 200μm in diameter. Using a step-wise progression of injection charge or charge density per electrode size, a pulse train of 20 asymmetric pulses, first with the cathodic phase of 200 μs duration followed by 1 ms anodic phase with 20% of the cathodic current was applied. we recorded the magnitude of peripheral muscle and sciatic nerve response of each electrode size and configuration. We tested up to the maximum charge injection allowed by each electrode configuration. (Figures 2.5, 2.8a, and 2.9a)

Semi-chronic implantation studies were performed on sprague-dawley rodents. For the surgery, adult rats were placed in the prone position and anesthetized in accordance to UCSD Institutional Animal Care and Use Committee protocol. Similar to the acute studies, a midline incision and laminectomy were performed to sufficiently expose the target thoracic area of the

spinal cord. Following laminectomy, an incision was made into the dura, allowing exposure of the spinal cord. A harness structure composed of dental acrylic was affixed to the spine using suture and stainless-steel screws. A clear acrylic window was affixed to the dorsal portion of the harness. A flexible flat cable from the electrode exited the caudal portion of the harness. The skin was closed circumferentially around the harness. (Figure 2.6)

Ten days after implantation, the electrodes were pulsed according to the paradigms described using charge balanced, current regulated, pulse train of 100 symmetric pulse pairs (cathodic first), with each pulse set at 100 μs per phase in duration, 1 ms pulse train period and 100 ms refractory period in between pulse pairs within the pulse train. Pulse trains were separated by 1 s to allow sufficient charge recovery. (Figure 2.8b)

Anesthesia with isoflurane was used during stimulation. Two subcutaneous EMG needles was placed in a single hindlimb. Isoflourane was started at 1-4% and delivered through a nose cone. Animals were placed over a heating blanket in a stereotactic frame during sedation and stimulation. Isoflourane was titrated to maintain breathing but minimize distress as seen on EMG and through vital sign monitoring. Neurostimulation was delivered at current levels below which will cause movement. We delivered stimulation for 2 hours and 20 minutes per day and repeat this stimulation paradigm for every third day for three days total.

After rats have finished their stimulation protocol, the animals were perfused after the stimulation for quantitative histologic evaluation of the spinal tissue subjacent to the electrode sites. In addition, tissue under reference un-stimulated electrodes were qualified for histology to compare stimulated to un-stimulated tissue. Quantitate markers of tissue damage will include structural changes and vacuolization, which can be detected with Cresyl Violet (Nissl stain). We also performed qualitative confocal immunofluorescence microscopic analysis and quantitative

analysis for neuronal loss and microgliosis/inflammatory changes using immunohistochemical markers NeuN and GFAP.

## 2.3    Results and Discussion

### 2.3.1    Efficacy of Electrical Stimulation for Variable Electrode Diameters

Figure 2.10a shows the example trial average plot of 20 stimulation trials performed with a 40 µm diameter electrode in an acute case. There is a clear time-delayed response from the sciatic nerve highlighted in green, and then followed by clear EMG response in blue. The negative peaks of each response showed a few milliseconds of delay as expected. Figure 2.10b summarizes the signal-to-noise ratio (SNR) of the stimulation-evoked sciatic responses from all paramaters of all electrode diamteres. The vertical line of 4 nC/ph was also displayed for comparison with the previously reported tissue damage threshold for penentrating electrode arrays.[53] Figure 2.11 shows the overlapped trial average plots of sciatic response acquired from all parameters for a given electrode sizes.

For any given electrode diameter, motor recruitment at the hindlimb seemed to initiate at around 100 nC/ph. It is likely that this was possible due to the higher CIC of smaller diameter microelectrrodes when compared to that of the larger macroelectrodes, thus easily reaching the threshold for response initiation despite their smaller electrode surface area. This relationship is crucial for the development of future iSCS technologies as it aims to target a very localized region of the spinal cord to induce desired motor recruitment for the treatment of SCI, while still metting the demands for higher level of CIC. Again, the discrepancy between our results with PtNR electrode arrays and those from other reported electrodes contributing to the Shannon plot

emphasized the need for systematic guidelines for safe electrical stimulation tailored for the PtNR surface electrodes.
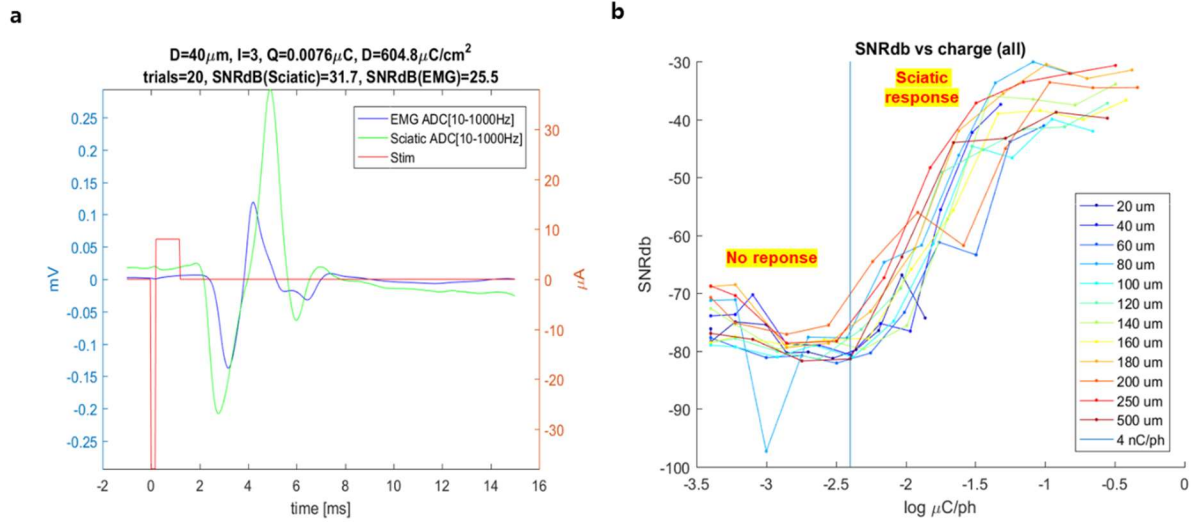


**Figure 2.10** Representative stimulation-evoked responses and summary of SNR of stimulation-evoked for all diameters. (a) An example trial average plot of stimulation-evoked sciatic and EMG responses. (b) Summary plot of the SNR of stimulation-evoked sciatic response for all diameters.
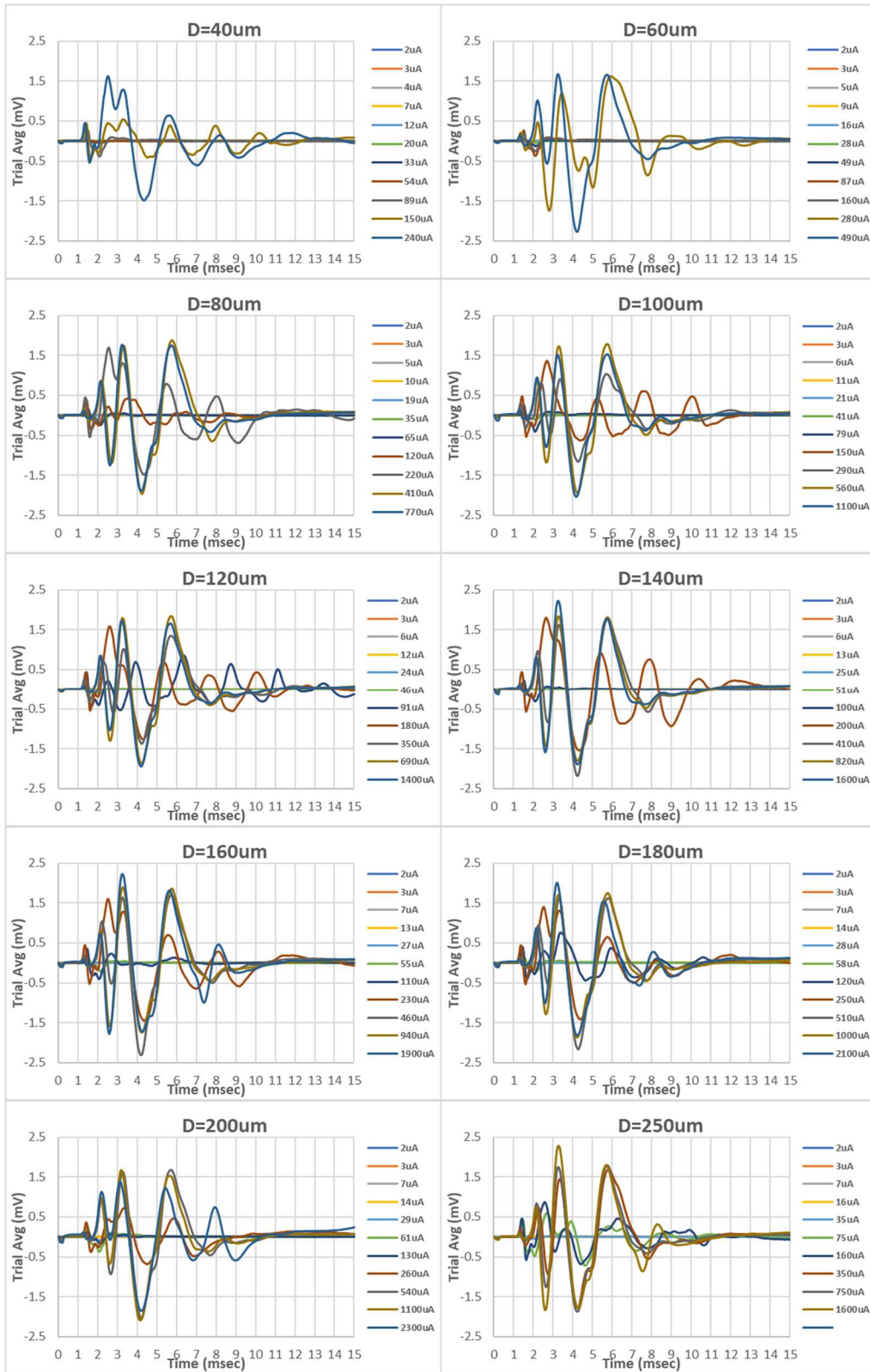
**Figure 2.11** Collection of all trial average plots of stimulation-evoked sciatic responses from all parameters of each electrode size.

### 2.3.2    Comparison of Ventral versus Dorsal Electrical Stimulation

Figure 2.12 compares the energy, or the area under the voltage curve, of the stimulation-evoked sciatic and EMG responses for three representative electrode sizes. As the amount of injected charge is increased, there is a much larger recruitment of motor response when stimulated from the ventral-lateral side of the spinal cord. The already significant discrepancy between the energy level of recruited motor response when stimulated from ventral-lateral and dorsal sides is further amplified for smaller microelectrodes. The capability of inducing stimulation-evoked responses at much lower injection charge in preferable as it lowers the risks of electrochemical degradation of the electrode material and tissue damage, especially for chronic applications.

These results implement that the development of novel microelectrode array technologies must be accompanied by a design or platform which allows more localized placement of the device on the target spinal cord region, in order to achieve efficient electrical stimulation for inducing desired responses.
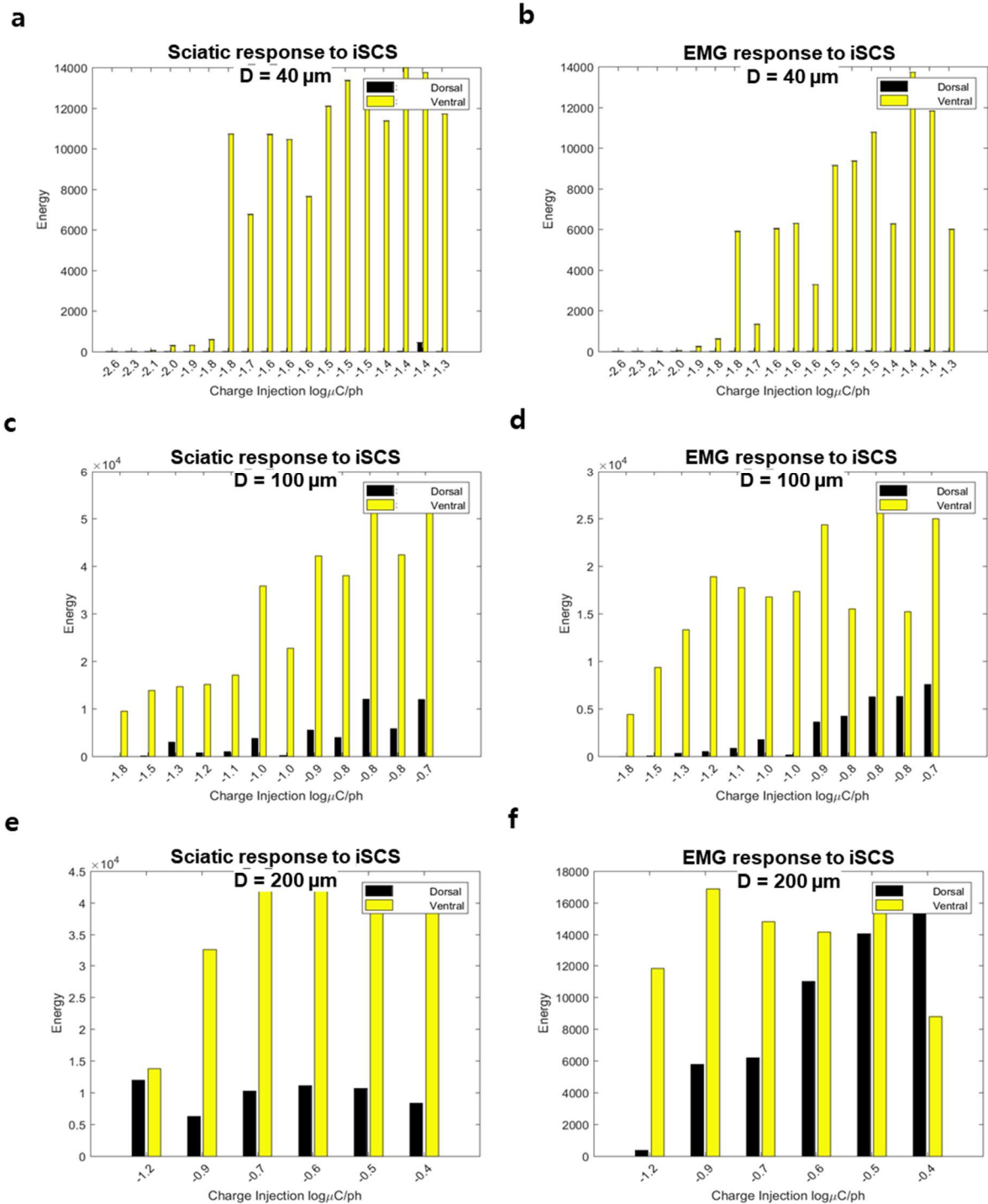
**Figure 2.12** Energy histograms of stimulation-evoked sciatic and EMG responses from ventral-lateral and dorsal stimulation of the spinal cord. (a) sciatic response of 40 µm diameter electrode. (b) EMG response of 40 µm diameter electrode. (c) sciatic response of 100 µm diameter electrode. (d) EMG response of 100 µm diameter electrode. (e) sciatic response of 200 µm diameter electrode. (f) EMG response of 200 µm diameter electrode.

### 2.3.3    Spatiotemporal Recording of Traveling Waveform

Type 3 128ch PtNR electrode array allowed large scale monitoring of stimulation evoked responses from an acute pig model. The device was a 4 × 32 array of 30 μm-diameter PtNR electrodes spaced out by 1 mm to 1.6 mm to record with large area coverage on the pig spinal cord. The ultra-thin, 10 μm parylene-C substrate allowed conformal lamination of the device on the spinal cord, thus minimizing the risk of the device rubbing against the micromotion of the pig spinal cord. (Figure 2.13)
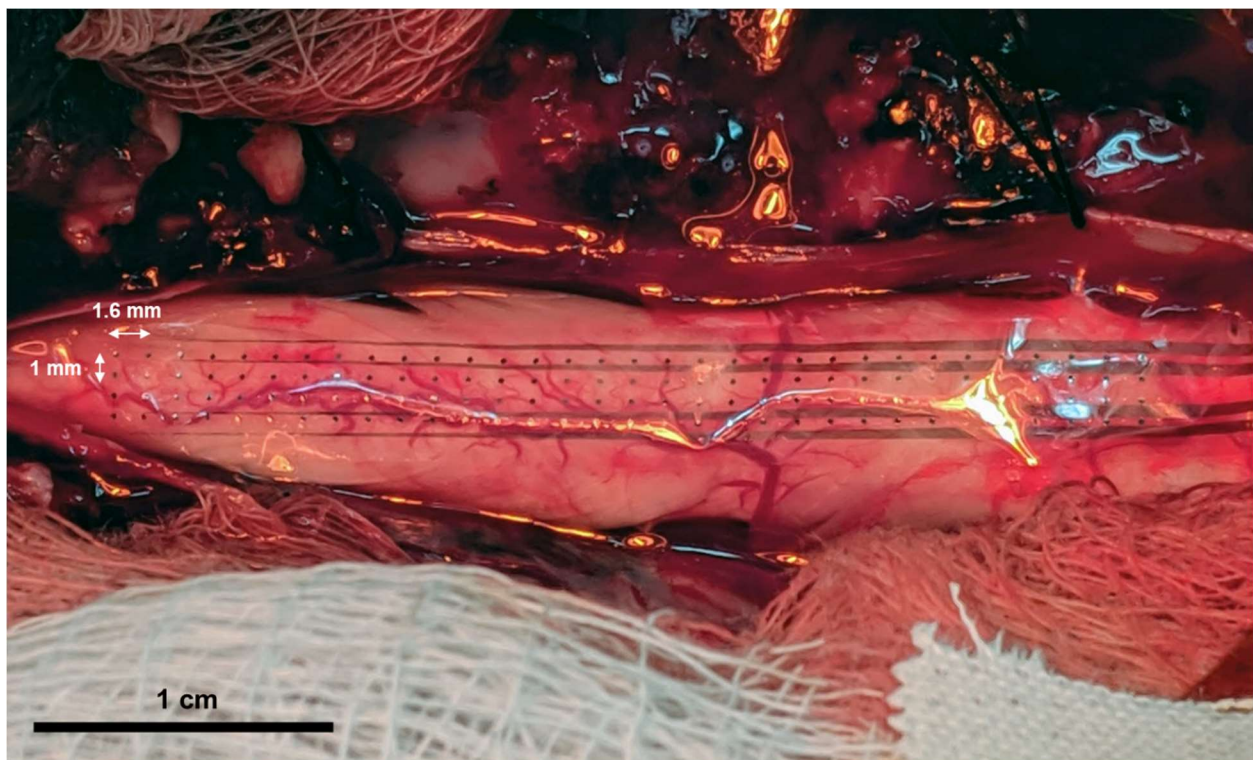


**Figure 2.13** 128ch PtNR electrode array implanted on pig spinal cord.

The 2-prong hook electrode that is in contact with the sciatic nerve of the pig model and connected to an electrical stimulator (A360 Stimulus Isolator, WPI) in synchronization with the Intan RHD Stim/Recording System using trigger signals. The electrical stimulator delivered a total of 30 anodal, monophasic pulses with 100 μs duration and injection current of 200 μA, 400 μA,

600 μA, 800 μA, and 1000 μA. Figure 2.14a shows the trial average plot of stimulation-evoked compound action potentials (CAP) recorded from the PtNR electrode that was in the most distal position relative to the hook electrode. The recorded CAPs in the spinal cord were proportional to the injection current of the stimulation and reached up to few mV. Figure 2.14b shows the CAPs recorded from PtNR electrodes from different locations. The electrode that had the closest distance distal from the stimulation source was marked as 0 mm. There was a clear indication of traveling waves, thus confirming the spatiotemporal property of the stimulation-evoked CAPs. As shown in Figure 2.14c, these traveling waves recorded for different stimulation current settings were used to calculate the velocity of the traveling waves, implementing the possibility of inducing specific fiber recruitment for future studies.
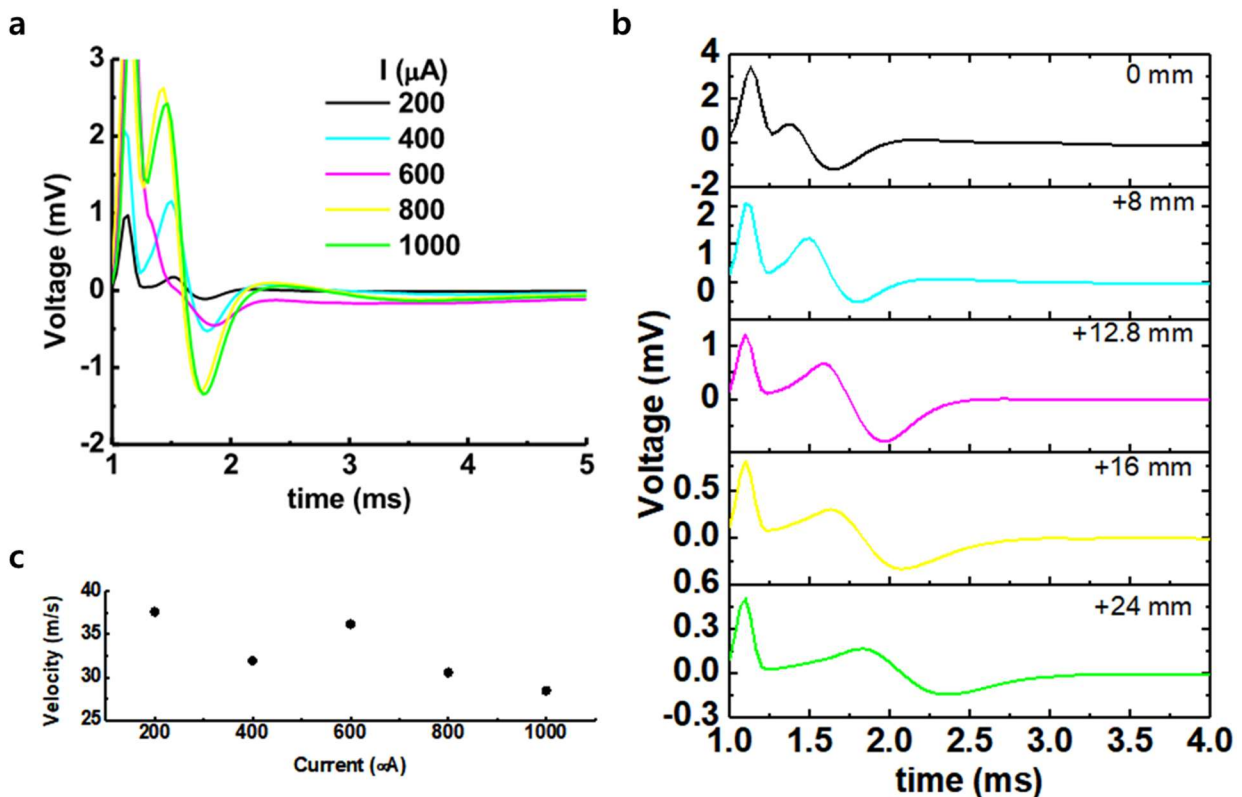


**Figure 2.14** Recording of stimulation-evoked CAPs and traveling waves. (a) Trial average plot of stimulation-evoked CAPs in the pig spinal cord. (b) Recorded traveling waves from different electrode sites. (c) Calculated velocity of the traveling waves from (b).

## 2.4     Conclusion

In this work, we developed a transparent, minimally invasive, and scalable PtNR-based devices for systematic study of iSCS thresholds for motor response using the PtNR electrode arrays. We confirmed that the smaller diameter electrodes demonstrated higher efficient charge delivery comparable to that of larger electrodes, promising high resolution, fine targeting of stimulation regions, without compromising the electrochemical performance of the device. We also found that this novel platform allows ventral-lateral insertion of the device unlike more commonly used, dorsal implantation. This allows more efficient recruitment of motor response at much lower charge injection levels. Our devices also demonstrated high scalability for various *in vivo* models while maintaining minimal invasiveness, and was suitable for high resolution spatiotemporal recording. Further studies such as the immunohistochemistry of the spinal cord for the detection of tissue damage thresholds of PtNR electrodes in chronic models, simultaneous stimulation and recording from the PtNR electrode sites for a more conclusive analysis of traveling waveforms, and transition to larger animal models for to promote future clinical applications are needed to improve the scope of this research.

Chapter 2, in full, is currently being prepared for submission for publication of the material. S. H. Lee, J. R. Martin, D. R. Cleary, K. Tonsfeldt, J. Ciacci, S. A. Dayeh. The dissertation author is the primary investigator and author of this paper.

## References

[1]     S. S. Cash, L. R. Hochberg, Neuron 2015, 86, 79.


[2]     I. Fried, C. L. Wilson, N. T. Maidment, J. Engel Jr, E. Behnke, T. A. Fields, K. A. Macdonald, J. W. Morrow, L. Ackerson, Journal of neurosurgery 1999, 91, 697; G. A. Worrell, A. B. Gardner, S. M. Stead, S. Hu, S. Goerss, G. J. Cascino, F. B. Meyer, R. Marsh, B. Litt, Brain 2008, 131, 928; I. Ulbert, E. Halgren, G. Heit, G. Karmos, Journal of neuroscience methods 2001, 106, 69; C. T. Nordhausen, E. M. Maynard, R. A. Normann, Brain research 1996, 726, 129.


[3]     L. R. Hochberg, M. D. Serruya, G. M. Friehs, J. A. Mukand, M. Saleh, A. H. Caplan, A. Branner, D. Chen, R. D. Penn, J. P. Donoghue, Nature 2006, 442, 164; S.-P. Kim, J. D. Simeral, L. R. Hochberg, J. P. Donoghue, M. J. Black, Journal of neural engineering 2008, 5, 455; L. R. Hochberg, D. Bacher, B. Jarosiewicz, N. Y. Masse, J. D. Simeral, J. Vogel, S. Haddadin, J. Liu, S. S. Cash, P. Van Der Smagt, Nature 2012, 485, 372; J. L. Collinger, B. Wodlinger, J. E. Downey, W. Wang, E. C. Tyler-Kabara, D. J. Weber, A. J. McMorland, M. Velliste, M. L. Boninger, A. B. Schwartz, The Lancet 2013, 381, 557.


[4]     A. Bragin, C. L. Wilson, R. J. Staba, M. Reddick, I. Fried, J. Engel, Annals of neurology 2002, 52, 407; C. J. Keller, W. Truccolo, J. T. Gale, E. Eskandar, T. Thesen, C. Carlson, O. Devinsky, R. Kuzniecky, W. K. Doyle, J. R. Madsen, Brain 2010, 133, 1668; W. Truccolo, O. J. Ahmed, M. T. Harrison, E. N. Eskandar, G. R. Cosgrove, J. R. Madsen, A. S. Blum, N. S. Potter, L. R. Hochberg, S. S. Cash, Journal of Neuroscience 2014, 34, 9927; W. Truccolo, J. A. Donoghue, L. R. Hochberg, E. N. Eskandar, J. R. Madsen, W. S. Anderson, E. N. Brown, E. Halgren, S. S. Cash, Nature neuroscience 2011, 14, 635.


[5]     M. L. MacMillan, J. O. Dostrovsky, A. M. Lozano, W. D. Hutchison, Journal of neurophysiology 2004, 91, 1085; H. Bergman, G. Deuschl, Movement Disorders 2002, 17; A. K. Engel, C. K. Moll, I. Fried, G. A. Ojemann, Nature Reviews Neuroscience 2005, 6, 35.


[6]     A. M. Chan, A. R. Dykstra, V. Jayaram, M. K. Leonard, K. E. Travis, B. Gygi, J. M. Baker, E. Eskandar, L. R. Hochberg, E. Halgren, Cerebral Cortex 2013, 24, 2679; R. Q. Quiroga, G. Kreiman, C. Koch, I. Fried, Trends in cognitive sciences 2008, 12, 87; A. Tankus, I. Fried, S. Shoham, Nature communications 2012, 3, 1015; I. Fried, R. Mukamel, G. Kreiman, Neuron 2011, 69, 548; M. K. Mian, S. A. Sheth, S. R. Patel, K. Spiliopoulos, E. N. Eskandar, Z. M. Williams, Cerebral cortex 2012, 24, 807; G. Kreiman, Current opinion in neurobiology 2007, 17, 471; M. P. Walker, R. Stickgold, Neuron 2004, 44, 121; S. Diekelmann, J. Born, Nature Reviews Neuroscience 2010, 11, 114.


[7]     J. C. Barrese, N. Rao, K. Paroo, C. Triebwasser, C. Vargas-Irwin, L. Franquemont, J. P. Donoghue, Journal of neural engineering 2013, 10, 066014.

[8]     A. B. Schwartz, X. T. Cui, D. J. Weber, D. W. Moran, Neuron 2006, 52, 205.


[9]     M. Leber, R. Bhandari, F. Solzbacher, S. Negi, "Novel method of fabricating self-dissolvable and freely floating neural array", presented at *2017 19th International Conference on Solid-State Sensors, Actuators and Microsystems (TRANSDUCERS)*,   2017.


[10]     A. Ersen, S. Elkabes, D. S. Freedman, M. Sahin, Journal of neural engineering 2015, 12, 016019.


[11]     X. Zheng, *Neural Interface: Frontiers and Applications*, Springer,   2019.


[12]     M. Shandhi, M. Leber, A. Hogan, R. Bhandari, S. Negi, "A novel method of fabricating high channel density neural array for large neuronal mapping", presented at *2015 Transducers-2015 18th International Conference on Solid-State Sensors, Actuators and Microsystems (TRANSDUCERS)*,   2015.


[13]     J. Klein, S. Clauson, S. Cogan, Journal of Vacuum Science & Technology A: Vacuum, Surfaces, and Films 1989, 7, 3043; R. D. Meyer, S. F. Cogan, T. H. Nguyen, R. D. Rauh, IEEE Transactions on Neural Systems and Rehabilitation Engineering 2001, 9, 2; S. Negi, R. Bhandari, L. Rieth, F. Solzbacher, Sensors and Actuators B: Chemical 2009, 137, 370; L. Robblee, J. McHardy, W. Agnew, L. Bullara, Journal of neuroscience methods 1983, 9, 301; L. S. Robblee, M. J. Mangaudis, E. D. Lasinsky, A. G. Kimball, S. B. Brummer, MRS Online Proceedings Library Archive 1985, 55; B. Wessling, W. Mokwa, U. Schnakenberg, Journal of Micromechanics and Microengineering 2006, 16, S142.


[14]     S. Park, Y. J. Song, H. Boo, T. D. Chung, The Journal of Physical Chemistry C 2010, 114, 8721; C. A. Marrese, Analytical chemistry 1987, 59, 217; R. A. Green, H. Toor, C. Dodds, N. H. Lovell, Sensors and Materials 2012, 24, 165; R. Green, P. Matteucci, C. Dodds, J. Palmer, W. Dueck, R. Hassarati, P. Byrnes-Preston, N. Lovell, G. Suaning, Journal of neural engineering 2014, 11, 056017; W. Franks, I. Schenker, P. Schmutz, A. Hierlemann, IEEE Transactions on Biomedical Engineering 2005, 52, 1295; D. Zhou, Google Patents,   2007; J. J. Whalen III, J. Young, J. D. Weiland, P. C. Searson, Journal of the Electrochemical Society 2006, 153, C834; A. Weremfo, P. Carter, D. B. Hibbert, C. Zhao, Langmuir 2015, 31, 2593; M. Tykocinski, Y. Duan, B. Tabor, R. S. Cowan, Hearing research 2001, 159, 53; A. Bolzan, A. C. Luna, A. Visintin, R. Salvarezza, A. Arvia, Electrochimica Acta 1988, 33, 1743.


[15]     J. Zhang, F. Laiwalla, J. A. Kim, H. Urabe, R. Van Wagenen, Y.-K. Song, B. W. Connors, F. Zhang, K. Deisseroth, A. V. Nurmikko, Journal of neural engineering 2009, 6, 055007; J. Wang, F. Wagner, D. A. Borton, J. Zhang, I. Ozden, R. D. Burwell, A. V. Nurmikko, R. van Wagenen, I. Diester, K. Deisseroth, Journal of neural engineering 2011, 9, 016001.

[16]     T. V. F. Abaya, M. Diwekar, S. Blair, P. Tathireddy, L. Rieth, F. Solzbacher, Journal of Biomedical Optics 2014, 19, 015006; T. Abaya, M. Diwekar, S. Blair, P. Tathireddy, L. Rieth, F. Solzbacher, "3D waveguide penetrating arrays for optical neural stimulation", presented at *2012 International Conference on Optical MEMS and Nanophotonics*，  2012.

[17]     L. Luan, X. Wei, Z. Zhao, J. J. Siegel, O. Potnis, C. A. Tuppen, S. Lin, S. Kazmi, R. A. Fowler, S. Holloway, Science advances 2017, 3, e1601966; J. E. Chung, H. R. Joo, J. L. Fan, D. F. Liu, A. H. Barnett, S. Chen, C. Geaghan-Breiner, M. P. Karlsson, M. Karlsson, K. Y. Lee, Neuron 2019, 101, 21.

[18]     E. Musk, Journal of medical Internet research 2019, 21, e16194.

[19]     T. D. Y. Kozai, N. B. Langhals, P. R. Patel, X. Deng, H. Zhang, K. L. Smith, J. Lahann, N. A. Kotov, D. R. Kipke, Nature materials 2012, 11, 1065.

[20]     P. R. Patel, K. Na, H. Zhang, T. D. Kozai, N. A. Kotov, E. Yoon, C. A. Chestek, Journal of neural engineering 2015, 12, 046009.

[21]     A. Canales, X. Jia, U. P. Froriep, R. A. Koppes, C. M. Tringides, J. Selvidge, C. Lu, C. Hou, L. Wei, Y. Fink, Nature biotechnology 2015, 33, 277.

[22]     A. Obaid, M.-E. Hanna, Y.-W. Wu, M. Kollo, R. Racz, M. R. Angle, J. Müller, N. Brackbill, W. Wray, F. Franke, Science advances 2020, 6, eaay2789.

[23]     K. Sahasrabuddhe, A. A. Khan, A. P. Singh, T. M. Stern, Y. Ng, A. Tadić, P. Orel, C. LaReau, D. Pouzzner, K. Nishimura, bioRxiv 2020.

[24]     A. Shadi, F. Azzazy, S. H. Lee, Google Patents，  2017.

[25]     M. Ganji, A. C. Paulk, J. C. Yang, N. W. Vahidi, S. H. Lee, R. Liu, L. Hossain, E. M. Arneodo, M. Thunemann, M. Shigyo, Nano letters 2019, 19, 6244.

[26]     M. Brosch, M. Deckert, S. Rathi, K. Takagaki, T. Weidner, F. W. Ohl, B. Schmidt, M. T. Lippert, Journal of Neural Engineering 2020, 17, 046014.

[27]     Y. Hanein, C. Schabmueller, G. Holman, P. Luecke, D. Denton, K. Böhringer, Journal of Micromechanics and Microengineering 2003, 13, S91.

[28]     A. B. Kibler, B. G. Jamieson, D. M. Durand, Journal of neuroscience methods 2012, 204, 296.

[29]     K. Miller, M. Li, K. M. Walsh, X.-A. Fu, Journal of Micromechanics and Microengineering 2013, 23, 035039.

[30]     P. K. Campbell, K. E. Jones, R. J. Huber, K. W. Horch, R. A. Normann, IEEE Transactions on Biomedical Engineering 1991, 38, 758.

[31]     R. Bhandari, S. Negi, F. Solzbacher, Biomedical microdevices 2010, 12, 797.

[32]     G. J. Goldey, D. K. Roumis, L. L. Glickfeld, A. M. Kerlin, R. C. Reid, V. Bonin, D. P. Schafer, M. L. Andermann, Nature protocols 2014, 9, 2515.

[33]     X. Cui, D. C. Martin, Sensors and Actuators B: Chemical 2003, 89, 92; X. T. Cui, D. D. Zhou, IEEE Transactions on Neural Systems and Rehabilitation Engineering 2007, 15, 502; X. Luo, X. T. Cui, Acta Biomaterialia 2011, 7, 441; C. Nick, S. Quednau, R. Sarwar, H. Schlaak, C. Thielemann, Microsystem technologies 2014, 20, 1849; C. Nick, C. Thielemann, H. F. Schlaak, "PEDOT: PSS coated gold nanopillar microelectrodes for neural interfaces", presented at *2014 International Conference on Manipulation, Manufacturing and Measurement on the Nanoscale (3M-NANO)*,   2014.

[34]     P. J. Rousche, R. A. Normann, IEEE transactions on rehabilitation engineering 1999, 7, 56.

[35]     M. Thunemann, Y. Lu, X. Liu, K. Kılıç, M. Desjardins, M. Vandenberghe, S. Sadegh, P. A. Saisan, Q. Cheng, K. L. Weldy, Nature communications 2018, 9, 1.

[36]     P. J. Rousche, R. A. Normann, Annals of biomedical engineering 1992, 20, 413.

[37]     P. A. House, J. D. MacDonald, P. A. Tresco, R. A. Normann, Neurosurgical focus 2006, 20, 1.

[38]     J. A. Gorski, T. Talley, M. Qiu, L. Puelles, J. L. Rubenstein, K. R. Jones, Journal of Neuroscience 2002, 22, 6309; L. Madisen, T. Mao, H. Koch, J.-m. Zhuo, A. Berenyi, S. Fujisawa, Y.-W. A. Hsu, A. J. Garcia, X. Gu, S. Zanella, Nature neuroscience 2012, 15, 793.

[39]     M. Desjardins, K. Kılıç, M. Thunemann, C. Mateo, D. Holland, C. G. Ferri, J. A. Cremonesi, B. Li, Q. Cheng, K. L. Weldy, Biological Psychiatry: Cognitive Neuroscience and Neuroimaging 2019, 4, 533.

[40]     H. Uhlirova, K. Kılıç, P. Tian, M. Thunemann, M. Desjardins, P. A. Saisan, S. Sakadžić, T. V. Ness, C. Mateo, Q. Cheng, elife 2016, 5, e14315.

[41]     B. P. Christie, D. M. Tat, Z. T. Irwin, V. Gilja, P. Nuyujukian, J. D. Foster, S. I. Ryu, K. V. Shenoy, D. E. Thompson, C. A. Chestek, Journal of neural engineering 2014, 12, 016009; J. Park, G. Kim, S.-D. Jung, IEEE Transactions on Neural Systems and Rehabilitation Engineering 2017, 25, 2227.

[42]     T. Honjoh, Z.-G. Ji, Y. Yokoyama, A. Sumiyoshi, Y. Shibuya, Y. Matsuzaka, R. Kawashima, H. Mushiake, T. Ishizuka, H. Yawo, PloS one 2014, 9, e93706; R. Reig, G. Silberberg, Neuron 2014, 83, 1200.

[43]     M.-A. Bellavance, J. Takatoh, J. Lu, M. Demers, D. Kleinfeld, F. Wang, M. Deschênes, Neuron 2017, 95, 673; Q.-T. Nguyen, D. Kleinfeld, Neuron 2005, 45, 447.

[44]     D. R. Ollerenshaw, B. A. Bari, D. C. Millard, L. E. Orr, Q. Wang, G. B. Stanley, Journal of neurophysiology 2012, 108, 479.

[45]     I. R. Minev, P. Musienko, A. Hirsch, Q. Barraud, N. Wenger, E. M. Moraud, J. Gandar, M. Capogrosso, T. Milekovic, L. Asboth, R. F. Torres, N. Vachicouras, Q. Liu, N. Pavlova, S. Duis, A. Larmagnac, J. Voros, S. Micera, Z. Suo, G. Courtine, S. P. Lacour, Science 2015, 347, 159.

[46]     L. H. Sekhon, M. G. Fehlings, Spine 2001, 26, S2.

[47]     S. F. Cogan, K. A. Ludwig, C. G. Welle, P. Takmakov, Journal of neural engineering 2016, 13, 021001.

[48]     M. Ganji, A. Tanaka, V. Gilja, E. Halgren, S. A. Dayeh, Advanced Functional Materials 2017.

[49]     R. T. Johnson, J. E. Joy, B. M. Altevogt, C. T. Liverman, *Spinal cord injury: progress, promise, and priorities*, National Academies Press,    2005.

[50]     I. R. Minev, P. Musienko, A. Hirsch, Q. Barraud, N. Wenger, E. M. Moraud, J. Gandar, M. Capogrosso, T. Milekovic, L. Asboth, Science 2015, 347, 159.


[51]     R. V. Shannon, IEEE Transactions on biomedical engineering 1992, 39, 424.


[52]     S. F. Cogan, Annu. Rev. Biomed. Eng. 2008, 10, 275; S. F. Cogan, J. Ehrlich, T. D. Plante, A. Smirnov, D. B. Shire, M. Gingerich, J. F. Rizzo, Journal of Biomedical Materials Research Part B: Applied Biomaterials: An Official Journal of The Society for Biomaterials, The Japanese Society for Biomaterials, and The Australian Society for Biomaterials and the Korean Society for Biomaterials 2009, 89, 353; S. F. Cogan, A. A. Guzelian, W. F. Agnew, T. G. Yuen, D. B. McCreery, Journal of neuroscience methods 2004, 137, 141; S. F. Cogan, P. R. Troyk, J. Ehrlich, T. D. Plante, IEEE Transactions on Biomedical Engineering 2005, 52, 1612; D. McCreery, W. Agnew, T. Yuen, L. Bullara, Annals of biomedical engineering 1988, 16, 463; D. B. McCreery, W. F. Agnew, T. G. Yuen, L. Bullara, IEEE Transactions on Biomedical Engineering 1990, 37, 996; R. Shepherd, G. M. Clark, R. Black, Acta Oto-Laryngologica 1983, 95, 19; R. Shepherd, G. M. Clark, R. Black, J. Patrick, Scientific publications, vol. 2, 1978-1983, no. 145 1983; R. K. Shepherd, D. B. McCreery, in *Cochlear and Brainstem Implants*, Vol. 64, Karger Publishers,   2006, 186.


[53]     S. F. Cogan, K. A. Ludwig, C. G. Welle, P. Takmakov, Journal of neural engineering 2016, 13, 021001.